The Coordinated Control of Space Robot Teams for the On-Orbit Construction of Large Flexible Space Structures

by

Peggy Boning

Bachelor of Science, Mechanical Engineering
Massachusetts Institute of Technology, 1985

Master of Science, Mechanical Engineering
Stanford University, 1986

Submitted to the Department of Mechanical Engineering
in partial fulfillment of the requirements for the degree of
Doctor of Philosophy in Mechanical Engineering

at the

Massachusetts Institute of Technology

February 2009

Signature of Author .....
Department of Mechanical Engineering
December 17, 2008

Certified by .....
Steven Dubowsky
Professor of Mechanical Engineering
Thesis Supervisor and Committee Chairman

Accepted by .....
Professor David E. Hardt
Chairman, Committee on Graduate Studies

The Coordinated Control of Space Robot Teams for the On-Orbit Construction of Large Flexible Space Structures

by

Peggy Boning

Submitted to the Department of Mechanical Engineering
on December 17, 2008, in partial fulfillment of the
requirements for the degree of
Doctor of Philosophy in Mechanical Engineering

ABSTRACT

Teams of autonomous space robots are needed for future space missions such as the construction of large solar power stations and large space telescopes in earth orbit. This work focuses on the control of teams of robots performing construction tasks such as manipulation and assembly of large space structures. The control of the robot structure system is difficult. The space structures are flexible and there are significant dynamic interactions between the robots and the structures. Forces applied by the robots may excite undesirable vibrations in the structures. Furthermore, the changing configuration of the system results in the system dynamics being described by a set of non-linear partial differential equations. Limited sensing and actuation in space present additional challenges. The approach proposed here is to transform the system dynamics into a set of linear time-varying ordinary differential equations. The control of the high-frequency robots can be decoupled from the control of the low-frequency structures. This approach allows the robots to apply forces to the structures and control the dynamic interactions between the structures and the robots. The approach permits linear optimal control theory to be used. Simulation studies and experimental verification demonstrate the validity of the approach.

Thesis Committee: Dr. Steven Dubowsky, Chair
Professor of Mechanical Engineering

Dr. David W. Miller
Professor of Aeronautics and Astronautics

Dr. Daniela Rus
Professor of Electrical Engineering and Computer Science

ACKNOWLEDGMENTS

I would like to thank my advisor, Prof. Steven Dubowsky, for his guidance and support. I would also like to thank the members of my committee, Prof. Daniela Rus and Prof. David W. Miller, for their encouragement and advice. Prof. Rich Wiesman from Mechanical Engineering shared valuable technical insight.

I would like to thank the Japan Aerospace Exploration Agency (JAXA) for its support of this work. In particular, Dr. Mitsushige Oda, Dr. Yoshiaki Ohkami, Yoshiyuki Ishijima and Hiroshi Ueno provided helpful comments and advice about space systems.

I am grateful to my research group at the Field and Space Laboratory (FSRL) for their help, advice, and friendship. This thesis builds on and extends a previous experimental infrastructure built by members of the FSRL. Dr. Matthew Lichter, Dr. Jamie Nichol, Prof. Yoji Kuroda, and Patrick Barragán made significant contributions to the design and construction of the experimental robots and testbed. Chris Ward started me down the path to xPC. Masahiro Ono did experimental work for his own Master's thesis and collaborated with me on related research. Tatsuro 'Ted' Nohara put in long hours debugging hardware and running experiments and Chiara Toglio ran simulations. Thanks to Dimitrios Tzeranis, Steve Peters, Sam Kessner, Chris Brooks, Dr. Karl Iagnemma, Dr. JS Plante, Dr. Matthew Spenko, Amy Bilton, Will Becker, Lauren Devita, Martin Udengaard and Dan Kettler for their help, conversation and advice. Thanks also to Marcos Berrios, Andrew Harlan, Ta Kim, Dan Lopuch, Francesco Mazzini, and Dr. Kenjiro Tadakuma. I would like to acknowledge Kate Anderson for her work preparing for the MIT Space Solar Power Workshop.

I also appreciate the assistance I received from students and staff in Prof. Rus and Prof. Miller's laboratories, especially Swati Mohan, Dr. Alvar Saenz-Otero, and Paul Bauer.

I would like to thank Prof. Rohan Abeyaratne and the Department of Mechanical Engineering for their support. In the Mechanical Engineering Graduate Office, Leslie Regan and Joan Kravit were especially helpful.

I would like to thank my family for their enthusiasm and encouragement. This thesis is dedicated to my husband Duane and to my children Will and Tom. I hope I have inspired you on your own educational journeys.

CONTENTS

FIGURES

TABLES

CHAPTER

1

INTRODUCTION

This chapter introduces the thesis and the motivation for building large space structures in Section 1.1. Then, the background and literature are presented in Section 1.2. The thesis contributions are described in Section 1.3, and the thesis organization is outlined in Section 1.4.

1.1 Motivation

Teams of autonomous space robots will be needed for future space missions, such as the construction of large solar power stations and space telescopes (see Figure 1.1) [35][67][86]. Currently, astronauts perform extra-vehicular activities (EVAs) to carry out such tasks; such EVAs are expensive and the space environment is dangerous for astronauts. Additionally, future space structures are expected to be significantly larger than existing structures, on the order of hundreds of meters to kilometers in scale [85]. The International Space Station, at present the largest on-orbit structure, is roughly one hundred meters across its longest dimension (see Figure 1.2) [63]. In contrast, the overall dimensions of a proposed solar power station, the Integrated Symmetrical Concentrator, shown in Figure 1.3, are about five by fifteen kilometers [52][57][62]. These large flexible structures will need to be assembled on orbit by teams of autonomous space robots [32][97].

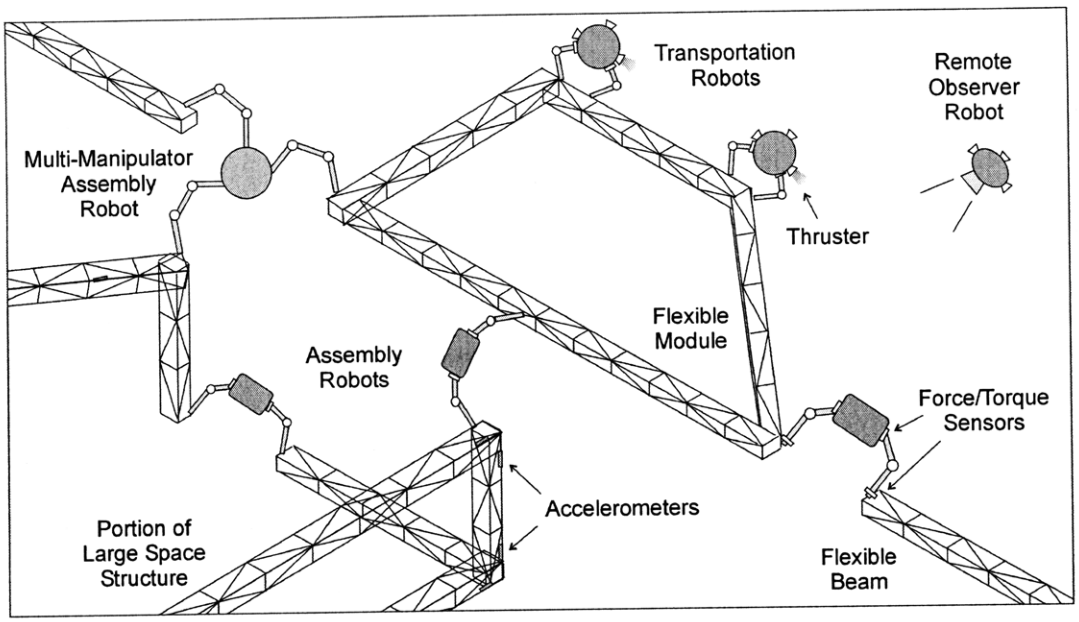

Figure 1.1. On-orbit construction of large flexible space structures by heterogeneous robotic teams.

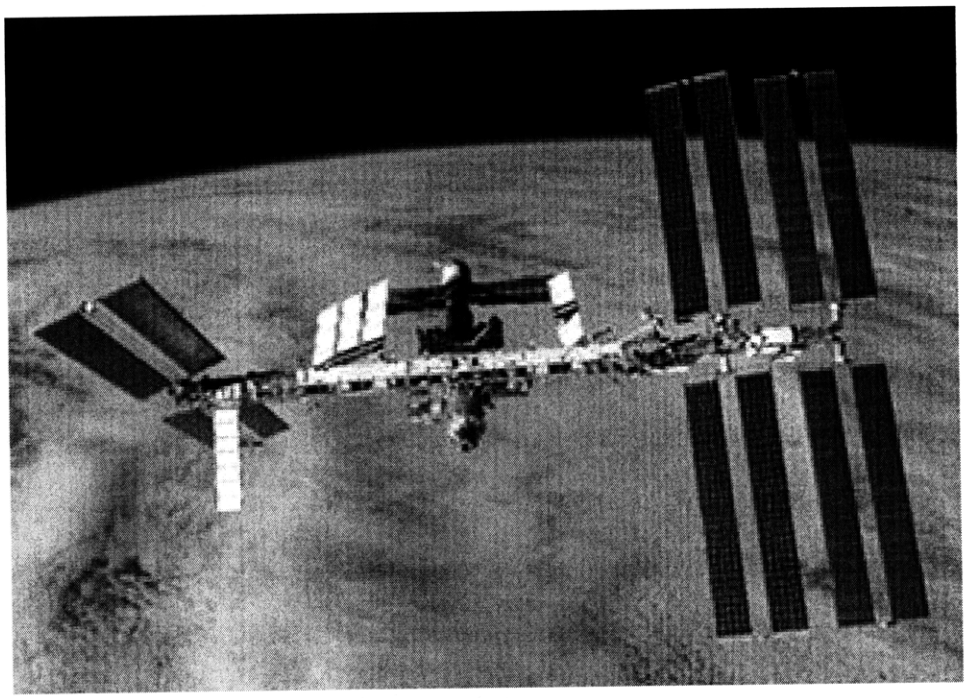

Figure 1.2. The International Space Station as seen from Space Shuttle Discovery (NASA Photograph [63]).

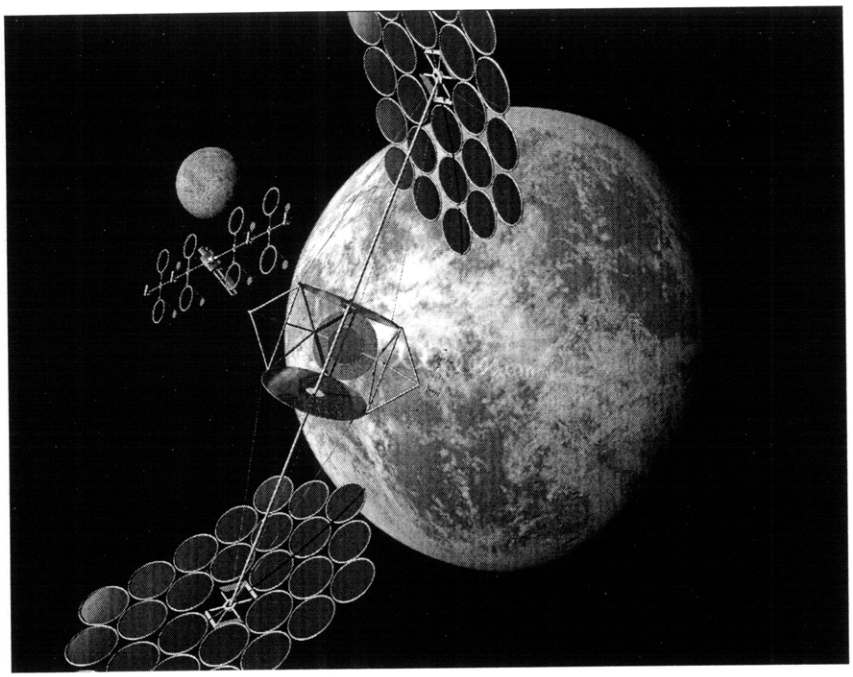

Figure 1.3. Integrated Symmetrical Concentrator (ISC) solar power satellite in geosynchronous orbit (NASA Concept [62]).

Teams with multiple robots will be necessary because the sub-assemblies are too large and flexible for manipulation by a single robot [102]. Also, heterogeneous teams of robots permit specialization resulting in increased effectiveness and reliability, as illustrated in Figure 1.1. These teams might include remote free-flying robots (with thrusters) and free-floating observation robots (without thrusters) for measuring the system's state, inspection and fault detection, worker robots for the transportation and manipulation of components, and robots that can walk across structures and perform fine manipulation for assembly and maintenance [97].

However, the control of teams of robots manipulating large space structural systems with complex changing geometry and significant dynamic behavior is not well understood. Structural vibrations present a major problem [28][93][94][95][98]. Vibrations may be large because the components are made of lightweight composite materials that are very flexible and have low damping (less than one percent) [31][74].

Figure 1.4 shows an artist's concept of the James Webb Space Telescope, scheduled for launch in 2013 [50][61]. This deployable space telescope has a primary mirror 6.5 meters in diameter and a sunshield that is approximately 22 meters by 12 meters. Finite element simulations of this structure predict the first mode for the sunshield membrane to be 0.404 Hertz and the first mode of the sunshield structure to be 1.103 Hertz [65]. Controlling vibrations with such low modes and little natural damping is challenging. Future space telescopes are expected to be substantially larger and more flexible.

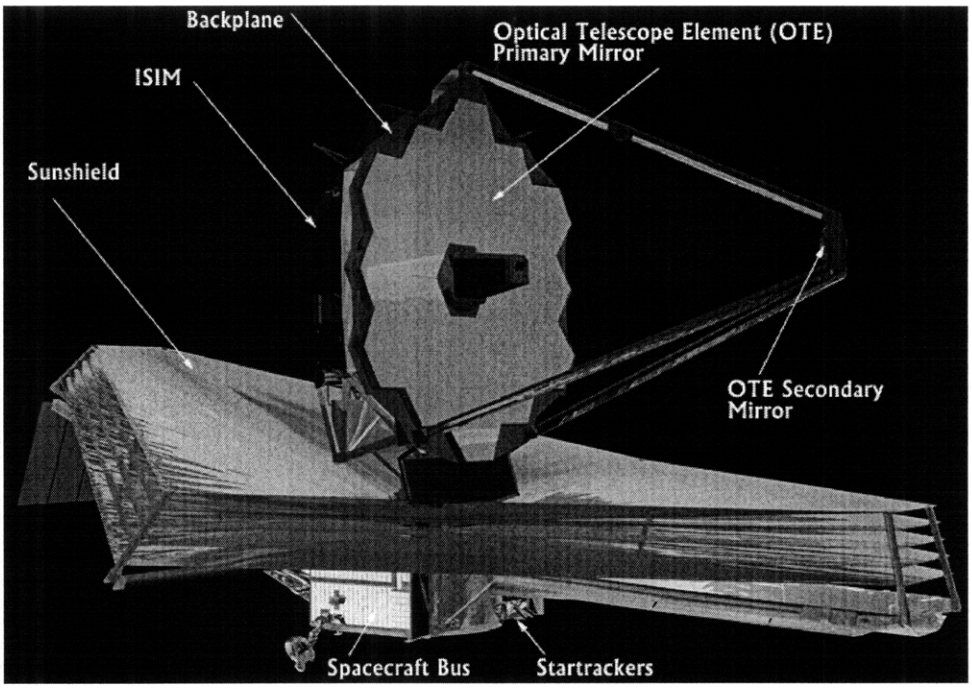

Figure 1.4. Artist concept of the James Webb Space Telescope [61].

The teams of space robots constructing large flexible space structures will need to control the structural vibrations while dealing with the complications of working in a space environment. Dynamic interaction forces between space robots and large flexible structures can excite undesirable structural vibrations; these vibrations can make it difficult to connect assemblies, create delays while waiting for vibrations to damp out or cause robots and structures to collide and damage each other. Practical considerations

such as the robots' high joint friction and nonlinear thruster actuation also make the construction and assembly of large flexible space structures using space robots challenging.

The objective of this thesis is to develop control algorithms to enable teams of space robots to manipulate and assemble large flexible space structures while minimizing residual vibration and operating in limited time, subject to limited sensory information and actuation.

1.2 Background Literature

Mission concepts for the construction of future large space solar power structures stations have been proposed that require space robots to perform manipulation and assembly tasks [17][102]. For the construction of such large structures, it is necessary to transport raw materials to space, build sub-assemblies, and then assemble these sub-assemblies into larger structures on orbit. Space robots have been studied for assembly tasks [24][51][98]. Assembly of simple structural elements such as rod or beam components has been experimentally demonstrated in the laboratory but no demonstration missions have been flown [77]. On-orbit assembly of large flexible structures by robots is especially challenging. The disturbing effects of the dynamic interactions between the structures and the robots make structural vibrations an important problem [95][98]. Space robots need to maneuver the components so as not to induce residual vibration in the structures [95].

Practical issues such as weight, complexity and reliability limit available sensing in space [12]. Limited sensing further complicates the control of these robots. For effective control, sensors must measure the structure's state including vibration and rigid body motions. Fixed sensors such as accelerometers mounted on a large space structure

can be used by state feedback controllers to reduce the structure's vibration [19][31][74]. Accelerometers can acquire high frequency data but only at a limited number of locations. Remote sensors such as vision sensors and laser range finders can see large areas of the structure but are limited by scan rate. These measurements are critical, but effective sensor fusion and estimation methods have been developed to estimate mass properties, vibration modes, as well as the rigid body motions for large space structures [3][4][46][48][49]. The methods use a modified Kalman filter to fuse high-bandwidth but spatially sparse accelerometer data with low-bandwidth vision data [11][18][100]. These methods can be used to compensate for the limits of each type of sensor [26].

Space robots need to perform high precision motion and force control using their thrusters and manipulators to maneuver the flexible space structures effectively and precisely. However, the movement of a space robot's manipulator can disturb its spacecraft base; control algorithms for space manipulators have been developed to compensate for these disturbances [27][71]. Precise control of space robots relies on precise actuation and the ability to measure forces and torques. Light-weight space systems with high gear ratio transmissions using dry lubrication result in high levels of nonlinear Coulomb joint friction that corrupt the fidelity of the actuator's outputs [21][64]. This problem is particularly critical for the approach proposed here, where the robots are used as precise force sources. Similarly, thrusters or reaction jets used by the robots are also highly nonlinear and imprecise [80]. Thruster performance is sensitive to thermal changes and variation in fuel supply level. Errors in the space robot thruster forces degrade these systems' force control capability. Adaptive and sensor-based methods have been developed to compensate for joint actuation nonlinearities but are not robust to unmodeled dynamics [73][84]. For this work, control methods called Space Base Sensor Control have been developed to compensate for nonlinear thruster behavior [8][9]. These methods are an extension of Base Sensor Control [58][59][60]. The

compensation algorithms are used in this work to achieve the precise control required by space robots.

The coordinated control of multi-robot teams to manipulate large flexible space objects has not been well studied. Studies have looked at cooperative control of teams of robots on earth for tasks such as exploration, clustering in formation, or pushing objects [16][76]. Teams of mobile robots have demonstrated coordinated behavior with leader-follower formations [101]. On-orbit multi-robot formation flying has been studied [36][54][56][90]. However, these studies did not generally consider dynamic interactions between teams of robots, a major issue to be addressed in this study. Here the robots and the structures are connected. Motion of one component of the system disturbs the other components. This problem is made more complex because the size of the robots is expected to be small (typically 2-20 meters) compared to the size of the structural elements they will need to manipulate (100-200 meters). To mitigate these coupling disturbances, the robots must be able to control the interactive forces they apply to the structures. Previous studies of dynamic interactions between robot teams have been limited to cases where the robots were not free-floating or free-flying in space such as mobile robots moving rigid beams without flexibility [70][88]. They also considered simple cases of single rigid beams. Previous research has included dynamics in planned trajectories for mobile robots, but without considering flexibility [41]. Preshaping methods can reduce vibration but the system model must be well known (not necessarily true for systems under construction) [15][81][83][92]. When vibration has been considered for transportation problems, it is treated as a disturbance [33][89]. The previous studies did not attempt to minimize the vibrations of the transported structures or control the dynamic interactions of the system.

Recently, studies have examined multi-robot on-orbit assembly for cases with dynamic interactions between robots. An interesting approach to beam assembly uses

tethers [29]. However, stability problems were experienced in initial verification tests with air table experiments. A study of space robots mounted on compliant bases manipulating a flexible structure used preplanned force trajectories by constraining vibration and showed that coordinated control is difficult [95]. Simulations of two robots transporting a flexible beam on orbit showed it is possible to reduce fuel consumption over thruster based methods by controlling large motions with thrusters while damping vibrations with the manipulator arms [7][38]. Experimental verification of the method found the method is sensitive to errors and noise but demonstrated reduced vibration and fuel use with the addition of compliance control [68][69]. However, the general problem of manipulating large flexible space structures with dynamic interactions using coordinated control of multi-robot teams remains a challenging problem that has not been solved [26]. There is no general architecture for the control of coordinated construction of large flexible space structures by teams of robots.

1.3 Contributions of this Thesis

This thesis addresses the problem of manipulating and assembling large scale flexible structures on orbit using teams of space robots. It solves the problem by exploiting the unique dynamics of the application and taking advantage of the frequency separation between the structures and the robots. The dynamics of the system consist of nonlinear partial differential equations (the structures) and nonlinear ordinary differential equations (the robots). The approach proposed here is to transform this system into a set of time-varying linear equations by linearizing about a nominal trajectory. This system is controlled by decoupling the control of the structures from control of the robots. The system can be decoupled assuming the highly flexible structures have low natural frequencies while the robots are high bandwidth and high frequency. Decoupling the

control allows the robots to serve as interactive force sources that apply forces to the structures. Linear optimal control methods determine the forces needed to position the structures while minimizing their vibration. This approach also considers limited sensing and actuation and provides compensation approaches. Simulation and experimental studies demonstrate the strengths and limitations of the method.

1.4 Thesis Organization

The thesis has six chapters. This chapter presents the motivation and background for the thesis. Chapter 2 describes the general solution approach of the thesis. It describes the system model and develops the controller. With this as a basis, Chapter 3 discusses details of the approach and issues with the practical control of space robots with limited sensing and actuation. It includes a compensation method that is used to determine minimal sensing and sensor placement. Chapter 4 describes simulation studies and results. Using the general approach given in previous chapters, the simulation cases explore tasks necessary for the construction of a large flexible space structure such as a space telescope. Chapter 5 describes the experimental system. A team of space robots floating on gas bearings on a granite table perform experiments manipulating flexible elements. Chapter 5 also presents the experimental results. Chapter 6 summarizes the thesis and suggests directions for future work.

The appendices include additional information supporting the main body of work. Appendix A discusses stability considerations of the general approach. Appendix B presents the results from studies of limited sensing and actuation, and includes details of the work described in Chapter 3. Appendix C gives a detailed description of the experimental system components and includes discussion of the system limitations and practical considerations.

CHAPTER

2

GENERAL SOLUTION APPROACH

This thesis examines the problem of transporting and assembling large scale flexible structures on orbit using teams of space robots. This chapter describes the general solution approach. Section 2.1 and Section 2.2 describe the scope of systems considered in this work. Then the general method is presented starting in Section 2.3. A linear time-varying model of the system is derived in Section 2.4 and issues related to the choice of trajectory are covered in Section 2.5. The controller is developed in Section 2.6 and stability is discussed in Section 2.7.

2.1 Flexible Space Systems

The space systems considered in this work consist of flexible elements and teams of space robots. Space systems are typically lightweight and flexible due to the cost of launching materials into orbit. The flexible elements may be large, hundreds of meters across. It is assumed that the structures' mode shapes and frequencies are known within a certain tolerance. Disturbances from thermal warping, solar pressure, and gravity gradient effects are ignored because they are beyond the scope of this thesis. The effect of orbital mechanics is neglected since in many cases the time scale for assembly operations (at most a few minutes) is shorter than the orbital period (about 90 minutes in Low Earth Orbit). The orbit is assumed to be high enough that aerodynamic effects are small.

2.2 Teams of Space Robots

Figure 2.1 shows a conceptual model of an assembly space robot. This three-dimensional robot has two manipulators with multiple degrees of freedom. The robot shown in the figure has rotary joints although some space robots are expected to have translational joints. Free-flying space robots need thrusters to control large motions but have limited supplies of fuel. Space robots may have reaction wheels for attitude control. For the robotic systems studied here, the spacecraft and links are assumed to be 3D rigid bodies. Fuel sloshing is not considered. Nonlinear actuation characteristics and limited sensing that can degrade the system performance are discussed in detail in Chapter 3.

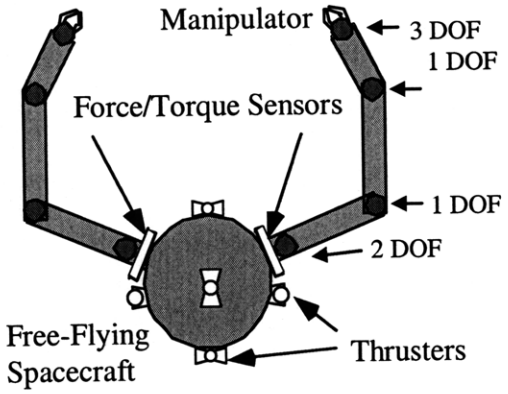

Figure 2.1. Conceptual model of multi-manipulator free-flying space robot.

2.3 Solution Approach

A control approach called *Assembly Manipulation Control* is proposed to enable the construction of large flexible space structures on orbit by teams of robots. The approach decouples the control of the high-frequency robots from the control of the low-frequency structures. Decoupling the control allows the robots to serve as interactive force sources that apply forces to the structures.

For the space systems considered here, the system dynamics can be represented by nonlinear partial differential equations (the structures) and nonlinear ordinary

differential equations (the robots). However, key to this work is that these equations can be linearized about a nominal trajectory resulting in a large system of equations that are slowly time-varying. The resulting system is time-varying because the structures may undergo large displacements. When linearized, the time-varying equations can be effectively controlled. With this transformation, the system can be decoupled and the control of the structures separated from the control of the robots. Linear optimal control methods determine the forces needed to position the structures while minimizing their vibration. Control forces are found that make the system follow the nominal motions while minimizing vibration.

2.4 Modeling Space Systems

The control approach requires a model of the system. This section describes the process of modeling the space structures and derives the state space equations of motion using Lagrange's equations. The nonlinear equations are linearized about a time-varying trajectory using Gardner's method [30]. In his work, the equations of motion are first developed in perturbation coordinates and then are simplified based on engineering analysis of the relative contributions of terms.

For the examples shown in this thesis, a simple finite element approach is used to find the mode shapes and frequencies [55]. For simulation studies, the method allows forces to be repositioned easily. For larger space systems, finite element models would usually be created from commercial finite element software packages. From vibration analysis, the differential equations for the flexural vibration are known to be partial differential equations (PDEs) of the form:

$$-\frac{\partial^2}{\partial \mathbf{z}^2}\left(\mathbf{EI}(\mathbf{z})\frac{\partial^2 \mathbf{w}(\mathbf{z},t)}{\partial \mathbf{z}^2}\right)+\mathbf{f}(\mathbf{z},t)=\mathbf{m}(\mathbf{z})\frac{\partial^2 \mathbf{w}(\mathbf{z},t)}{\partial t^2} \tag{2.1}$$

where $\mathbf{z}$ is the spatial variable, t is time, $\mathbf{w}(\mathbf{z},t)$ is the displacement from equilibrium, $\mathbf{f}(\mathbf{z},t)$ are applied forces, $\mathbf{m}(\mathbf{z})$ is the mass density, $\mathbf{E}$ is the modulus of elasticity and $\mathbf{I}(\mathbf{z})$ is the moment of inertia ($\mathbf{EI}(\mathbf{z})$ is known as the flexural rigidity) [5][40][55].

Finite element methods or assumed displacement functions allow approximation by nonlinear ordinary differential equations (ODEs). Multiple methods are available for finding these equations. For example, assume the displacement from the nominal position $\mathbf{w}$ can be written as a function of shape functions $\boldsymbol{\varphi}_i(\mathbf{z})$ that satisfy the boundary conditions and that $\mathbf{u}_{di}(t)$ are the time-varying displacements at the nodes:

$$\mathbf{w}(\mathbf{z},t) = \sum_{i=1}^{m} \boldsymbol{\varphi}_i(\mathbf{z})\mathbf{u}_{di}(t) \tag{2.2}$$

This displacement function is used to find the kinetic energy:

$$T(t) = \frac{1}{2}\int \mathbf{m}(\mathbf{z})\left[\frac{\partial \mathbf{w}(\mathbf{z},t)}{\partial t}\right]^2 d\mathbf{z} \tag{2.3}$$

and potential energy:

$$V(t) = \frac{1}{2}\int \mathbf{EI}(\mathbf{z})\left[\frac{\partial^2 \mathbf{w}(\mathbf{z},t)}{\partial \mathbf{z}^2}\right]^2 d\mathbf{z} \tag{2.4}$$

Virtual work is used to find the forces associated with the coordinates from the distributed forces $\mathbf{f}(\mathbf{z},t)$:

$$\delta \mathbf{W} = \int \mathbf{f}(\mathbf{z},t)\delta \mathbf{w}(\mathbf{z},t)d\mathbf{z} \tag{2.5}$$

The virtual work is combined with kinetic and potential energies from Equations (2.3) and (2.4) in Lagrange's equation:

$$\frac{d}{dt}\left(\frac{\partial T}{\partial \dot{q}_j}\right) - \frac{\partial T}{\partial q_j} + \frac{\partial V}{\partial q_j} = W_j, \quad j = 1,2,...,n \tag{2.6}$$

where q_j is the jth of n generalized coordinates. This results in the second order equations of motion:

$$\mathbf{M}(\mathbf{u}_d)\ddot{\mathbf{u}}_d + \mathbf{D}(\mathbf{u}_d, \dot{\mathbf{u}}_d)\dot{\mathbf{u}}_d + \mathbf{K}(\mathbf{u}_d)\mathbf{u}_d = \mathbf{B}_f(\mathbf{u}_d)\mathbf{F}(t) \tag{2.7}$$

where $\mathbf{u}_d$ is the generalized displacement vector, $\mathbf{M}(\mathbf{u}_d)$ is the mass matrix, $\mathbf{D}(\mathbf{u}_d, \dot{\mathbf{u}}_d)$ is the damping matrix $\mathbf{K}(\mathbf{u}_d)$ is the stiffness matrix, and $\mathbf{B}_f(\mathbf{u}_d)$ is a coefficient matrix. For space structures, the damping ratios are typically not known exactly. For convenience, proportional damping is generally assumed for the structural modes [31]. The coefficient matrices are converted to linear slowly time-varying matrices using the approach in [30].

The displacement coordinates $\mathbf{u}_d$ are usually transformed to modal coordinates $\mathbf{q}_m$. Modal coordinates allow model reduction to reduce the order of the system, particularly when the original system has a large number of high frequency components that do not substantially contribute to the system model. Additionally, system identification methods often provide their results in modal coordinates. The second order equations of motion in modal coordinates are:

$$\ddot{\mathbf{q}}_m + 2\mathbf{Z}\boldsymbol{\Omega}\dot{\mathbf{q}}_m + \boldsymbol{\Omega}^2\mathbf{q}_m = \mathbf{B}'_f\mathbf{F} \tag{2.8}$$

Equation (2.8) can be written in state space form:

$$\dot{\mathbf{x}} = \mathbf{A}(t)\mathbf{x} + \mathbf{B}(t)\mathbf{u} \tag{2.9}$$

where $\mathbf{x}$ is the state vector containing position and velocity components of the perturbation components, $\mathbf{u}$ is the control vector and $\mathbf{A}(t)$ and $\mathbf{B}(t)$ are coefficient matrices. An important characteristic is that these linearized matrices are slowly time-varying to allow effective control of structures undergoing large displacements and rotations [30].

The control algorithms require the positions and velocities of specific points where forces are applied to the flexible structure. These positions and velocities are collected in an output vector $\mathbf{y}$. This output vector can be found from the perturbation coordinates in the state vector $\mathbf{x}$ and written in the matrix form:

$$\mathbf{y} = \mathbf{C}(t)\mathbf{x} + \mathbf{y}_e(t) \tag{2.10}$$

where $\mathbf{y}_e(t)$ is the nominal value of the output vector at time t, and $\mathbf{C}(t)$ is the output matrix. Note that the formulation in Equation (2.10) can be transformed to another commonly used notation $\mathbf{y}' = \mathbf{C}(t)\mathbf{x}$ by defining $\mathbf{y}' = \mathbf{y} - \mathbf{y}_e(t)$.

2.5 Trajectory Planning

The nominal trajectories are found from the rigid body model of the system. A number of methods have been developed to find the motion of free-floating systems. The path for a beam transported in space can be determined by minimizing fuel consumption [38]. Preshaping methods can be used to find trajectories [15][81][83][92]. Nonholonomic path planning methods have been developed for space manipulators [44][91]. These methods can be used to find the nominal motions of the structural elements for assembly.

2.6 Control Approach

A controller is developed to make the system follow the nominal motions while minimizing vibration. Figure 2.2 shows a block diagram of the controller. The inner loop shows a space robot controlled as a force source. The space robot's end-effectors apply forces to the large flexible space structure. The outer loop shows the large flexible space structure controlled by the applied forces.

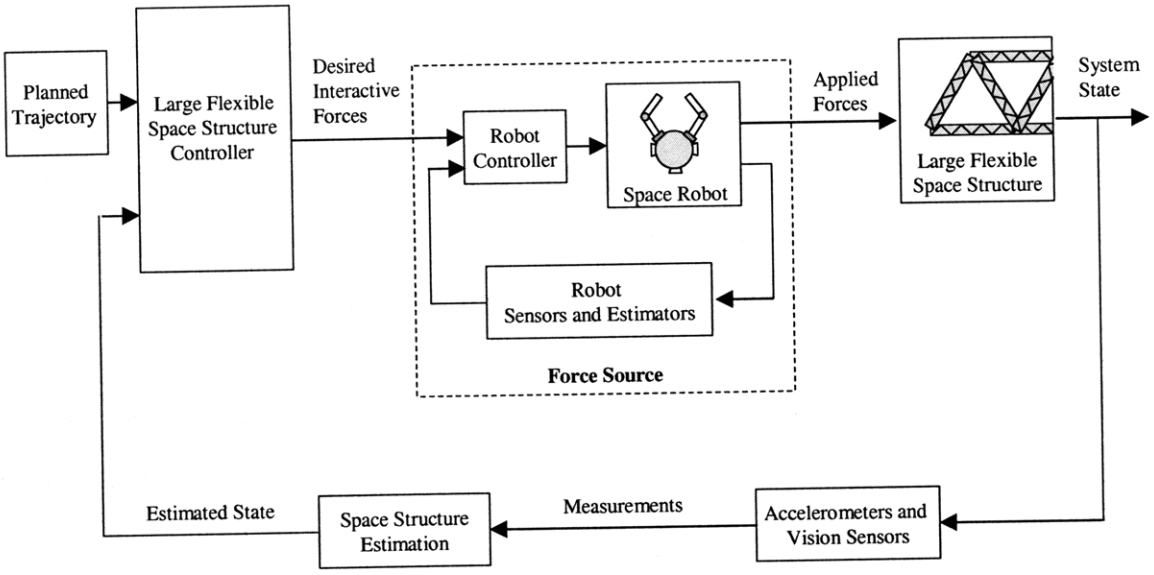

Figure 2.2. Block diagram of large space structure assembly controller.

For transportation and assembly tasks, the objective is to move structures to a desired position and bring the structures' connection points together while minimizing vibration and actuator effort. During transportation, the structures may undergo large displacements. To perform the assembly tasks, the robots apply forces to the structure with their end-effectors. In a previous study, preplanned forces for two robots moving a flexible structure were calculated by constraining vibration and finding a pseudoinverse solution [93][94]. The method distributed the effort among the robots and reduced the vibration induced to the supporting structure. That work also demonstrated the challenging problem of coupled robot and structure dynamics.

For this work, optimal control methods are used to find desired interactive forces [1][10][28]. Optimal methods minimize vibrations to all the structures. Because the system is time-varying linear, linear quadratic (LQ) methods are used to find the optimal control. The resulting control prescribes the forces the robots apply to the structure. The control of the individual robots can be decoupled from the control of the larger system. Figure 2.2 shows this in the inner loop. The robots are controlled to act as force sources that apply forces to the large flexible structures.

The determination of the robot forces is formulated as a finite-time optimal tracking control problem [10]. Given a system:

$$\dot{\mathbf{x}} = f(\mathbf{x},\mathbf{u},t) \tag{2.11}$$

and its initial state $\mathbf{x}(t_0)$, the objective is to find the optimal control $\mathbf{u}^*(t)$, $t \in [t_0, t_f]$ that minimizes the performance index J:

$$J = S\big(\mathbf{x}(t_f), t_f\big) + \int_{t_0}^{t_f} L\big(\mathbf{x}(t),\mathbf{u}(t),t\big)dt \tag{2.12}$$

The function S specifies the cost at the terminal time t_f and the function L includes the cost of applying control forces while following a trajectory from the initial time t_0 to the terminal time.

Using the system equations from Equations (2.9) and (2.10), the performance index to follow a trajectory $\tilde{\mathbf{x}}(t)$ with minimal control effort $\mathbf{u}$ can be written as the linear quadratic cost function:

$$\begin{aligned} J = {} & [\mathbf{x}(t_f) - \mathbf{x}_{des}]^{\mathrm{T}} \mathbf{M}_f [\mathbf{x}(t_f) - \mathbf{x}_{des}] \\ & + \int_{t_0}^{t_f} \left\{ [\mathbf{x}(t) - \tilde{\mathbf{x}}(t)]^{\mathrm{T}} \mathbf{Q} [\mathbf{x}(t) - \tilde{\mathbf{x}}(t)] + \mathbf{u}(t)^{\mathrm{T}} \mathbf{R}\mathbf{u}(t) \right\} dt \end{aligned} \tag{2.13}$$

The weighting matrices $\mathbf{M}_f$ and $\mathbf{Q}$ are assumed to be positive semidefinite and $\mathbf{R}$ is positive definite (since $\mathbf{R}$ must be inverted in the solution). The first term of the function is the cost of moving the structures to their desired position and velocity state $\mathbf{x}_{des}$. The first term inside the integral is the cost of following a specific trajectory. (When no trajectory is specified only residual vibration is minimized and $\mathbf{Q} = \mathbf{0}$). The last term of the cost function in Equation (2.13) specifies the actuation (or fuel) cost. For the transportation maneuver, the actuation cost includes the external forces that are applied to the system by the limited reaction jet thrusters. The state vector $\mathbf{x}$ contains the vibration modes, so vibration suppression is accomplished by specifying the weighting matrices

M_f and $\mathbf{Q}$. The relative weights of $\mathbf{M}_f$, $\mathbf{Q}$ and $\mathbf{R}$ can be adjusted to trade off the goals of vibration suppression and fuel use.

The desired trajectory is usually given in output coordinates $\tilde{\mathbf{y}}(t)$, but the desired trajectory $\tilde{\mathbf{x}}(t)$ in the performance index is expressed in state coordinates. This allows the maximum number of constraints on the state without creating a conflict of objectives. The relationship between state coordinates and output coordinates is given by:

$$\tilde{\mathbf{x}}(t) = \mathbf{C}^{\mathrm{T}}\left(\mathbf{C}\mathbf{C}^{\mathrm{T}}\right)^{-1}\tilde{\mathbf{y}}(t) \tag{2.14}$$

where the matrix $\mathbf{C}$ is from Equation (2.10) [1].

An assembly example is shown in Figure 2.3. The objective of this task is to perform fine assembly by bringing the endpoints together without inducing vibrations that might damage the structure or the robots. For the case shown in the figure, the first term of the cost function can be written:

$$S\left(\mathbf{x}(t_f), t_f\right) = \left\| \mathbf{r}_a(t_f) - \mathbf{r}_b(t_f) \right\|^2 \tag{2.15}$$

where $\mathbf{r}_a$ and $\mathbf{r}_b$ are inertial vectors to the endpoints. The trajectory point can be written in terms of the $\mathbf{r}_a$ and $\mathbf{r}_b$ vectors and converted to the terminal constraint:

$$S\left(\mathbf{x}(t_f), t_f\right) = [\mathbf{x}(t_f) - \mathbf{x}_{des}]^{\mathrm{T}} \mathbf{M}_f [\mathbf{x}(t_f) - \mathbf{x}_{des}] \tag{2.16}$$

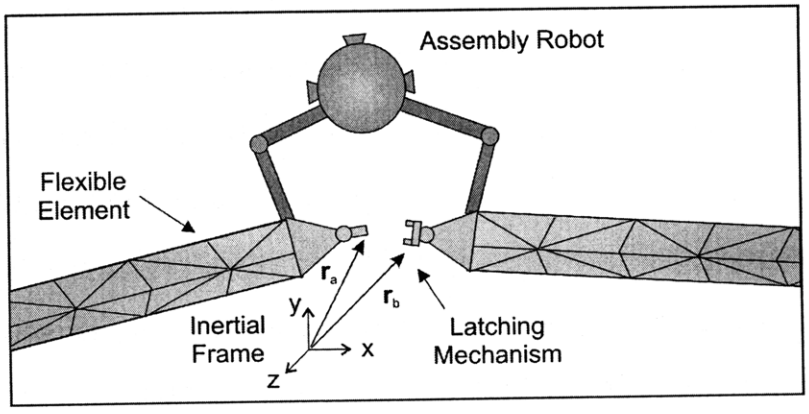

Figure 2.3. Space robot performing fine assembly.

Once the optimal control problem is posed, the optimal forces can be determined. To solve the optimal control problem, the Hamilton-Jacobi-Bellman (H.J.B.) partial differential equation is written [10]:

$$\frac{\partial J}{\partial t_r} = \min_{\mathbf{u}(t)}\{[\mathbf{x}(t)-\tilde{\mathbf{x}}(t)]^{\mathrm{T}}\mathbf{Q}[\mathbf{x}(t)-\tilde{\mathbf{x}}(t)]+\mathbf{u}(t)^{\mathrm{T}}\mathbf{R}\mathbf{u}(t)+ (\nabla_x J)^{\mathrm{T}}[\mathbf{A}\mathbf{x}+\mathbf{B}\mathbf{u}]\} \tag{2.17}$$

where time remaining is defined as $t_r \equiv t_f - t$, and ∇_x is the gradient. The boundary conditions are similar to those given in Equation (2.16). The H.J.B. equation is solved using the Principle of Optimality. The details of the solution derivation can be found in the references [1][10]. The optimal control solution is found:

$$\mathbf{u}^*(t) = -\mathbf{R}^{-1}\mathbf{B}^{\mathrm{T}}\left\{\mathbf{W}(t_r)\mathbf{x}(t)+\tfrac{1}{2}\mathbf{V}(t_r)\right\} \tag{2.18}$$

The matrix $\mathbf{W}(t_r)$ is found from the matrix Riccati equation:

$$\frac{d\mathbf{W}}{dt_r} = \mathbf{W}(t_r)\mathbf{A}+\mathbf{A}^{\mathrm{T}}\mathbf{W}(t_r)-\mathbf{W}(t_r)\mathbf{B}\mathbf{R}^{-1}\mathbf{B}^{\mathrm{T}}\mathbf{W}(t_r)+\mathbf{Q} \tag{2.19}$$

and the matrix $\mathbf{V}(t_r)$ can be found from $\mathbf{W}(t_r)$:

$$\frac{d\mathbf{V}}{dt_r} = \mathbf{A}^{\mathrm{T}}\mathbf{V}(t_r)-\mathbf{W}(t_r)\mathbf{B}\mathbf{R}^{-1}\mathbf{B}^{\mathrm{T}}\mathbf{V}(t_r)-2\mathbf{Q}\tilde{\mathbf{x}}(t) \tag{2.20}$$

with the end conditions $\mathbf{W}(t_r=0)=\mathbf{M}_f$ and $\mathbf{V}(t_r=0)=-2\mathbf{M}_f\mathbf{x}_{des}$. These equations can be solved numerically to find the optimal control forces for the robots to apply to the structures. The matrices $\mathbf{W}$ and $\mathbf{V}$ in Equations (2.19) and (2.20) are computed with preprocessing, and Equation (2.18) is the control used inside the feedback loop. A closed-form solution is available to the matrix Riccati equation via the Hamiltonian matrix and a similarity transformation to its Jordan form. However, this form was found to be numerically ill-conditioned in practice, so numerical integration is used in this work for finding the optimal control.

2.7 Stability and Robustness of the Controller

The stability of the closed-loop time-varying system requires that the system be stabilizable and detectable [1][10]. Stabilizability is a slightly weaker form of controllability where all the uncontrollable modes must be stable. Detectability is a weaker form of observability, and requires that the unobservable modes of the system be stable. These conditions are met for the space systems and control algorithm presented in this thesis. Appendix A discusses these properties in detail.

CHAPTER

3

LIMITED SENSING AND ACTUATION

The previous chapter presented the general approach to constructing large flexible structures on orbit. This chapter discusses issues related to the implementation of this approach for actual systems and discusses the problems associated with limited sensing and actuation.

Precise control of space robots is important for space missions such as large space structure construction [43][78][103]. However, practical factors such as unpredictable actuator behavior and limited sensing in space can degrade performance; these are discussed in Section 3.1. Sensing capabilities in space robots to measure and compensate for actuator uncertainty are limited by the practical issues of weight, complexity and reliability. Sensors to measure the motions and vibrations of the large space structures face similar issues.

Compensation methods, discussed in Section 3.2, are constrained by the challenges of space systems. A method called Space Base Sensor Control (SBSC) is presented in Section 3.3 [8]. SBSC an extension of the Base Sensor Control (BSC) method that has been developed for fixed-based terrestrial robots [58][60]. SBSC allows multi-actuator sensing for a space robot with a reduced number of actuators. A force/torque sensor is mounted between a space robot's spacecraft and its manipulators and is used to identify manipulator joint actuator outputs while simultaneously estimating spacecraft thruster forces and moments. Then the SBSC method is used to examine the best placement and the minimum number of force/torque sensors for a given space robot

to simultaneously measure joint and spacecraft actuation; Section 3.4 describes this approach [9]. Force/torque sensors isolate system sections that are reduced to canonical elements. This allows the analysis of a small number of elements. The results of the analysis of the canonical elements are combined to determine the number of sensors needed for the original system. The chapter concludes in Section 3.5 with a discussion of the application to the control of large flexible structures. Appendix B presents the details of the approach and simulation results for Space Base Sensor Control.

Accurate estimates of vibration modes, relative mass properties and the rigid body motions for large flexible space structures is also critical to the control algorithms. However, effective methods have been developed to determine these properties, and thus this chapter focuses on space robots issues with sensing and actuation [3][4][46][49].

3.1 Limits on Sensing and Actuation in Space

The robots used for space missions need to perform precise motion and force control using their manipulators and reaction jets. Figure 2.1 shows a concept of a space robot with two manipulators. Sensing for the robot may include joint encoders, force/torque sensors, gyroscopes, inertial measurement units (IMUs), etc. [45]. The actuation may include joint motors, spacecraft thrusters, and reaction wheels. For the robots, actuation errors can degrade the desired performance if not compensated using inner closed-loop force/torque control. For space applications, the need to limit system weight results in high gear ratio drives, while conditions in space require the use of dry lubrication in robot joints and transmissions. The result is that the robot joints have high non-linear Coulomb friction [2]. Reaction jets or thrusters are used to control the large motions of free-flying space robots. These thrusters are controlled with highly nonlinear pulse width modulation (PWM) or pulse width-pulse-frequency modulation (PWPFM)

[45][80]. Thruster performance is sensitive to such effects as thermal changes and variation in fuel supply level. These joint and thruster actuation characteristics can degrade system performance.

The problem of limited sensing of the space structures makes the control of space robots difficult. For effective control, sensors must be able to measure the structures' dynamic state including rigid-body motions, geometric shape, and vibrational motion. Fixed sensors such as accelerometers or strain gages mounted on flexible space structures can acquire high frequency data but only at a limited number of locations. To accurately estimate vibration, a large number of sensors would be required, resulting in increased cabling, power requirements, cost, and weight. Also, accelerometers attached to the structure are not able to measure constant velocity, rigid-body motions of the system. Remote vision sensors such as stereo cameras, laser range finders, and LIDAR mounted on observer robots can see large areas of the structure but are limited by scan rate. Data may be missing when parts of the structure are occluded by other objects. Additionally, range sensor data can be noisy, and the harsh lighting conditions in space degrade the quality of visual images. Nontheless, methods have been developed to compensate for the limits of each type of sensor [3][4].

3.2 Compensation Methods

A number of effective methods for dealing with imprecise actuation approaches in conventional ground based manipulators have been developed, including sensor-based methods, adaptive compensation, and model-based methods. These methods have principally focused on friction compensation. When sensors are available, measurement-based control provides direct feedback of actuation effort for closed-loop force or torque control [73][99]. These methods are desirable because they do not require a model and

hence are robust to system changes with time. However, for a complex space robot, they would require multiple sensors that increase cost, weight, and complexity and reduce system reliability. Therefore, developing a method that uses limited sensing to measure actuation efforts is desirable.

Adaptive control methods have been developed to estimate unknown joint actuator friction parameters [20][84]. However, especially for high degree-of-freedom space systems, adaptive control formulations can be complex making their implementation difficult [21]. In addition, they have not yet been extended to the identification of attitude control jet forces and moments. Also for space systems, relying on measurement of uncertainty and errors rather than indirect computation is preferred, due to the wide range of environmental conditions that can affect system parameters and the need to avoid dangerous transient behavior during adaptation.

Model-based actuator effort compensation methods use mathematical models to predict actuator behavior [20]. However, these methods would not be robust in the hostile environment of space because model parameters change radically with conditions, load, position, temperature, and wear. Therefore model based compensation is not well suited to space applications. Other methods based on special command profiles to deal with imprecise actuation have been developed, such as high frequency dither [37]. However, these methods have yet to be developed for space applications, in particular for reaction jet uncertainty.

3.3 Space Base Sensor Control Approach

The approach proposed to identify actuator efforts from limited sensor data using appropriate kinematic and dynamic models is an extension of the Base Sensor Control (BSC) method that has been developed for fixed-based terrestrial robots [58][60]. BSC

identifies joint torques by placing a single six-axis force/torque sensor between its manipulator and its fixed base. Here, one six-axis force/torque sensor is placed between each manipulator and its spacecraft (see Figure 2.1). It is shown (see Appendix B) that these sensors can simultaneously measure all of the system's actuator efforts including the effects of friction in the manipulator joints and jet reaction forces and torques [8]. The measurements can be used in inner force or torque control loops to eliminate torque and thruster actuation error, improving the precision control system (see Figure 3.1). These sensors could also be used for continuous monitoring to detect degradation in actuator performance. Appendix B gives the details of this approach. The appendix demonstrates the effectiveness of the Space Base Sensor Control method in simulation.

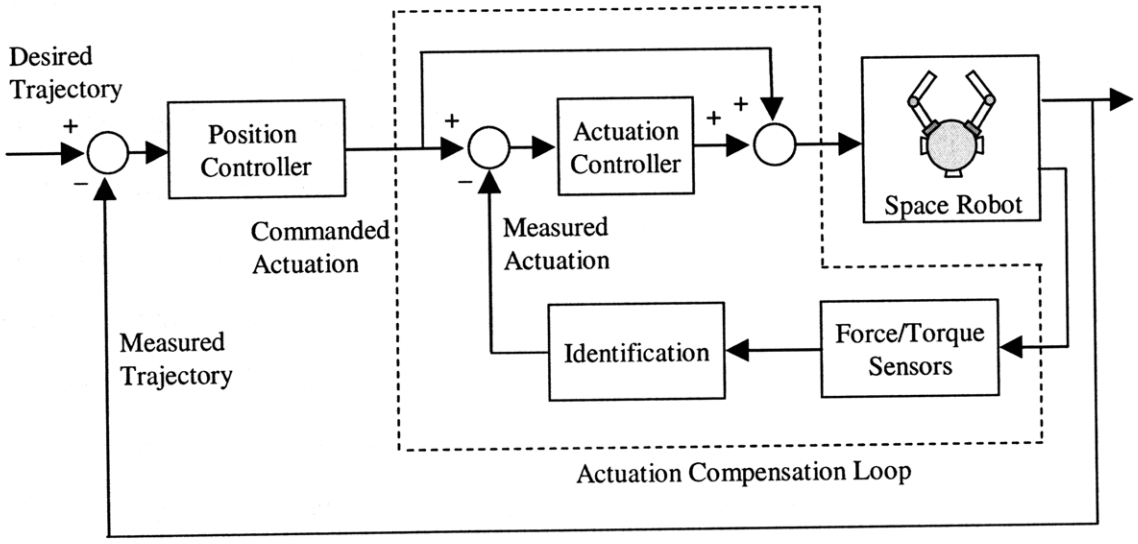

Figure 3.1. Inner loop identifies and compensates for actuator efforts while outer loop tracks desired trajectory.

3.4 Determining Minimal Sensors

The Space Base Sensor Control method can be used to examine the best placement and the minimum number of force/torque sensors for a given space robot to

simultaneously measure joint and spacecraft actuation [9]. This problem could be solved by exhaustive analysis. However, varying the number of manipulators p, the number of links n, reaction jets or not, payload or not, and considering force/torque sensors at the base of the manipulator or at the end-effector, the number of cases c to be considered grows rapidly ($c = 16\,p \times n$). However, most cases are topologically similar and the space of possible solutions can be reduced to a small number of similar cases called canonical elements. The dynamic analysis is needed only for these elements and the results can be applied to more general systems.

The approach taken here is to divide the system at each six-axis force/torque sensor into subsystems. The subsystems are categorized by a small set of canonical elements. The dynamics of the canonical elements are analyzed using Newton's method to find intermediate forces and torques. Finally, the results are applied to the original system to find the minimum number of sensors required to calculate the actual net joint efforts (eliminating the effects of friction) and the actual thruster forces and reaction wheel moments. Appendix B gives the details of this approach.

3.5 Application to the Control of Large Flexible Structures

The precise control of the space robots and the accurate estimation of rigid-body and vibrational modes is important to the performance of the control algorithms presented in this work. The block diagram of the general approach given in Figure 2.2 is reproduced in Figure 3.2 to show the impact of limited sensing and actuation. In this work, the space robots need to act as force sources. When there is imperfect actuation and the force control effort degrades due to influences such as outside disturbances or limited force control bandwidth, this enters the system in the upper dashed block shown in Figure 3.2. One approach to mitigate these influences is to use the Space Base Sensor

Control algorithm discussed in this chapter to control the robots so that they can act as force sources to the flexible structure.

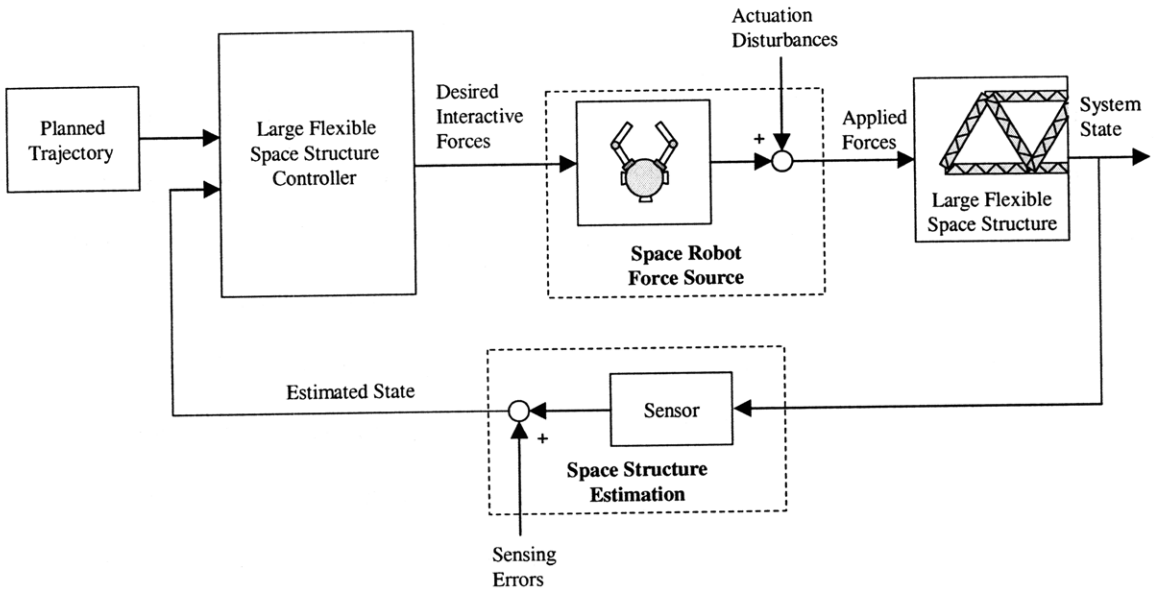

Figure 3.2. Block diagram shows the impact of limited sensing and actuation on the general approach.

CHAPTER

4

SIMULATION STUDIES

This chapter describes the simulation studies performed in Matlab and Simulink to validate the control algorithm and predict its performance. Section 4.1 gives the choice of parameters for the flexible structures and robots along with assumptions for the simulations. The controllers are described in Section 4.2, and metrics to compare their performance are proposed in Section 4.3. The specific cases studied are described in Section 4.4. There, results are presented and the performance of the controllers evaluated. Section 4.5 summarizes the conclusions of the results.

4.1 System Description

The simulation parameters are determined by analysis of potential future large on-orbit structures such as telescopes and space solar power collectors. Future on-orbit structures will be complex and built from flexible elements such as beams and other components. This section explains the choice of parameters and the assumptions made.

4.1.1 Flexible Element Specifications

Researchers have designed a prototypical on-orbit flexible beam for use in a large space solar power collector [51][93][95][96]. Figure 4.1 shows this tensegrity structure, and Table 4.1 gives its parameters. This beam is the basis of the simulation structures, and parameters for the other structures used in simulation are derived in relation to it.

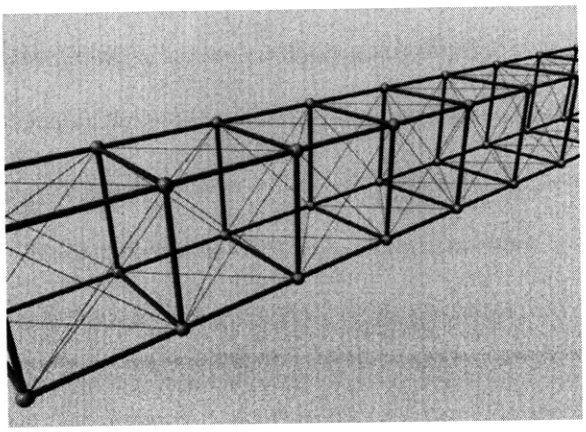

Figure 4.1. Concept for large flexible on-orbit beam [93].

Table 4.1. Simulated flexible beam parameters [93].

Parameters	Values
Length	200 [m]
Width	1 [m]
Height	1 [m]
Mass	600 [kg]
Axial inertia	2×10^6 [kg m^2]
Young's modulus	0.156 [Gpa]
Lowest frequencies	0.18, 0.51, 1.01, 1.85, 2.90, 4.49, 7.48 [Hz]

Finite element models are created for the flexible structure simulations. The finite element models have nodes with three or six displacements, leading to models with three or six rigid-body degrees of freedom, respectively. For the three DOF cases, a beam has transverse flexibility in the plane, transverse flexibility in the orthogonal direction, and axial flexibility. (Torsion is neglected since deflections due to torsion are small when compared to transverse flexibility. For example, a force of 20 Newtons applied to the structure described in Table 4.1 causes a 25 centimeter deflection for a simply supported structure, while applying that same force in torsion at the outer edge to create a torque of 14.14 Newton-meters causes only a deflection of 7×10^{-5} radians or 5×10^{-3} centimeters at the edge. Displacements due to axial compression result in similarly small values.) When multiple flexible elements are combined together to make more complex three-dimensional structures, six displacements per finite element node are used.

4.1.2 Robot Parameters

The parameters for the simulated robots that can transport and maneuver these large flexible structures are estimated from analysis of current space robots and space satellites, such as the Space Station Remote Manipulator System (SSRMS), ETS-VII, and Orbital Express, and projections of future space robot capabilities [35][42][66][72][78]. Huge robots are needed to construct structures that are kilometers across. Robots capable of doing these assembly and transportation tasks are beyond the scope of anything designed to date and the composition of future space robots is a challenge for designers. The workspace of the robots must enable significant motion. For maximum versatility, it is assumed that the space robots have at least two manipulators. The manipulators motors must manipulate and control the large flexible elements described earlier. The spacecraft must support the robot infrastructure including fuel, power supplies, electronics, communications, etc., while minimizing mass to reduce the need for propellant. Finally, the system needs thrusters capable of fine motions for attitude control, but also large enough to perform the transportation maneuvers required for space structure construction. These tradeoffs should be considered for the design of future space robots. For the simulations presented here, Table 4.2 gives the estimated robot parameters.

Table 4.2. Simulated space robot parameters.

Parameters	Values
Manipulators per robot	2
Links per manipulator	2
Manipulator reach	10 [m]
Spacing between manipulator bases	5 [m]
Total mass	600 [kg]
Maximum thrust (large motions)	400 [N]
Maximum thrust (attitude control)	25 [N]

4.1.3 Assumptions

The simulated transportation and assembly simulation cases ignore disturbances from thermal warping, aerodynamic and gravity gradient effects. Relative positioning information about the location of connection points where the structures are to be joined is assumed to be available via on-board cameras or range sensors. Vibration modes are provided from sensor fusion techniques combining on-board accelerometer data that measure high temporal frequencies but low spatial distributions with low temporal high spatial frequency camera or laser range finder data [3][4]. The robot links are assumed to be rigid bodies. The simulated robots are assumed to be able to precisely provide the forces needed. Simulations given in Appendix B demonstrate robotic techniques for precise sensing and actuation despite joint friction and thruster nonlinearities.

4.2 Controllers

Two controllers are compared in the simulations. The first, a rigid-body controller, translates and rotates the structures assuming the structures are rigid. The second controller takes flexibility into account. The flexible controller actively requires the robot and their manipulators to act as force sources to remove vibrations.

The controllers are found using Linear Quadratic techniques described in Chapter 2. For the simulations, one trajectory is used and is calculated using cubic splines. The $\mathbf{M}_f$, $\mathbf{Q}$, and $\mathbf{R}$ cost function matrices are chosen to be diagonal. The initial values in these matrices are determined using Bryson's rule [13]:

$$M_{f,ii} = \text{1/maximum acceptable value of } (x_i(t_f) - x_{i,des})^2$$

$$Q_{ii} = \text{1/maximum acceptable value of } (x_i - \tilde{x}_i)^2$$

$$R_{ii} = \text{1/maximum acceptable value of } (u_i)^2 \qquad (4.1)$$

These initial values are adjusted to improve performance. The gains for rigid-body translations and rotations are set to be effectively the same for the rigid-body controller and the flexible controller. In the simulations, when the state vectors are scaled normalize the modes ($\mathbf{\Phi}^T\mathbf{M}\mathbf{\Phi} = \mathbf{I}$), the gain matrices are also scaled by the software accordingly.

Once the gains are determined, the matrix Riccati equation is integrated numerically to find the control gains along the trajectory. Control gains and control effort are calculated by preprocessing in Matlab. The optimal rigid-body and flexible controllers are designed to output zero forces after the assembly point is reached, because they assume no errors or disturbances in the system. In a real system, there are accumulated errors; a space system would not be left without control, so the simulations switch to a PD controller when the optimal controllers finish to address accumulated or continuing errors and disturbances. Issues of computational burden are beyond the scope of this thesis.

4.3 Performance Metrics

The performance metrics for the controllers determine how well they remove residual vibration and how much non-renewable thruster fuel they consume to perform a maneuver. To perform final assembly, it is assumed that the manipulators use automatic latch mechanisms that join the components together when they are brought within a threshold needed by the mechanism design, here 10 centimeters. Hence, the residual vibration is measured at assembly points, the endpoints for a flexible element or the corners of a flexible frame or structure. The settling time t_s is the time that it takes transients to decay so that the amplitude of vibration is below a given value.

Another important metric is thruster propellant fuel usage. As much as possible of the vibration damping contribution should come from the manipulators, as the thruster

fuel is a non-renewable resource. If the assembly robots did not have manipulators, all damping effort would have to be provided by the thrusters. Using manipulators for vibration damping has been shown to substantially reduce the amount of thruster propellant required [38, 69]. The actuation effort is calculated from the integral of the net forces applied to the structure. The net impulse I_{net} is defined as:

$$I_{net} = \int_0^t \|\mathbf{F}\| dt \tag{4.2}$$

where $\mathbf{F}$ is the applied force. The higher frequency components of this effort and much of the damping effort can come from the manipulators, but the thrusters must provide the net external forces to transport a structure across a distance.

For the assembly cases, there is no transportation and the thruster forces are smaller. The thrusters could be used for active damping to remove structural vibrations during assembly, but most likely will be turned off in order to conserve fuel. For the assembly simulation cases, the thrusters are not used and the robots apply all forces with their end-effectors while operating in free-floating mode.

4.4 Cases Studied

The simulations explore tasks necessary for the on-orbit construction of a large flexible structure such as a space telescope. The first simulation (Case A) shows the assembly of two non-symmetric elements to form a support truss for the telescope (see Figure 4.2). The flexible elements undergo large rotations. For the second simulation (Case B), three robots create a large frame by maneuvering flexible elements and performing fine assembly while avoiding collisions. Finally, for the third simulation (Case C), the assembled frame structure is transported to be attached to the telescope.

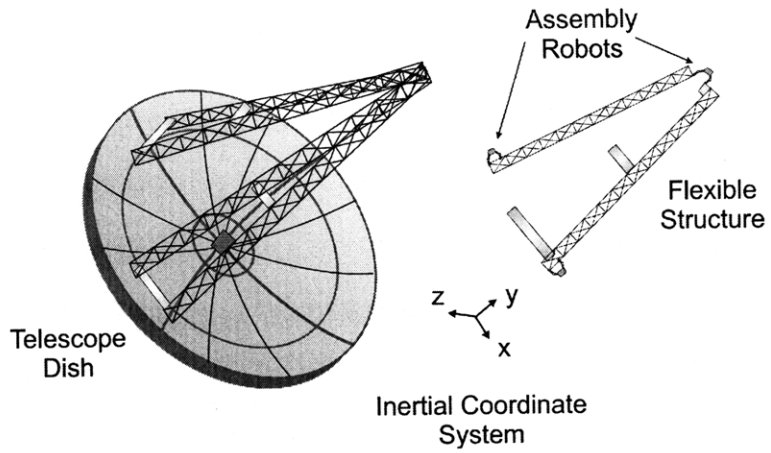

Figure 4.2. Assembly of a support structure for a space telescope. For these figures, the scale is enlarged to make parts more visible.

The simulation results for the telescope truss assembly (Case A) demonstrate the performance of the rigid-body controller and the flexible controller. The need for time-varying systems is demonstrated and the effect of controller bandwidth on the performance of the system is examined. The results for the frame assembly (Case B) and the assembled frame transportation (Case C) simulations show a comparison of the rigid-body and flexible controller performance.

4.4.1 Simulation Case A – Space Telescope Truss Assembly

The first task (Case A) is the assembly of a flexible truss element by three space robots (see Figure 4.2). While being assembled, the flexible elements undergo large displacements and rotations. Figure 4.3 shows a closer view of the assembly maneuver. The structure on the left in the figure is a simple flexible structure. The flexible structure on the right has already been joined with its crossbar sections so the system models are not symmetric. For the case, the outermost transportation robots fire their thrusters to bring the endpoints of the two structures close together. The assembly robot in the middle holds both flexible structures and applies forces to bring the parts together.

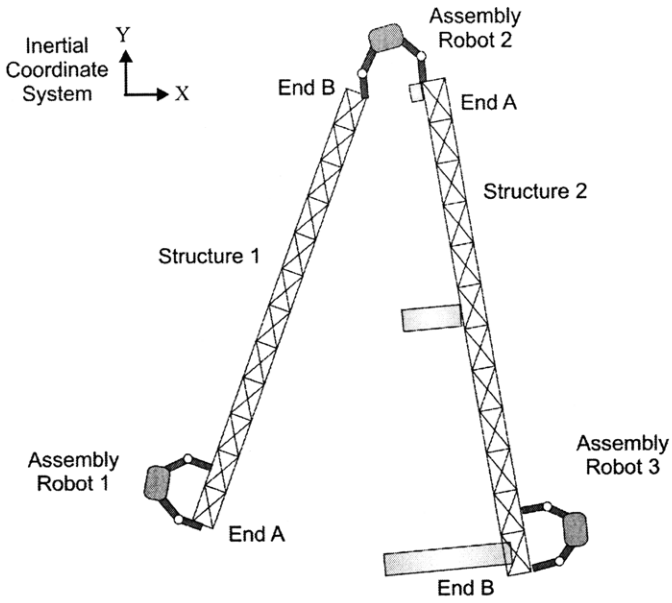

Figure 4.3. Details of assembly maneuver simulation.

The robots and structures in all of the drawings in this section are enlarged to make them more visible. For example, Figure 4.4 shows a rendering drawn to scale; the details of the robots and structures are barely visible.

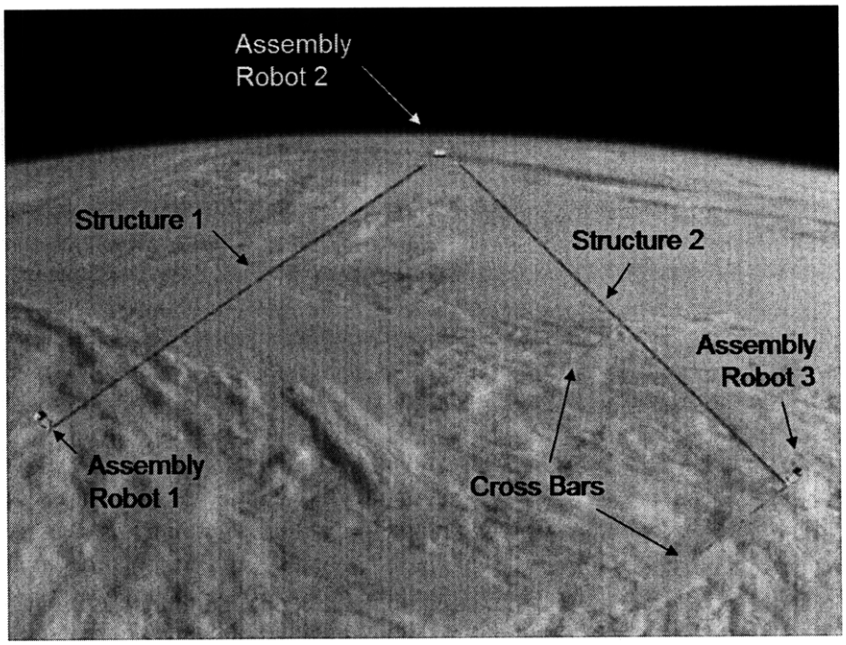

Figure 4.4. Maya rendering of the assembly maneuver case. At scale, the details are barely visible.

The rigid-body model of the structure is given in state space. The flexible model is constructed using finite elements, the cross bars are modeled as rigid masses, and the robots are modeled as force sources. The trajectory for the motion of the flexible element is calculated with a cubic spline fitting the initial and final positions and velocities. Figure 4.5 shows the initial and final positions, along with the orientation of the inertial coordinate system used in the simulation. Table 4.3 gives the parameters for this simulation.

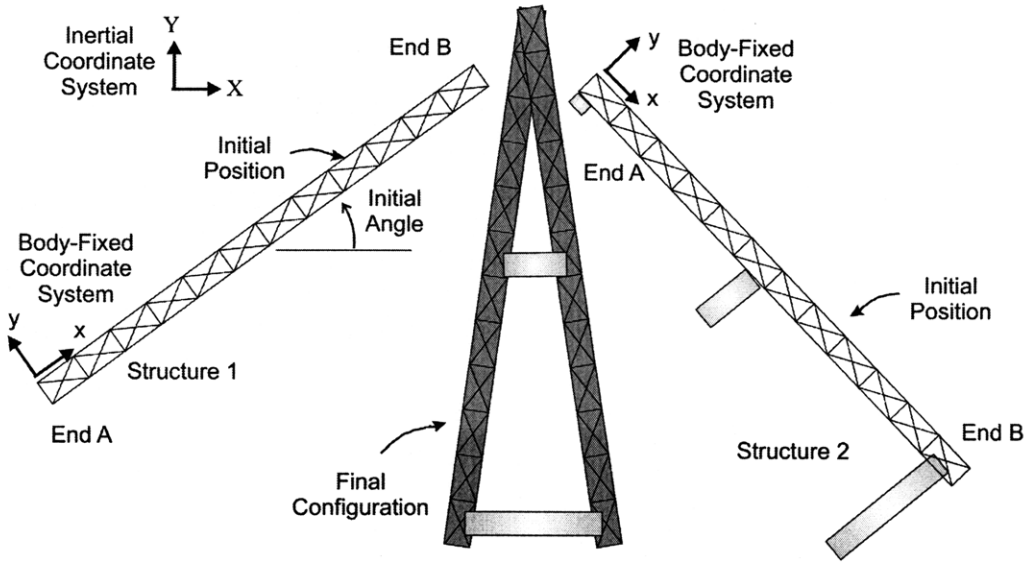

Figure 4.5. Initial and final positions for Case A.

Table 4.4 gives the rigid-body controller gain matrices $\mathbf{M}_f$ and $\mathbf{R}$ for the cost-function Equation (2.13). This controller is designed to minimize residual vibration but not vibration along the trajectory so the $\mathbf{Q}$ matrix is zero. Table 4.5 shows the gains for the flexible controller. The translational and rotation gains are equivalent for the rigid-body motion of the rigid-body and flexible controllers, but the flexible controller also includes gains for the modal variables.

Table 4.3. Assembly maneuver simulation parameters.

Parameters		Values
Structure 1	Initial position (xyz)	81.91, 50, 0 [m]
	Initial angle	35 [deg]
	Final position	158.28, 50, 0 [m]
	Final angle	82.5 [deg]
	Length	200 [m]
	Mass	600 [kg]
	Lowest frequencies	0.18, 0.51, 1.01, 1.85 [Hz]
Structure 2	Initial position (xyz)	250.15, 37.27, 0 [m]
	Initial angle	-44.5 [deg]
	Final position	184.38, 50, 0 [m]
	Final angle	-82.5 [deg]
	Length	200 [m]
	Total mass	650 [kg]
	Mass top piece	20 [kg]
	Mass middle cross bar	10 [kg]
	Mass bottom cross bar	20 [kg]
	Lowest frequencies	0.14, 0.42, 0.81, 1.58 [Hz]
Transportation time		30 [sec]
Number of flexible modes		4
Modal damping ratio		0.01

Table 4.4. Rigid-body controller cost matrix gains for assembly maneuver.

Parameters		Values
M_f	Translational position	4.0e+03 [$1/m^2$]
	Translational velocity	4.0e+04 [s^2/m^2]
	Angular position	4.0e+05 [$1/rad^2$]
	Angular velocity	4.0e+05 [$1/rad^2$]
R	Actuation effort	4.0e-06 [$1/N^2s$]

Table 4.5. Flexible controller cost matrix gains for assembly maneuver.

Parameters		Values
M_f	Translational position	4.0e+03 [$1/m^2$]
	Translational velocity	4.0e+04 [s^2/m^2]
	Angular position	4.0e+05 [$1/rad^2$]
	Angular velocity	4.0e+05 [$1/rad^2$]
	Modal position	4.0e+01
	Modal velocity	4.0e+01 [s^2]
R	Actuation effort	4.0e-06 [$1/N^2s$]

4.4.2 Simulation Case A – Space Telescope Truss Assembly Results

Figure 4.6 shows the angular position of both structures for the space telescope truss assembly (Case A). A rigid-body controller is used for this figure and applied to a rigid-body model and a flexible model. The figure shows that the gross trajectory is followed well by both models and demonstrates the basic quality of the rigid-body controller. At this scale no details of the vibration are apparent.

Figure 4.7 and Figure 4.8 show the magnitude of the gap between the structures at the top and bottom of the assembly, respectively. Figure 4.9 shows a closer view of the information in Figure 4.8. For the first 30 seconds the structures are moved together, then the assembly point is reached and the robots attempt to perform assembly. The black dotted line shows the rigid-body controller applied to a rigid-body model. It shows that the controller brings the latching points together within the tolerance almost immediately at the beginning of the assembly period. The gray dashed line shows the same rigid-body controller applied to a flexible model. The disruptive effects of the vibration cause the controller to take much longer (until 38 seconds) to bring the structures within the tolerance, and still the structures continue to ring after that point. While the rigid-body controller achieves its objectives for rigid-body models, the rigid-body controller applied to a flexible model induces substantial residual vibration. Clearly, vibration control is needed to perform this assembly task.

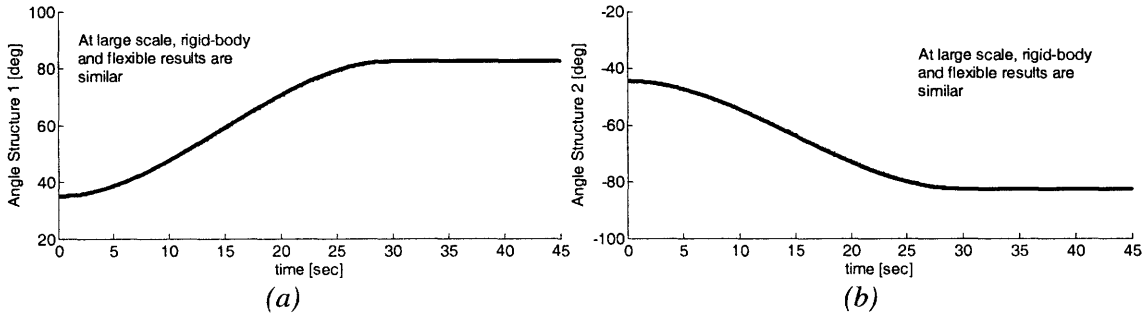

Figure 4.6. Rotational angles versus time with rigid-body controller for assembly maneuver simulation (Case A): (a) Structure 1; (b) Structure 2.

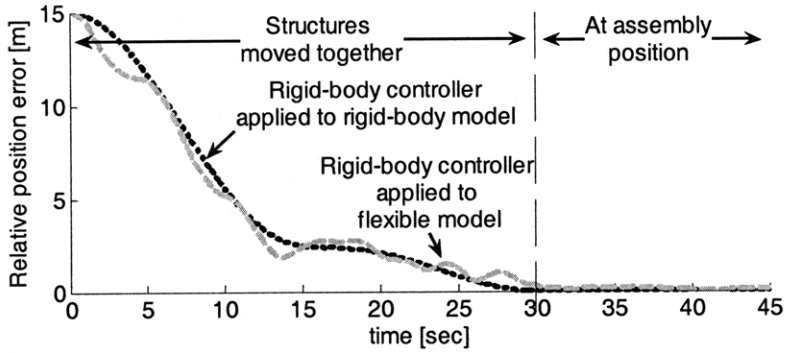

Figure 4.7. Magnitude of position error at top of assembly with rigid-body controller for assembly maneuver simulation (Case A).

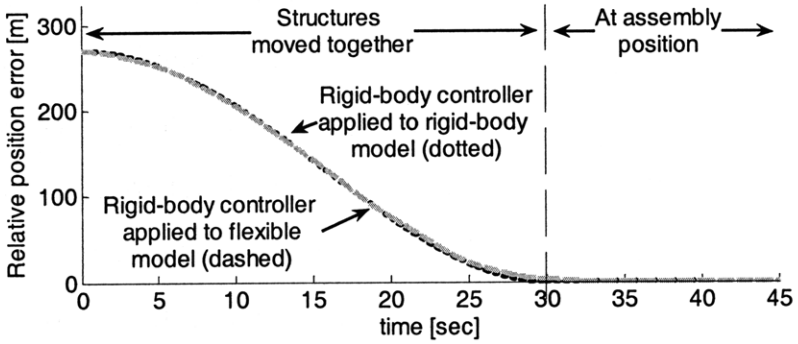

Figure 4.8. Magnitude of position error at bottom of assembly with rigid-body controller for assembly maneuver simulation (Case A). Detail of area close to latching tolerance is shown in Figure 4.9.

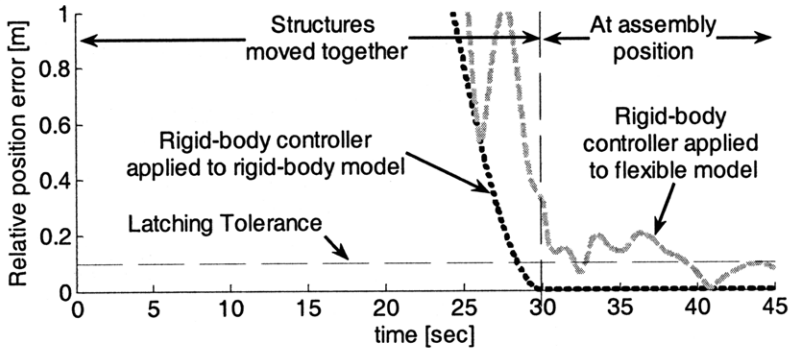

Figure 4.9. Detail of magnitude of position error at bottom of assembly with rigid-body controller for assembly maneuver simulation (Case A).

Next, the flexible controller applied to a flexible model is compared with rigid-body results. Figure 4.10 shows the position error at the top of the structure and

Figure 4.11 shows the same information magnified. Figure 4.12 and Figure 4.13 show the gap and the magnified gap at the bottom of the structures. The gray dashed line is again the rigid-body controller applied to a flexible model, while the solid black line shows the controller designed for a flexible model applied to a flexible model. The flexible controller's objective is to remove residual vibration and it does not try to minimize vibrations along the trajectory. The flexible controller reduces the gap to a small distance almost immediately at the desired assembly time, while rigid-body controller applied to flexible model does not reduce the gap to below 0.1 meters until 38 seconds have passed (8 seconds into assembly time).

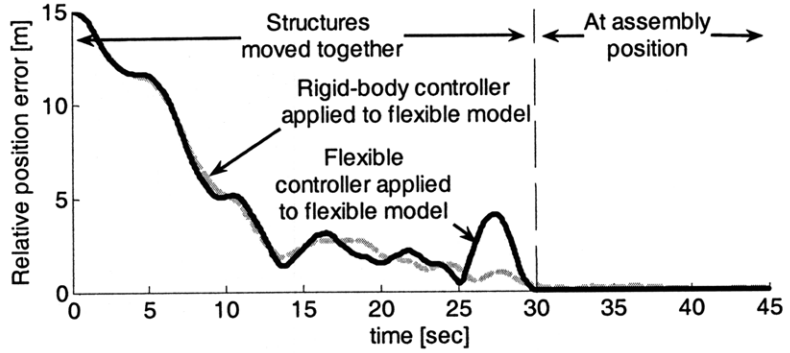

Figure 4.10. Magnitude of position error at top of assembly with flexible models for assembly maneuver simulation (Case A). Detail of area close to latching tolerance is shown in Figure 4.11.

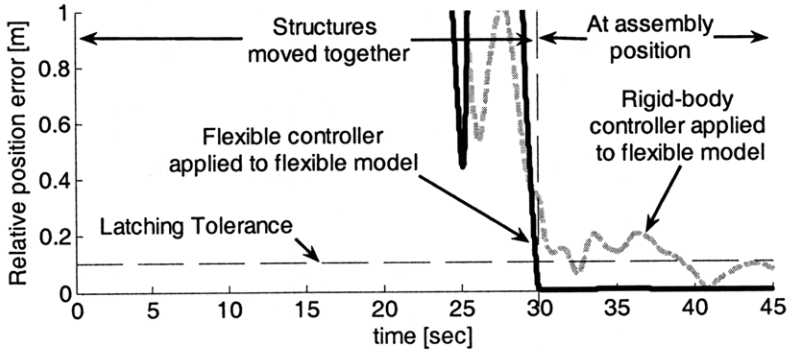

Figure 4.11. Detail of magnitude of position error at top of assembly with flexible models for assembly maneuver simulation (Case A).

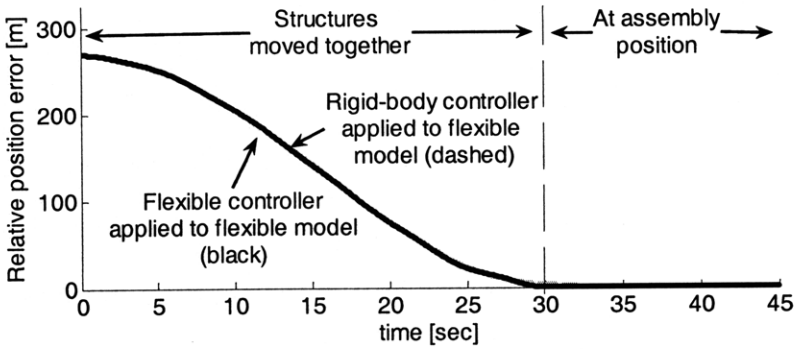

Figure 4.12. Magnitude of position error at bottom of assembly with flexible models for assembly maneuver simulation (Case A). Detail of area close to latching tolerance is shown in Figure 4.14.

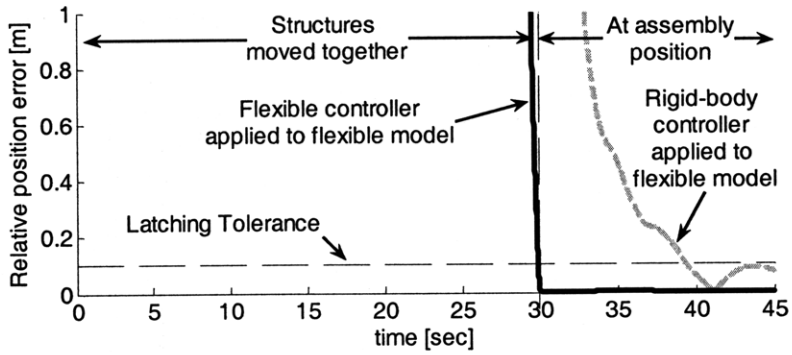

Figure 4.13. Detail of magnitude of position error at bottom of assembly with flexible models for assembly maneuver simulation (Case A).

Figure 4.14 shows the applied forces in the body-fixed x direction and Figure 4.15 shows the body-fixed y direction forces for the rigid-body and flexible controllers. The optimal control forces for the given trajectory are shown as dashed lines for the rigid-body. The optimal rigid-body controller is unable to complete the task at the assembly time of 30 seconds, so the PD controller removes the remaining residual vibrations. Most of the vibration is in the body-fixed y direction. The forces for the flexible controller (the solid line) take into account vibrations along the trajectory and hence oscillate about the rigid-body trajectory. Little control effort is needed after the assembly time. A higher performance controller such as optimal LQR regulator could be used instead of the PD controller at the end. Nonetheless, a second controller is required

to remove vibration for the rigid-body controller, while the optimal flexible controller essentially only needs station keeping after the desired assembly point.

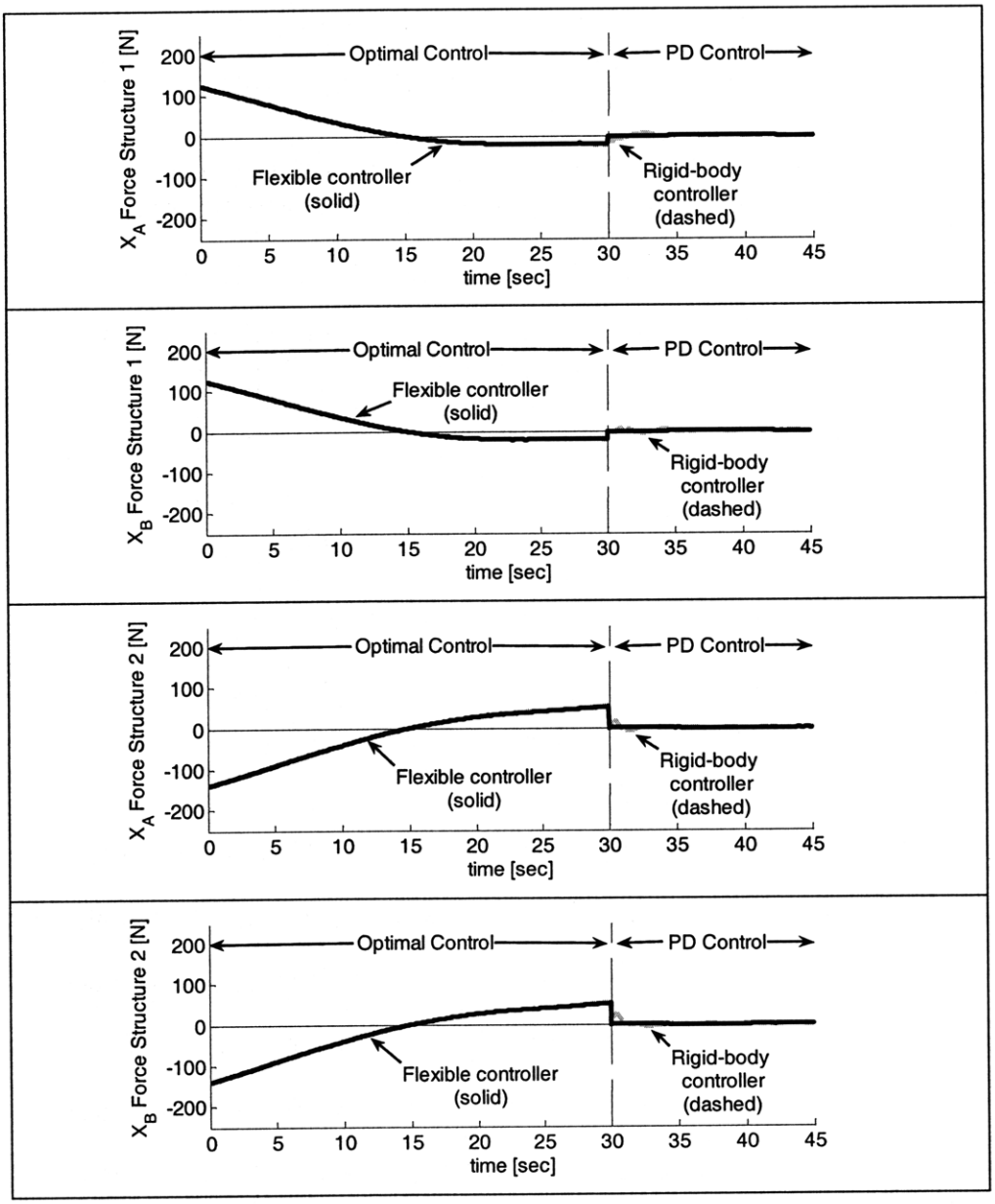

Figure 4.14. End forces in body-fixed x direction for rigid-body and flexible controllers with flexible plant model for assembly maneuver simulation (Case A).

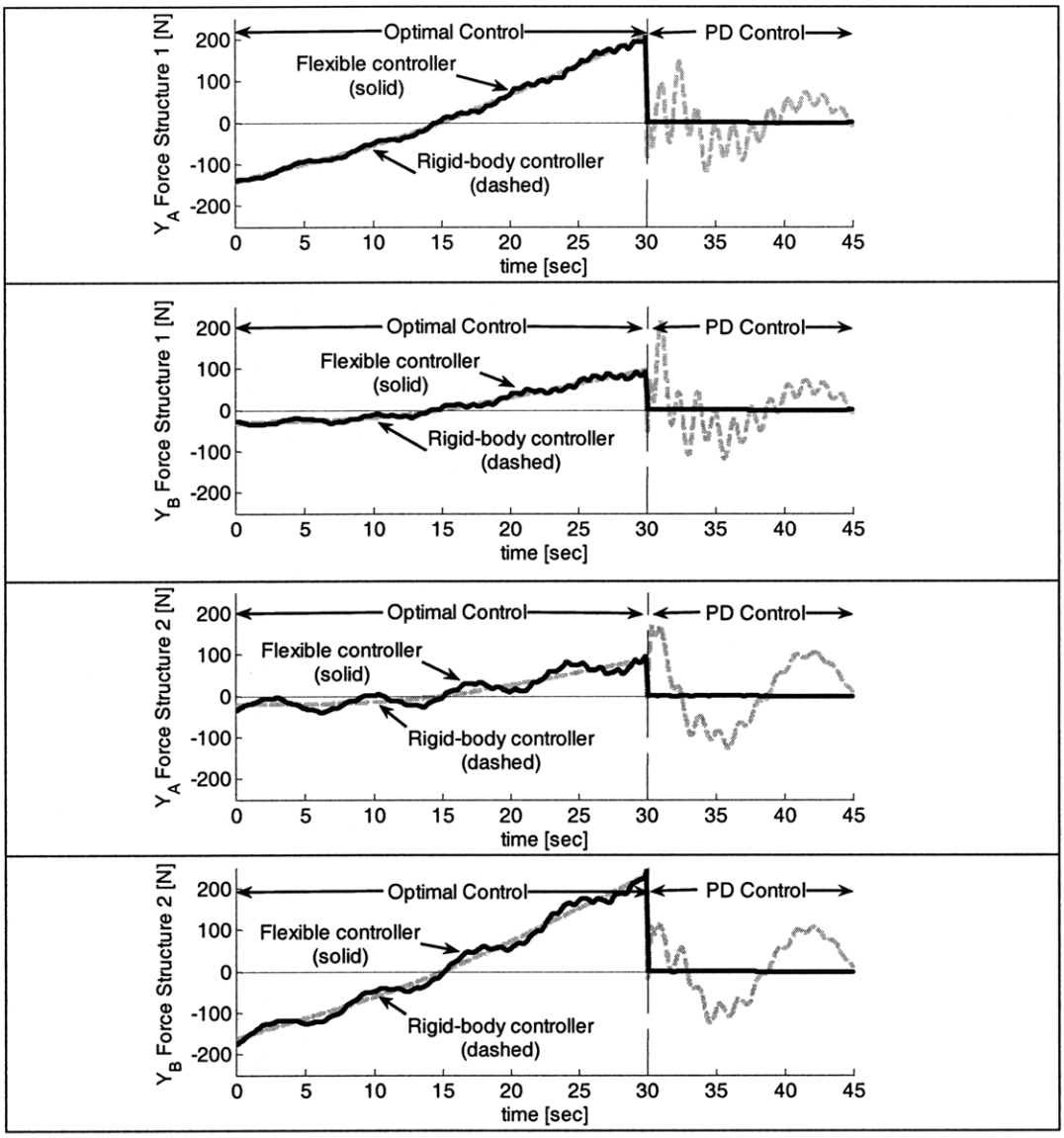

Figure 4.15. End forces in body-fixed y direction for rigid-body and flexible controllers with flexible plant model for assembly maneuver simulation (Case A).

Figure 4.16 and Figure 4.17 show the time integral forces (the net impulse) applied by robot 1 and robot 3. The forces applied by these robots are generated by their thrusters, so the net impulse is proportional to fuel use. Both controllers use similar amounts of fuel along the trajectory, but the rigid-body controller requires more fuel to complete the task.

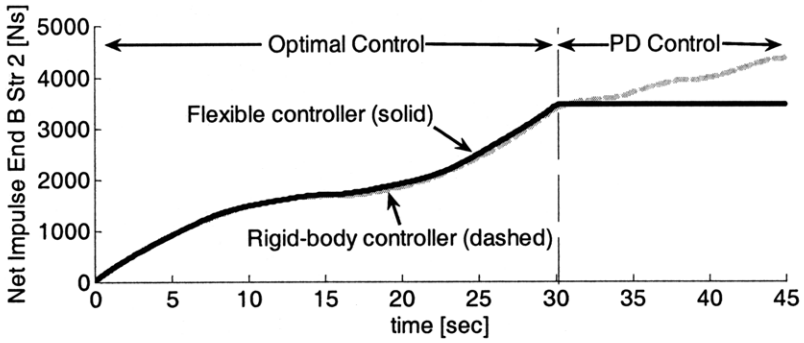

Figure 4.16. Net impulse applied by robot thrusters at end A (bottom) of structure 1 for rigid-body and flexible controllers with flexible plant model for assembly maneuver simulation (Case A). The net impulse is proportional to thruster fuel use.

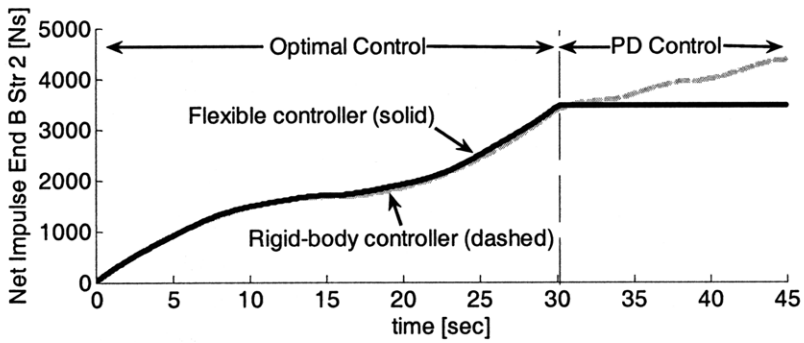

Figure 4.17. Net impulse applied by robot thrusters at end B (bottom) of structure 2 for rigid-body and flexible controllers with flexible plant model for assembly maneuver simulation (Case A).

4.4.3 Time-Varying System Results

For the optimal controllers used in the approach in this thesis, a time-varying linearized model of the system is created. However, the space systems undergo large translations and rotations, and linearizing the system about a single equilibrium point introduces significant errors. The approach taken in this thesis to solve this problem is to linearize about a time-varying trajectory. The flexible controller is used to demonstrate the benefit of using time-varying systems. The PD controller is not used in this case to emphasize the difference between the time-varying and time-invariant controllers.

For the system studied in the truss assembly (Case A), the structures rotate approximately 40 degrees. Figure 4.18 shows the position in the inertial Y direction at

the top end of the structure on the left. The dotted line is the linearized time-invariant system, and the solid line shows the linearized time-varying system. The desired final point is at about 145 meters. The time-invariant system accumulates significant error, while the time-varying system continually adjusts for the changes in angle and is able to follow the trajectory quite closely. Figure 4.19 shows the magnitude of the position error at the top of the structures. The time-invariant system accumulates such a large error that effective control is not possible. Figure 4.20 and Figure 4.21 show the forces applied to the structure at the same point as Figure 4.18. The time-varying approach in these results substantially improves performance.

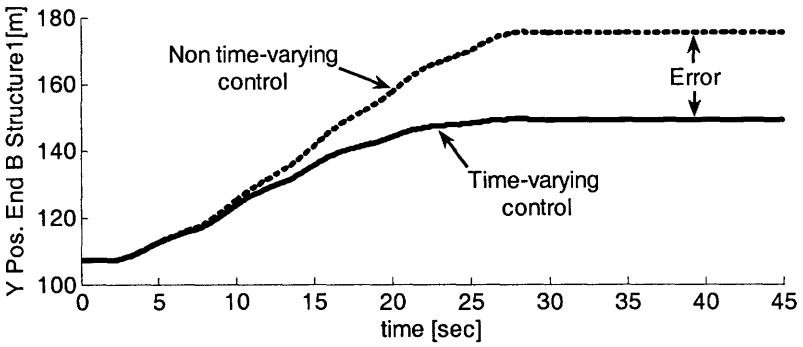

Figure 4.18. Inertial Y direction position of structure 1 at end B with flexible controller for assembly maneuver simulation (Case A).

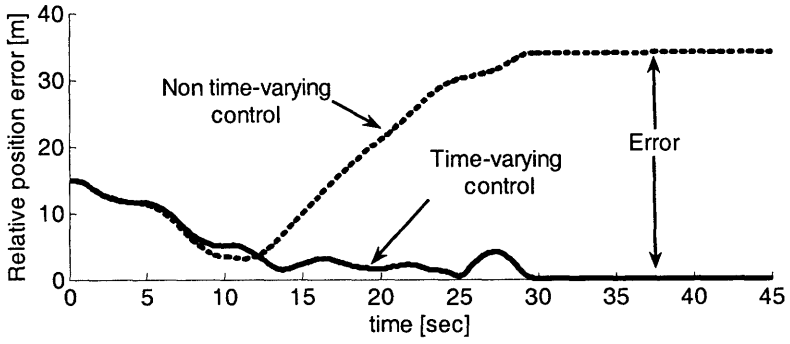

Figure 4.19. Magnitude of position error at top of assembly with flexible controller for assembly maneuver simulation (Case A).

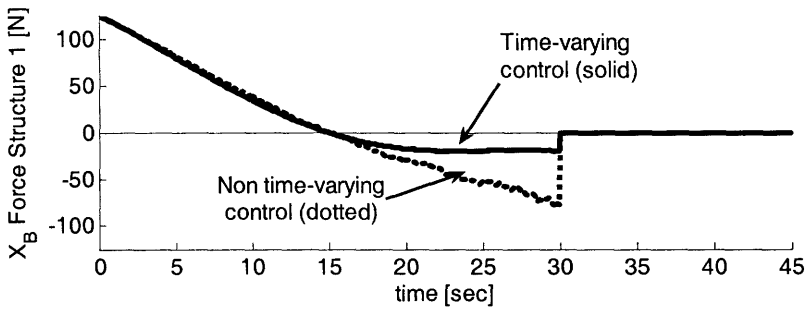

Figure 4.20. Body-fixed x direction applied forces at end B of structure 1 with flexible controller for assembly maneuver simulation (Case A).

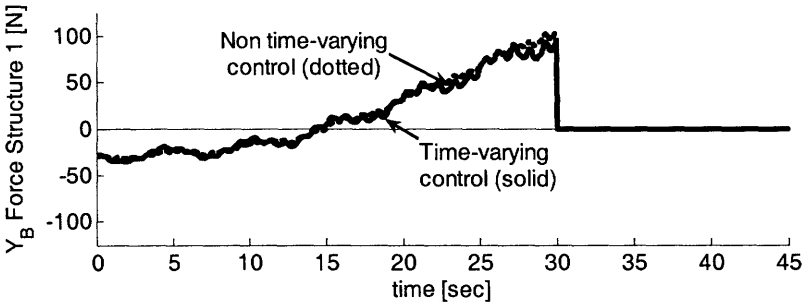

Figure 4.21. Body-fixed y direction forces at end B of structure 1 with flexible controller for assembly maneuver simulation (Case A).

4.4.4 Controller Bandwidth Results

A key requirement of the method proposed in this thesis is that the robot control systems have much higher frequency response than the dominant natural frequencies of the structures or higher frequencies of the optimal control forces and are therefore the robots are able to act as accurate force sources. Simulations are used to quantify this frequency separation. A first order low-pass filter models diminished bandwidth in the robot controller. The flexible controllers for Case A with varying bandwidths of ten, twenty and one thousand times the frequency of the highest mode to be controlled of the structure are compared. Figure 4.22 shows that the motions for all cases are similar in the large scale, and Figure 4.23 shows a closer view of the area within the latching tolerance. When the bandwidth is at least one thousand times the highest mode frequency, the controller performs well. At twenty times the highest mode frequency, the performance is

not quite as good but is still acceptable. When the bandwidth has dropped to ten times the highest mode frequency the controller has oscillations that cause it to initially exceed the latching tolerance.

Figure 4.24 shows the forces applied in the body-fixed y direction; these forces are magnified in Figure 4.25. The controller with bandwidth twenty times the highest mode frequency is not able to make the sharp transition at 30 seconds and lags the ideal controller, but is still able to achieve acceptable performance. However, the controller with bandwidth ten times the highest mode frequency does not track the desired force trajectory well. Based on these simulations, a bandwidth of somewhat less than twenty times the frequency to be controlled should be sufficient to allow the robots to act as force sources.

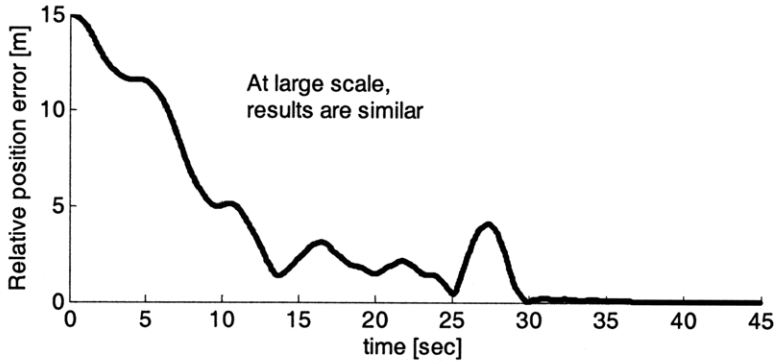

Figure 4.22. Magnitude of position error at top of assembly for flexible controllers with varying bandwidths for assembly maneuver simulation (Case A). Detail shown in Figure 4.26

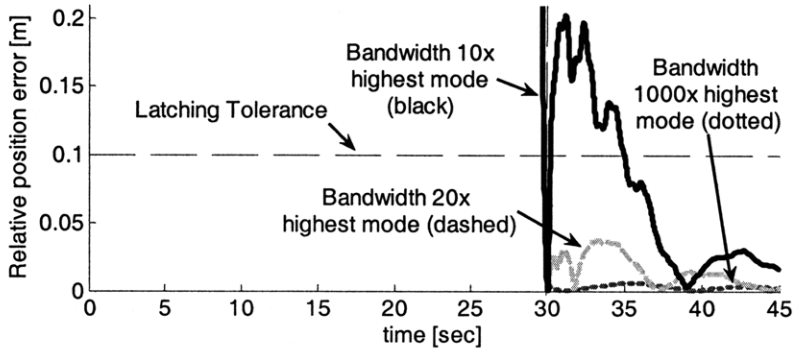

Figure 4.23. Detail of magnitude of position error at top of assembly for flexible controllers with varying bandwidths for assembly maneuver simulation (Case A).

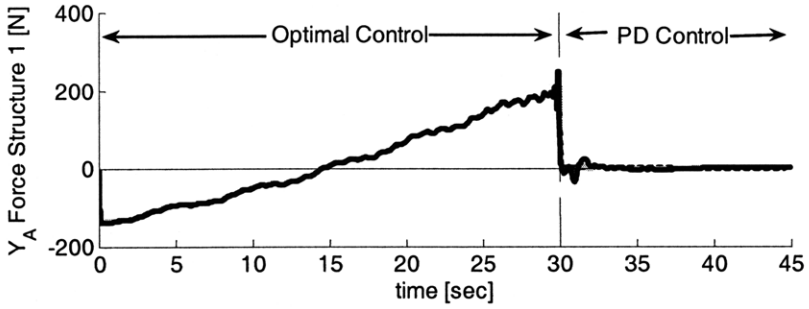

Figure 4.24. Body-fixed y direction force at end A of structure 1 for flexible controllers with varying bandwidth for Case A. Detail shown in Figure 4.25.

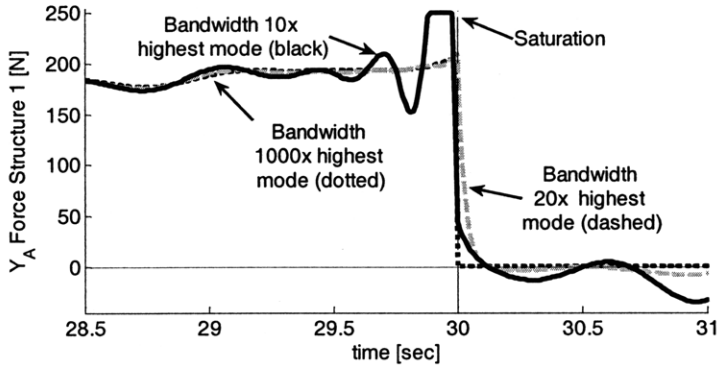

Figure 4.25. Detail of body-fixed y direction force at end A of structure 1 for flexible controllers with varying bandwidth for Case A.

4.4.5 Simulation Case B – Frame Assembly

Figure 4.26 shows three robots building a structural frame to become part of the telescope dish (Case B). These robots need to bring the endpoints of the flexible structures together without inducing large vibrations or causing collisions. The robots also need to perform this motion within a limited time.

Table 4.6 gives the parameters for this case. Note that the objective of bringing the endpoints of multiple structures together is more important than the absolute values of the final position parameters.

Table 4.7 and Table 4.8 give the cost function gains for the rigid-body and flexible controllers. Again for this case, the controller minimizes residual vibration but not vibration along the trajectory, so the $\mathbf{Q}$ matrix is zero.

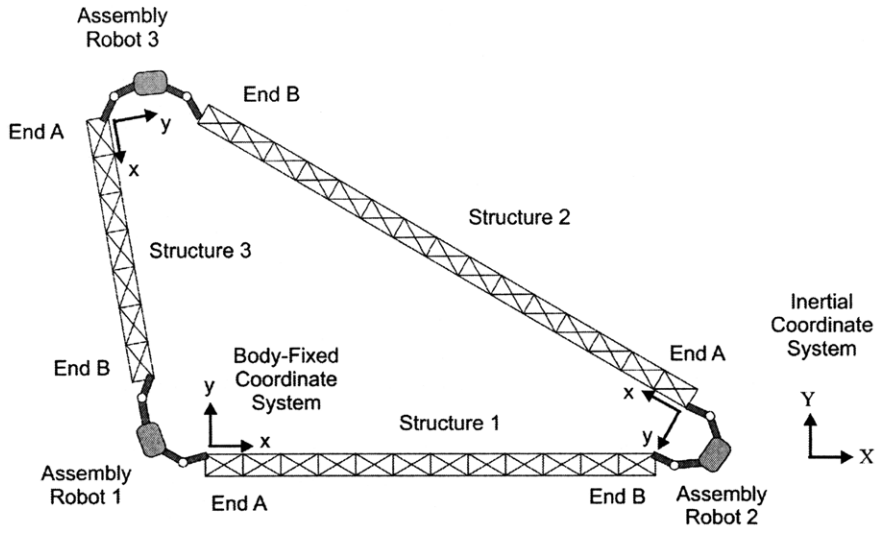

Figure 4.26. Flexible frame assembly simulation. Objects are not drawn to scale.

Table 4.6. Flexible frame assembly simulation parameters.

Parameters		**Values**
Structure 1	Initial position (xyz)	-3.55, -10.10, 0 [m]
	Initial angle	3 [deg]
	Final position	0, 0, 0 [m]
	Final angle	0 [deg]
	Length	150 [m]
	Mass	450 [kg]
	Lowest frequencies	0.33, .91,1.79,3.29 [Hz]
Structure 2	Initial position (xyz)	5.07, 65.24, 0 [m]
	Initial angle	139 [deg]
	Final position	0, 56.25, 0 [m]
	Final angle	143 [deg]
	Length	187.5 [m]
	Mass	562.5 [kg]
	Lowest frequencies	0.21, 0.59, 1.15, 2.10 [Hz]
Structure 3	Initial position (xyz)	-78.70, 54.73, 0 [m]
	Initial angle	263 [deg]
	Final position	-75, 56.25, 0 [m]
	Final angle	270 [deg]
	Length	112.5 [m]
	Mass	337.5 [kg]
	Lowest frequencies	0.58, 1.62, 3.19, 5.84 [Hz]
Assembly time		15 [sec]
Number of flexible modes		4
Modal damping ratio		0.01

Table 4.7. Rigid-body controller cost matrix gains for flexible frame assembly.

Parameters		Values
M_f	Translational position	4.0e+03 [1/m^2]
	Translational velocity	4.0e+04 [s^2/m^2]
	Angular position	4.0e+05 [1/rad^2]
	Angular velocity	4.0e+06 [s^2/rad^2]
R	Actuation effort	4.0e-06 [1/N^{2}s]

Table 4.8. Flexible controller cost matrix gains for flexible frame assembly.

Parameters		Values
M_f	Translational position	4.0e+03 [1/m^2]
	Translational velocity	4.0e+04 [s^2/m^2]
	Angular position	4.0e+05 [1/rad^2]
	Angular velocity	4.0e+06 [1/rad^2]
	Modal position	4.0e+01
	Modal velocity	4.0e+01 [s^2]
R	Actuation effort	4.0e-06 [1/N^{2}s]

4.4.6 Simulation Case B – Frame Assembly Results

This section gives the results for the flexible frame assembly simulation (Case B). Figure 4.27 shows the magnitude of the position error between structures 1 and 2. Figure 4.28 and Figure 4.29 show the position errors for the other gaps between structures. Figure 4.30, Figure 4.31, and Figure 4.32 show the same information magnified to show the detail inside the latching tolerance. For these figures, the gray dashed line is the rigid-body controller applied to the flexible model, and the solid black line is the flexible controller applied to the flexible model. The flexible structures are brought together over the first fifteen seconds. In all cases the flexible controller is able to remove the residual vibration by that point. Consequently, the settling time the flexible controller needs to keep the endpoints within the latching tolerance is substantially less than the additional eight seconds the rigid-body controller requires.

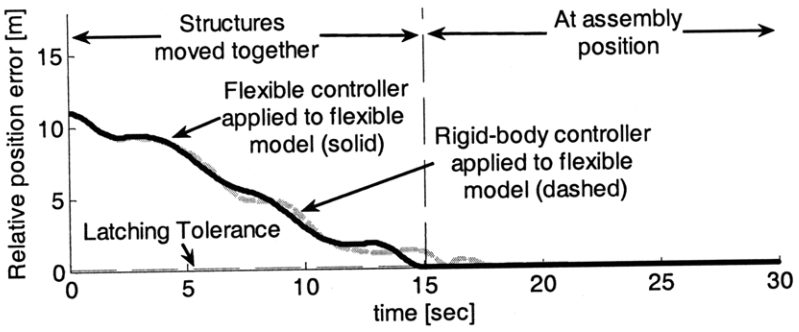

Figure 4.27. Magnitude of position error between structures 1 and 2 for flexible models for flexible frame assembly simulation (Case B).

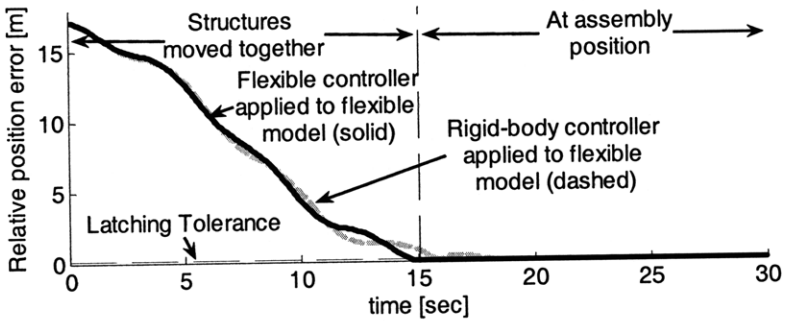

Figure 4.28. Magnitude of position error between structures 2 and 3 for flexible models for flexible frame assembly simulation (Case B).

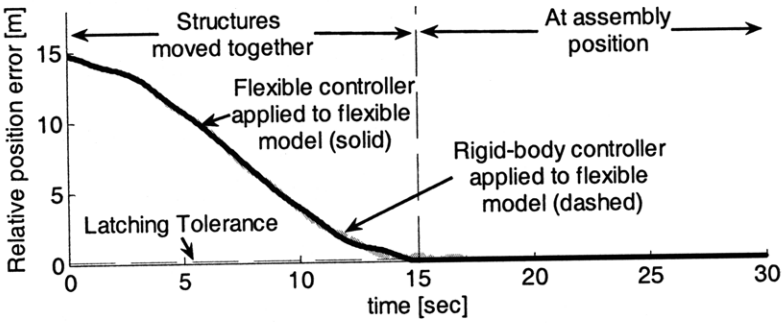

Figure 4.29. Magnitude of position error between structures 3 and 1 for flexible models for flexible frame assembly simulation (Case B).

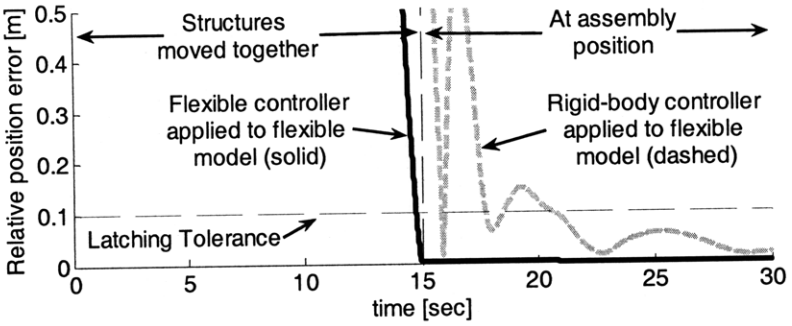

Figure 4.30. Detail of magnitude of position error between structures 1 and 2 for flexible models for flexible frame assembly simulation (Case B).

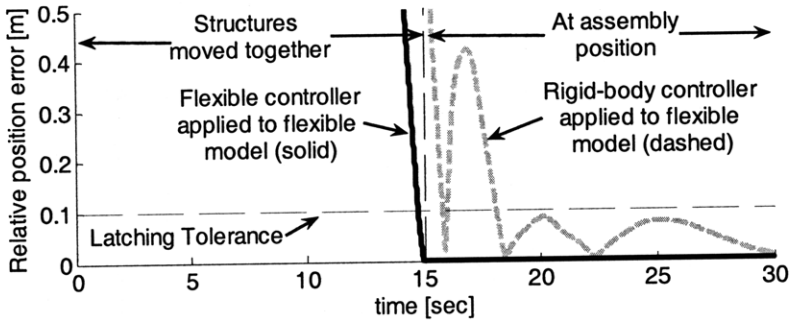

Figure 4.31. Detail of magnitude of position error between structures 2 and 3 for flexible models for flexible frame assembly simulation (Case B).

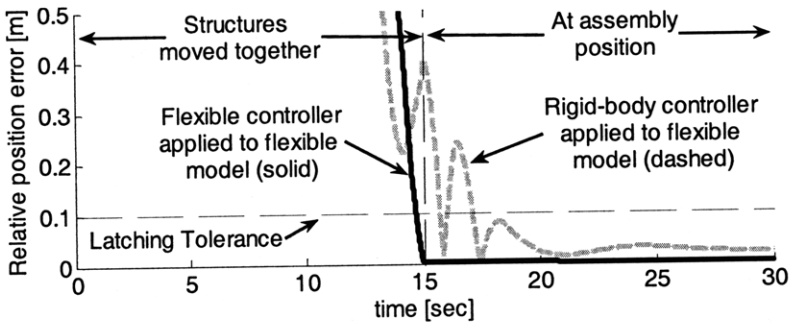

Figure 4.32. Detail of magnitude of position error between structures 3 and 1 for flexible models for flexible frame assembly simulation (Case B)

The forces at either end of the first structure are shown in Figure 4.33, Figure 4.34, Figure 4.35, and Figure 4.36. The structure is essentially rigid in the body-fixed x direction so there is little difference between controllers in Figure 4.33 and Figure 4.35. In the body-fixed y direction, the rigid-body controller must apply substantial forces to remove the residual vibration. Fuel use for both controllers is assumed to be equal (zero) because all forces are applied by manipulators with the thrusters turned off.

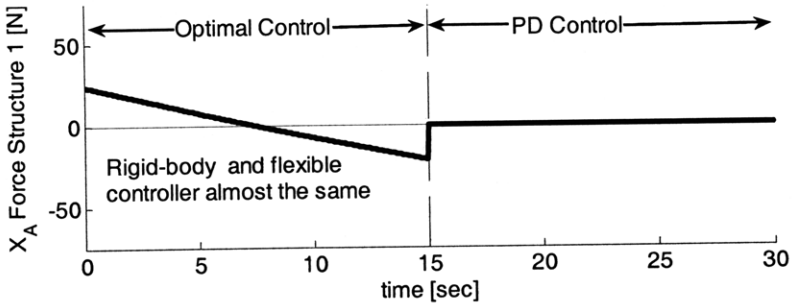

Figure 4.33. Forces in body-fixed x direction at end A of structure 1 for Case B.

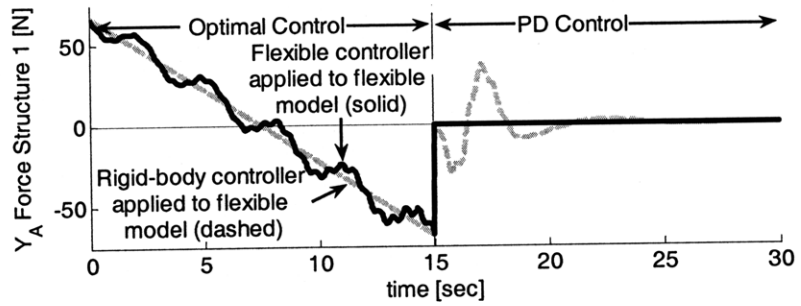

Figure 4.34. Forces in body-fixed y direction at end A of structure 1 for Case B.

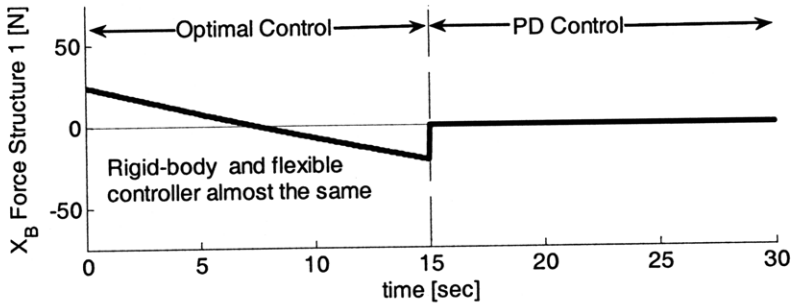

Figure 4.35. Forces in body-fixed x direction at end B of structure 1 for Case B.

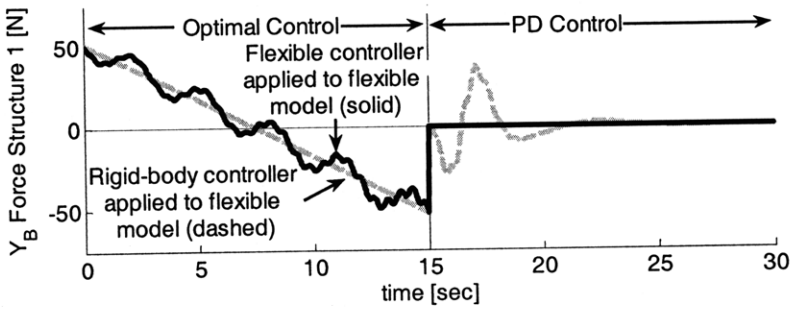

Figure 4.36. Forces in body-fixed y direction at end B of structure 1 for Case B.

4.4.7 Simulation Case C – Assembled Frame Transportation

For the third simulation (Case C), three robots transport the assembled frame to the space telescope (see Figure 4.37). Table 4.9 gives the parameters. For this case, the robots move and rotate the structure along a three-dimensional trajectory, as illustrated in Figure 4.38. Table 4.10 and Table 4.11 give the values for the controller gain matrices. The controller minimizes residual vibration but not vibration along the trajectory, so the **Q** matrix is zero.

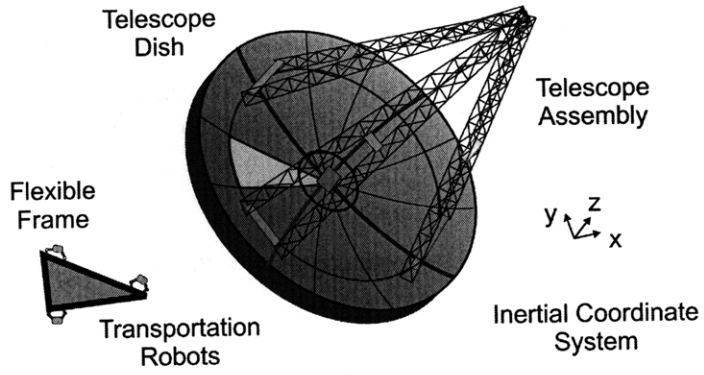

Figure 4.37. Simulation of transportation of flexible frame to the telescope.

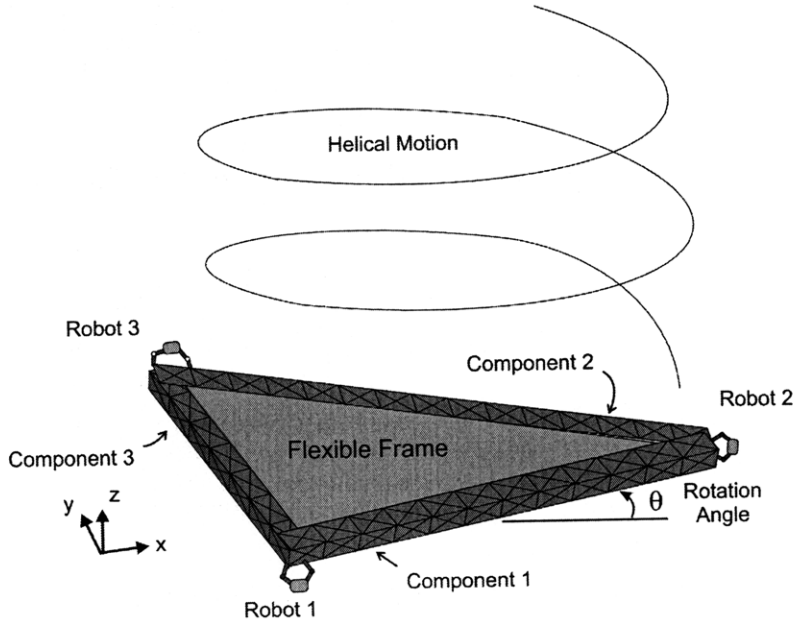

Figure 4.38. Structures from Case B assembled to form flexible frame Case C.

Table 4.9. Flexible frame transportation simulation parameters.

Parameters	Values
Initial position (center of mass)	-18.75, 37.5, 0 [m]
Initial angle	0 [deg]
Final position (center of mass)	-18.75, 37.5, 400 [m]
Final angle	540 [deg]
Total mass	1350 [kg]
Assembly time	60 [sec]
Number of flexible modes	10
Modal damping ratio	0.01
Lowest frequencies	0.18, 0.19, 0.25, 0.26, 0.45, 0.46, 0.54, 0.55, 0.80, 0.81 [Hz]

Table 4.10. Rigid-body controller cost matrix gains for flexible frame transportation.

Parameters		Values
M_f	Translational position	4.0e+04 [1/m^2]
	Translational velocity	4.0e+05 [s^2/m^2]
	Angular position	4.0e+05 [1/rad^2]
	Angular velocity	4.0e+06 [s^2/rad^2]
R	Actuation effort	4.0e-06 [1/N^{2}s]

Table 4.11. Flexible controller cost matrix gains for flexible frame transportation.

Parameters		Values
M_f	Translational position	4.0e+04 [1/m^2]
	Translational velocity	4.0e+05 [s^2/m^2]
	Angular position	4.0e+05 [1/rad^2]
	Angular velocity	4.0e+06 [1/rad^2]
	Modal position	4.0e+02
	Modal velocity	4.0e+03 [s^2]
R	Actuation effort	4.0e-06 [1/N^{2}s]

4.4.8 Simulation Case C – Assembled Frame Transportation Results

The flexible frame transportation simulation (Case C) demonstrates the performance of the controller on a three-dimensional system. The structure rotates 540 degrees about the z axis while translating 400 meters in a helical motion. Figure 4.39 shows the angular position of the structure for a rigid-body controller applied to the flexible model and the flexible controller applied to the same model. The large rotational

motions of the system are essentially the same. Figure 4.40 shows the angular error versus time. The rigid-body controller (gray dashed curve) has a larger error than the flexible controller (solid black curve), but it is still less than a degree at its largest.

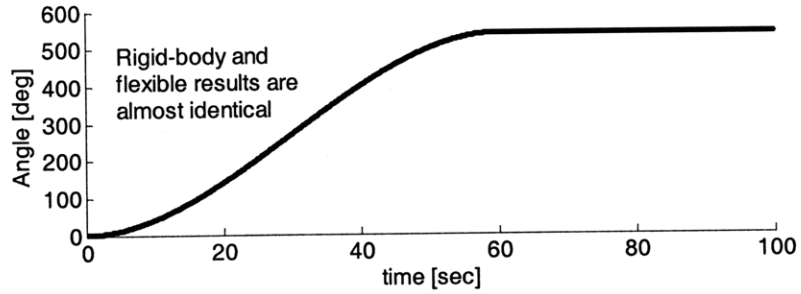

Figure 4.39. Angular position for frame transportation simulation (Case C).

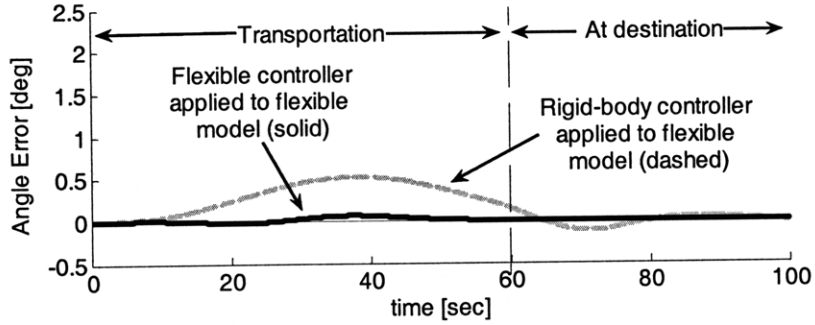

Figure 4.40. Angular position error for Case C.

Figure 4.41 shows the body-fixed z position of the structure at the corner held by robot 1 for both controllers. On a large scale, again the motions for both controllers look similar. However, if the position error is examined, the difference between the flexible and rigid-body controllers is apparent. Figure 4.42, Figure 4.43, and Figure 4.44 show the z position errors at the corners held by robots 1, 2, and 3 respectively. The rigid-body controller does not control the flexibility well, and the system vibrates. The flexible controller is designed to remove residual vibration, and while it permits flexing during transportation, the controller has removed almost all of the vibration when the structure reaches its destination at 60 seconds.

The body-fixed x and y direction forces at robot 1 are shown in Figure 4.45, Figure 4.46, while Figure 4.47 shows the net torque applied by all the robots to the structure. Figure 4.48 shows the forces in the body-fixed z direction. These figures are plotted in a coordinate frame attached to the structure, initially aligned with the inertial coordinate system. The system is not symmetric in geometry or mass distribution, so the x and y forces show the effort to rotate the structure while keeping the center of mass fixed in the inertial xy plane. Figure 4.47 demonstrates that the net force required to rotate the structure by all the robots is minimal along the angular trajectory given in Figure 4.39. The force plots also show that disturbances from system vibrations require a small amount of effort in the z direction after the destination is reach for the flexible controller, but almost none in the x and y directions. The rigid-body controller requires much more effort to remove the vibrations at the destination point, and thus the rigid-body controller requires more thruster fuel to apply the forces (see Figure 4.49). The first phase in Figure 4.49 shows the need for fuel to accelerate the structure. During transportation, little additional fuel is required. Then the robots use their thrusters to bring the structure to a stop. Finally, additional effort is required to remove any position errors and residual vibration.

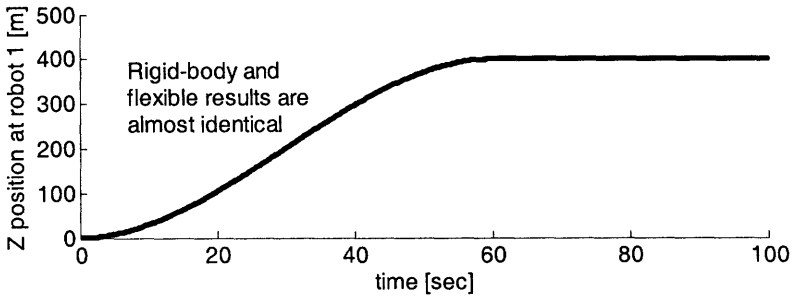

Figure 4.41. Robot 1 z position for frame transportation simulation (Case C).

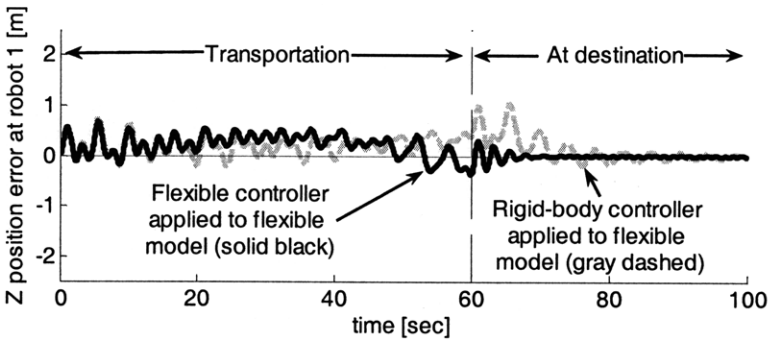

Figure 4.42. Robot 1 z position error, frame transportation simulation (Case C).

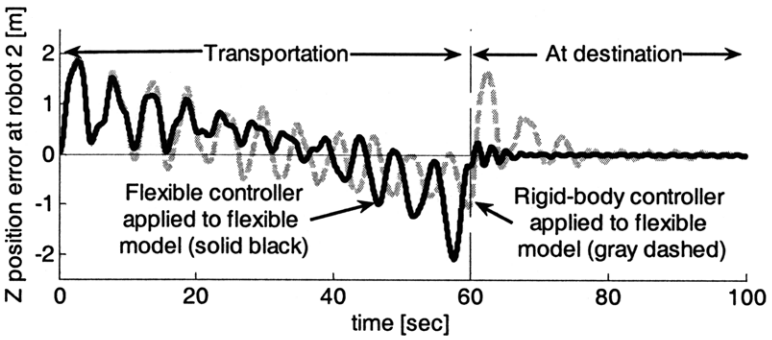

Figure 4.43. Robot 2 z position error, frame transportation simulation (Case C).

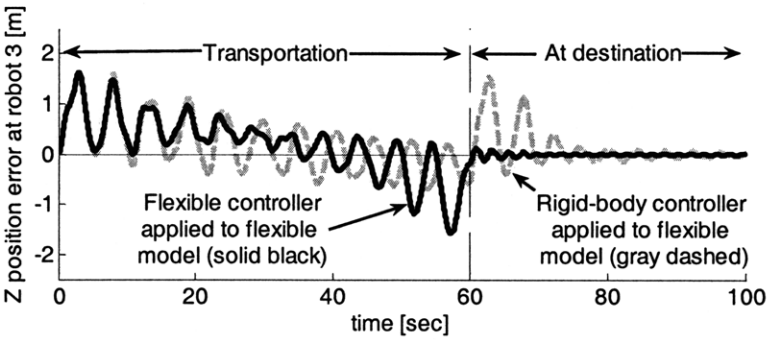

Figure 4.44. Robot 3 z position error, frame transportation simulation (Case C).

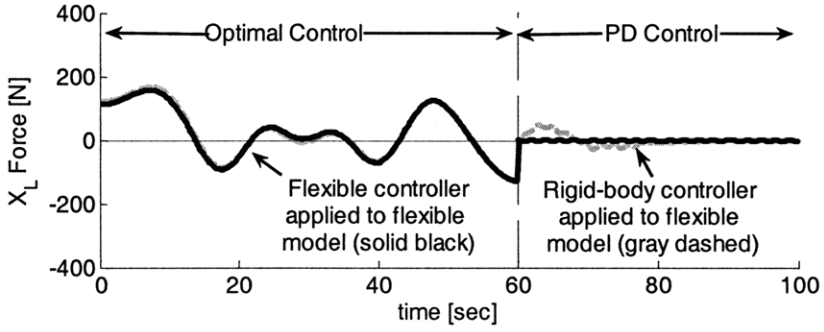

Figure 4.45. End forces in body-fixed x direction applied by robot 1 for frame transportation simulation (Case C).

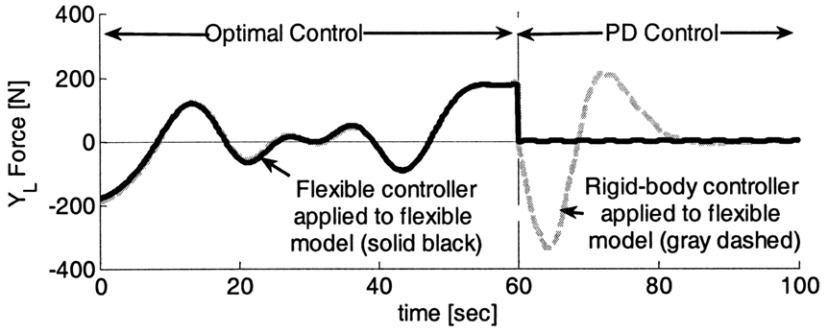

Figure 4.46. End forces in body-fixed y direction applied by robot 1 for frame transportation simulation (Case C).

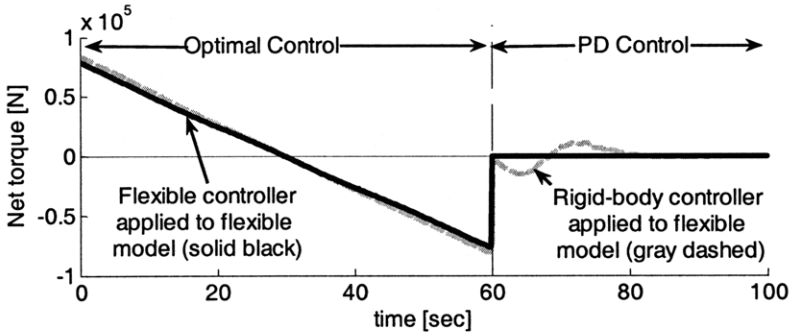

Figure 4.47. Net torque applied by all robots for Case C.

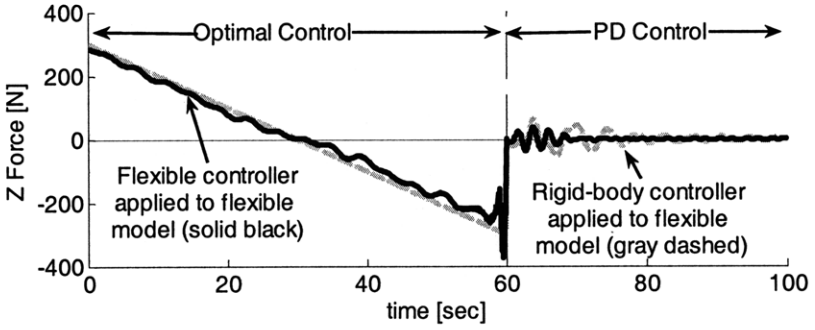

Figure 4.48. End forces in z direction applied by robot 1 for Case C.

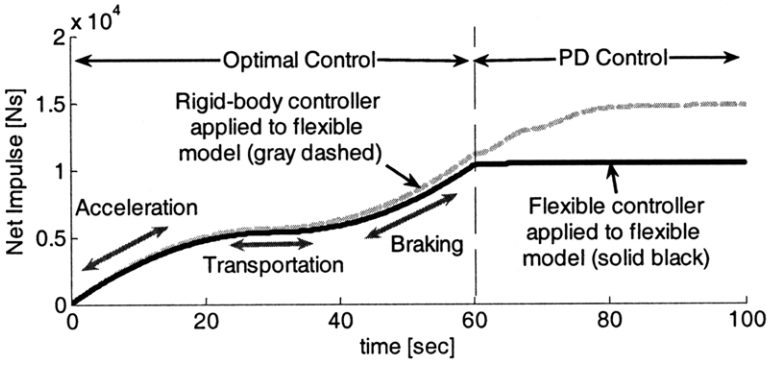

Figure 4.49. Net impulse applied by robot 1 for Case C.

4.5 Simulation Conclusions

The simulation results show the need for vibration control when manipulating large flexible structures on orbit. For assembly and transportation tasks, the straightforward choice of a controller designed without consideration of flexibility results in a controller unable to meet its objectives. The space structures are too large and too flexible to manipulate without accounting for flexibility. However, a controller designed for flexible control using the approach presented in this thesis is easily able to perform the desired operations while removing residual vibration. The method works for trajectory vibration minimization as well. The use of time-varying systems in the formulation allows the systems to undergo large translations and rotations while permitting the use of linear optimal control techniques. Simulations of the degrading effects of limited controller bandwidth show that a controller bandwidth about twenty times that of the highest modes to be controlled is sufficient to permit the separation of the robotic control from the space structure control.

CHAPTER

5

EXPERIMENTAL PROGRAM

This chapter presents experimental studies of the assembly of flexible structures by space robots. The purpose of the program is to verify and evaluate the performance for physical systems. Section 5.1 describes the experimental setup including the testbeds, the robots and the flexible structures. See Appendix C for additional details about the hardware and a discussion of the systems' limitations. Section 5.2 discusses the controllers used and Section 5.3 presents the cases studied. Section 5.4 gives the metrics used for comparison. The results here support the simulation result that separation of the robot controller bandwidth from the highest structural modal frequencies is needed for optimal control. The results are given in Section 5.5 and are summarized in Section 5.6.

5.1 Experimental Description

Experiments are performed using the MIT Field and Space Robotics Lab (FSRL) Free-Flying Robotics Testbed (FFRT) (see Figure 5.1) [3][4][7]. The testbed has been used for previous experiments, including the transportation of flexible linear elements using a decoupled controller developed by Yoshiyuki Ishijima [38][68][69]. That experiment showed that the Ishijima controller reduces fuel consumption over thruster based methods by controlling large motions with thrusters while damping vibrations with the manipulator arms.

Another view of the robots is shown in Figure 5.2. The testbed consists of a team of space robots floating on a 1.3 meter by 2.2 meter granite table with a polished surface [22][23][48][75]. The table is finely leveled to enable the gas bearing supported robots and structural elements to simulate working in a microgravity environment.

Each robot has a full set of reaction jet thrusters and fully instrumented manipulators including force/torque sensors mounted between each manipulator and the robot. The robots are self-contained with their own on-board electronics, computers and power supplies. The structural elements used in the experiments are relatively large and flexible. The motions of the robot/structural systems are measured by distributed accelerometers.

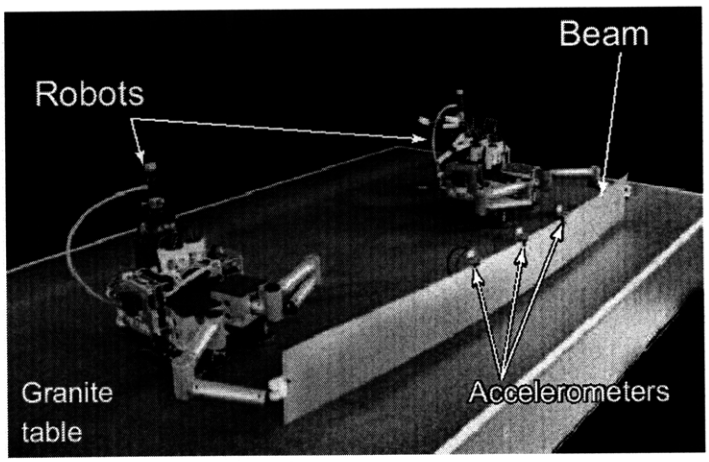

Figure 5.1. The MIT FSRL Free-Flying Robotics Test Bed (FFRT) [photo by Masahiro Ono].

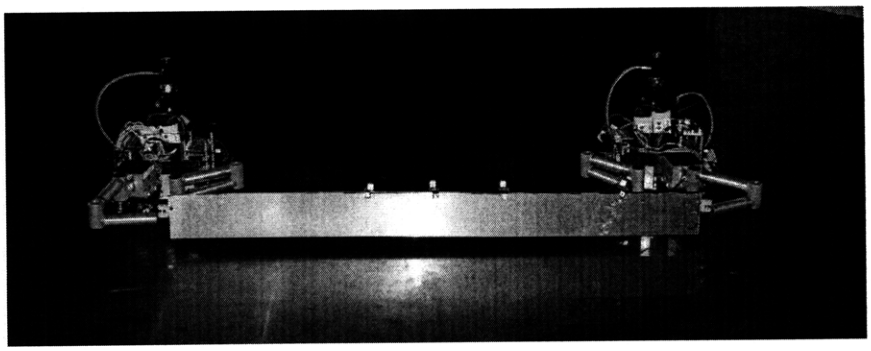

Figure 5.2. Experimental robots with flexible structure.

5.1.1 Experimental Robots

Each experimental space robot is equipped with two manipulators, eight thrusters, two position sensors, four manipulator joint angle encoders, and two force/torque sensors (see Figure 5.3 and Figure 5.4). The robots have seven DOF in total (two DOF translation, one DOF rotation, and four DOF for the manipulator joints), all of which are controllable and observable. The robots can operate in free-flying mode (thrusters on) or free-floating mode (thrusters off). The robots are designed to emulate the dynamics of robots on orbit. The spacecraft base is light weight in relation to the manipulators and to the loads they carry. Motion of the manipulators significantly perturbs the motions of the base as is found in orbital robots. The robots are completely self-contained thus eliminating the need for tethers that could affect the dynamics of the system.

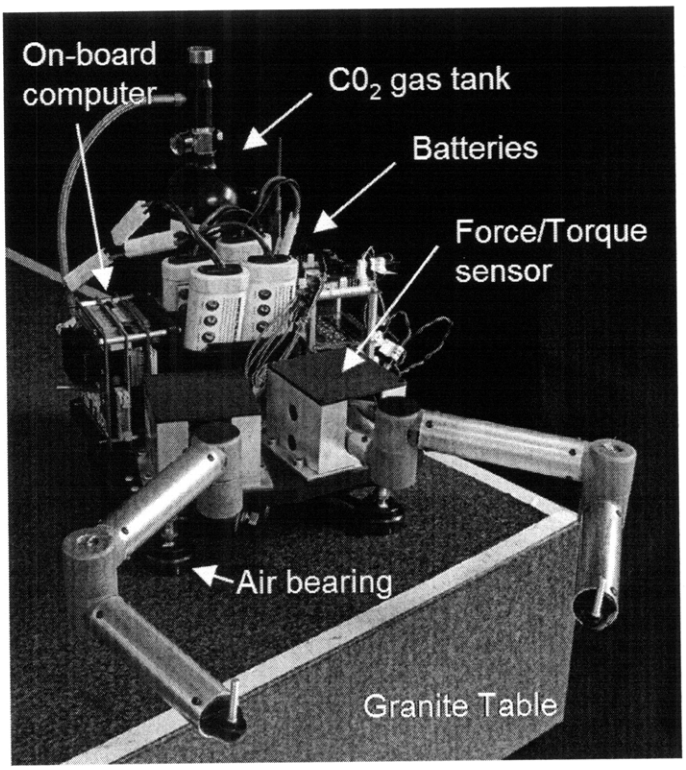

Figure 5.3. Experimental space robot [with Masahiro Ono].

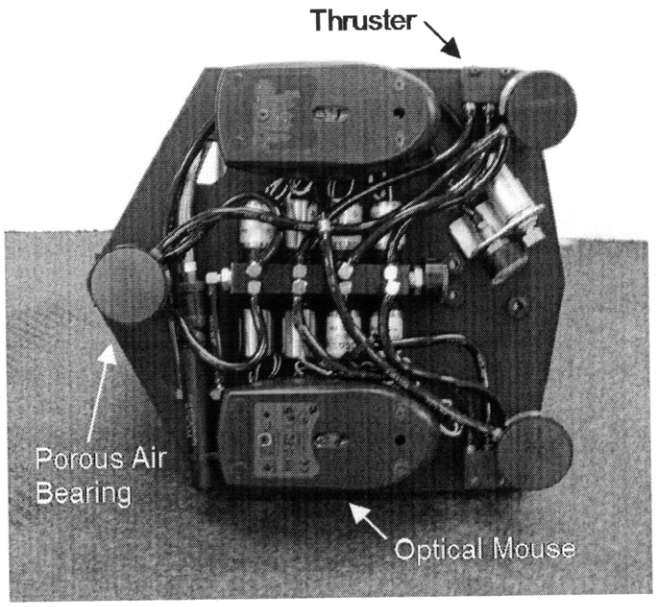

Figure 5.4. Underside of experimental space robot.

The robot electronics consist of an on-board PC104 computer, wireless LAN, a CAN peripheral board, the CANBus (twisted pair wires), and the interface electronic circuit boards. The software for the simulations and the experimental system is written with Matlab xPC and Simulink.

Figure 5.5 shows a schematic diagram of an experimental robot. The figure shows the local and inertial coordinate systems. The local coordinate system for each robot has its x axis aligned with the robot's axis of symmetry. Joint 0 is the location of the force/torque sensor. Joint 0 and Link 0 are fixed to the base; Joint 1 is the first movable joint. Note that the center of mass of the spacecraft base is not on the axis of symmetry due to electronics and battery placement.

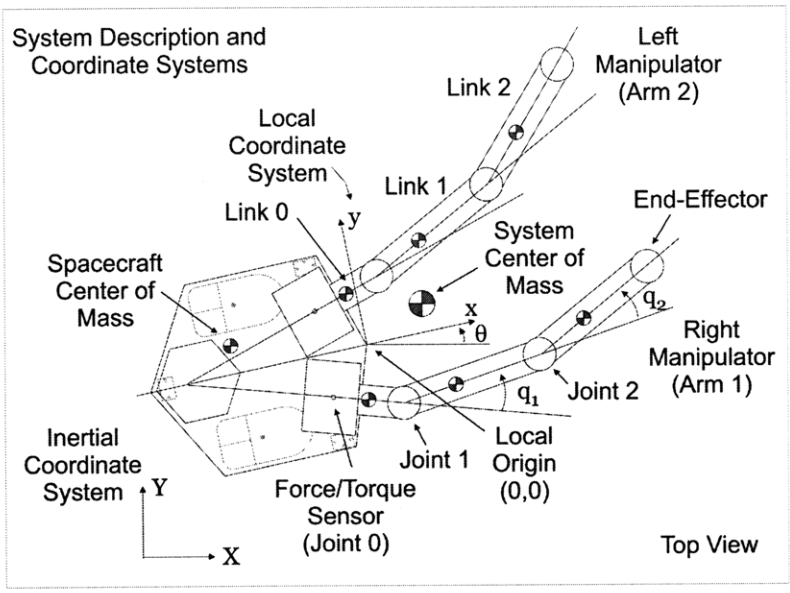

Figure 5.5. System description for experimental robot.

5.1.2 Flexible Elements

Experimental flexible elements are representative of flexible orbital structural modules. The experimental flexible elements are desired to have similar low natural frequencies and low damping ratios (like the orbital modules) to evaluate the flexible assembly control algorithms [34]. The experimental system's vibration amplitudes are relatively large to make the differences between algorithms visible. However, designing a flexible element that meets all these requirements is challenging, and compromises must be made (see Appendix C for details).

For the experiments presented here, the flexible element used is a simple aluminum beam, 1.22 meters long and 0.80 mm thick, shown in Figure 5.1. The beam's lowest natural frequency is 2.8 Hertz and has a damping ratio of 0.15. The beam is supported by and pin-jointed to the end-effectors of the robots' manipulators. Accelerometers mounted on the beam measure its vibration and provide the vibration states needed by the flexible algorithms (see Figure 5.1).

5.2 Experimental Control

For the fine-assembly maneuvers, two control methods for maneuvering the flexible structures are compared. In the *No Vibration Control* method, the robots use their manipulators to maneuver the structures using a proportional and derivative controller (PD) without consideration of flexibility in the system. The thrusters are not used for this controller. In the *Vibration Control* method, the robots use their manipulators to maneuver the structures and also use the manipulators to control vibrations. The thrusters are not used.

The assembly controller used for the experiments is shown in Figure 5.6. Due to limitations on the robots' force/torque sensors and due to robot actuation challenges such as limited control bandwidth, the experimental robot force controller is unable to follow the force trajectory called for by the ideal approach shown in the controller block diagram in Figure 2.2. Simulations in Section 4.4.4 showed that controller bandwidth twenty times the frequency of the highest mode of the structure to be controlled is sufficient. However, due to robot communication system delays and design constraints on the flexible structure, this separation is not achieved for this hardware. The limitations of the experimental system are discussed in more detail in Appendix C.

For the experiments, a practical approach is taken in the face of the challenges of limited sensing and actuation, and the vibration controller used for the experiments follows a reduced version of the generalized framework. This approach resembles the controller used for flexible element transportation cases using a vibration controller and a compliance controller [68][69]. However, unlike the transportation case, for assembly the robots use their manipulators both to apply forces to the structures to move them and to reduce structural vibration. Also, the thrusters were used for rigid-body motions during transportation. As seen in Figure 5.6, the flexible structure controller determines the forces to apply in reaction to the vibration of the flexible structures.

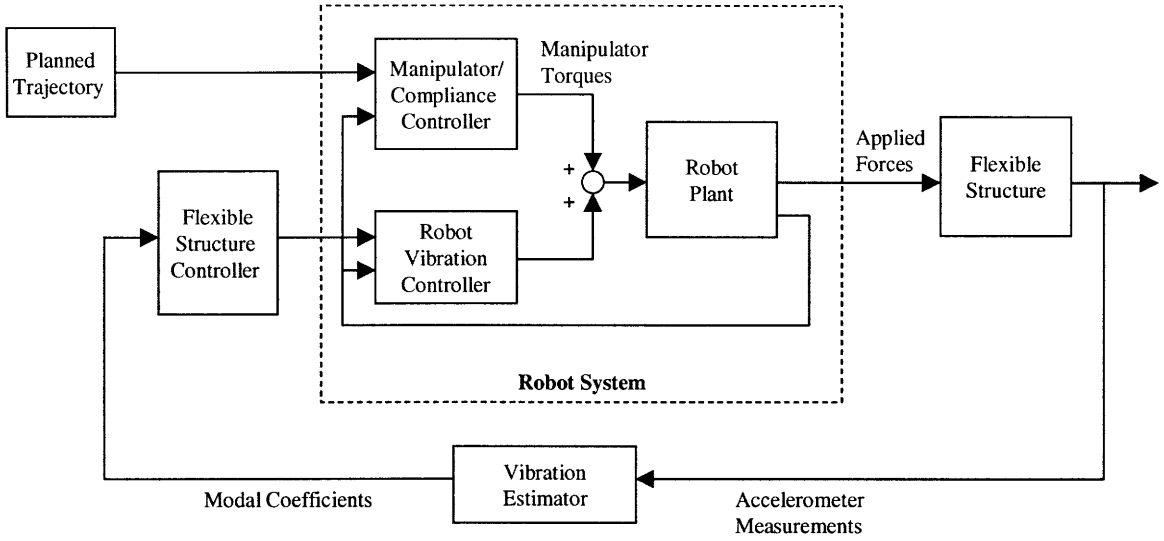

Figure 5.6. Experimental assembly controller.

The vibration is controlled with an LQR state feedback controller:

$$\begin{bmatrix} \mathbf{F}_A \\ \mathbf{F}_B \end{bmatrix} = \mathbf{K}_{lqr} \begin{bmatrix} \hat{\mathbf{q}}_m \\ \dot{\hat{\mathbf{q}}}_m \\ \hat{\mathbf{F}}_A \\ \hat{\mathbf{F}}_B \end{bmatrix} \tag{5.1}$$

where $\mathbf{F}_A$ and $\mathbf{F}_B$ are the components of the forces applied to the structural element in the direction of bending and $\hat{\mathbf{F}}_A$ and $\hat{\mathbf{F}}_B$ are the measured manipulator forces and contain measurement error and noise. A Kalman filter obtains $\hat{\mathbf{q}}_m$ and $\dot{\hat{\mathbf{q}}}_m$, the estimated modal coordinates [11]. Only the first mode of vibration is controlled in this experiment due to the limitations of the controller bandwidth and because the first mode is dominant for the experimental structures. The optimal LQR gain $\mathbf{K}_{lqr}$ is found by solving the infinite horizon Riccati equation (unlike the general solution, the time-varying matrix Equations (2.19) and (2.20) do not need to be integrated for this controller) [10]. Note also that the LQR controller state does not contain the rigid body modes of the structure, so the vibration controller does not control the rigid body motion of the structural elements.

The rigid body motions of the structures are controlled by the manipulator compliance controller. The robots are commanded to bring the manipulators together. The manipulator compliance controller also makes the experimental system more robust to assembly errors and noise. The manipulator compliance controller is a simple PD controller for the manipulator's end effector.

5.3 Experiments

For parallel assembly, two robots support the ends of two flexible elements as illustrated in Figure 5.7. The objective is to bring both sets of endpoints of the flexible structures together in a fine-assembly maneuver, close enough to allow the pieces to be attached. On orbit it is expected that an automatic latching system would fasten the flexible elements together once they are in close proximity. The figure shows the initial configuration and the location of the inertial coordinate system.

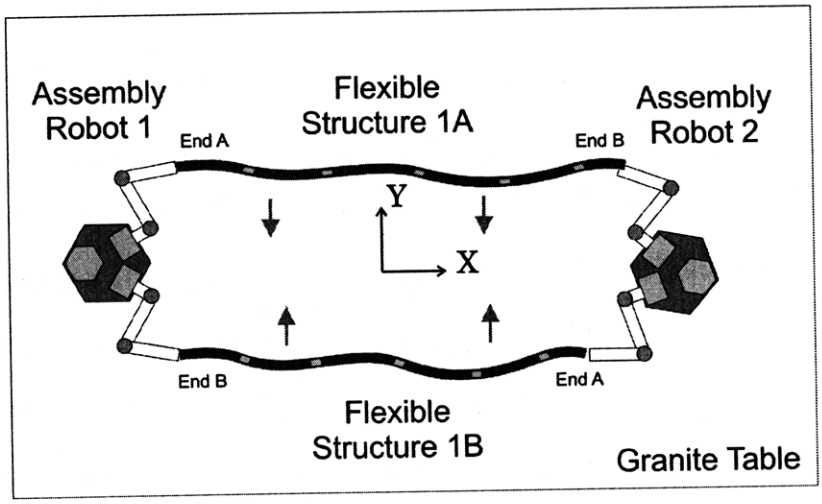

Figure 5.7. Parallel assembly maneuver.

The robots must maneuver the two flexible elements so that they do not collide with each other as they flex. Also, the robots must not permit any end-effector to collide

with a flexible structure or another end-effector. The robots do not undergo large translations so they do not use their thrusters. When turned on to maintain nominal attitude control, the thrusters were found to contribute to the damping of the system, but were also found to use significant fuel. Since conservation of limited propellant is an objective of the method the thrusters were turned off for the assembly experiments. Figure 5.8 shows a photograph of the experiment.

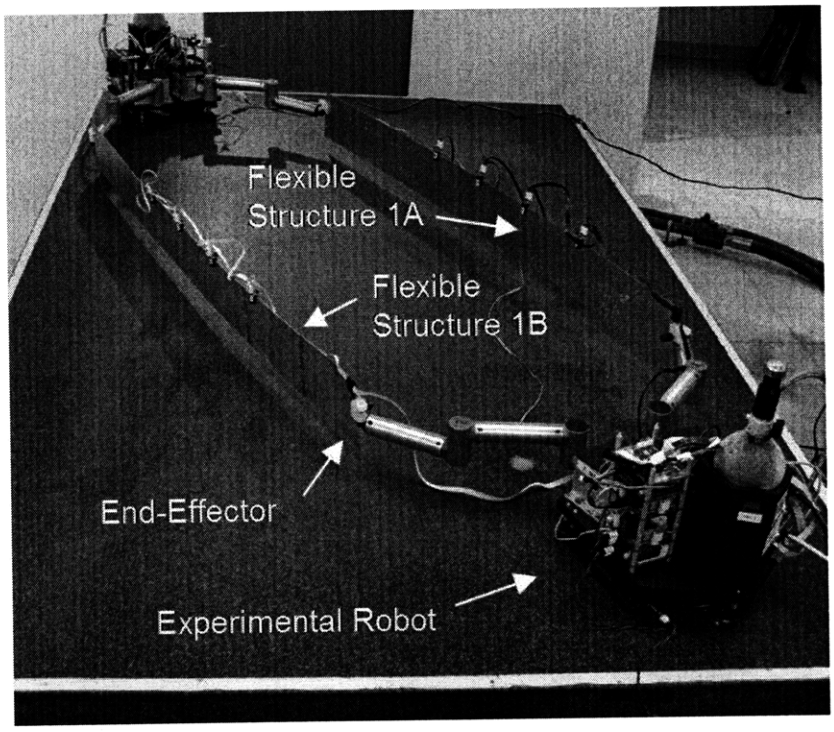

Figure 5.8. Photograph of parallel assembly maneuver.

5.4 Experimental Performance Metrics

The performance of the experimental control methods are compared using metrics measuring the ability of the controller to remove vibration, and whether the controller is able to perform its required task. Three criteria are considered: damping ration, settling time, and success in assembly latching.

The damping ratio, which captures the ability of the controller to eliminate vibration, is determined from the first mode of vibration of the flexible structure. The time-series vibration amplitude data is obtained from the Kalman filter. The damping ratio zeta ζ is determined assuming the system is a second order oscillatory system with an exponential envelope of the form:

$$x(t) = X \exp(-\zeta \omega_n t) \sin(\sqrt{1-\zeta^2}\,\omega_n t + \phi) \tag{5.2}$$

In this equation t is time, x is the vibration amplitude, X is the amplitude constant, ω_n is the natural frequency of vibration and ϕ is the phase angle. Using the logarithmic decrement method, the damping ratio is found from the natural log of the ratio of the first peak x_1 to the nth peak x_n:

$$\zeta = \frac{1}{2\pi n} \ln(x_1 / x_n) \tag{5.3}$$

The second criterion is the settling time, t_s, that measures the ability of the controller to remove vibrations. The settling time is the time that it takes transients to decay so the amplitude of vibration is always below a given threshold. The experimental data is noisy so the settling time uses a five percent criteria, $t_s(5\%) = 3/\zeta\omega_n$.

Finally, the third criterion is success in latching the assembly. For assembly cases, even if the controller uses little fuel and removes vibration quickly, it is not successful unless it is able to perform the assembly operation. For the experimental system, the latching mechanism is simply a pair of magnets (see Figure 5.9 and Figure 5.10). If the controller brings the assemblies close together in the correct orientation, the magnets snap together and latching takes place. To perform the assembly latching, the flexible structures must be close at the latching point and have the correct orientation. When the orientation is correct, the distance d_x is zero. As latching takes place, the distance d_y goes to zero. If

the orientation is not correct it is possible for the magnets to be close together and not latched (see Figure 5.11).

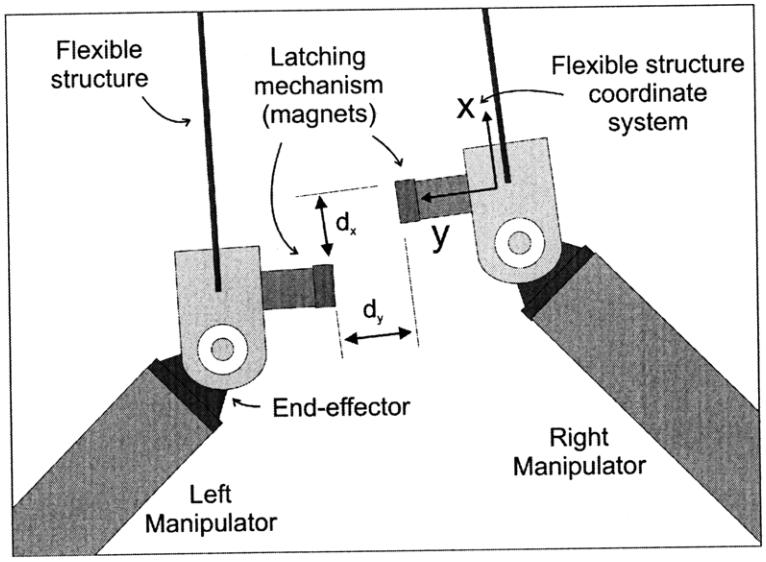

Figure 5.9. Diagram of latching mechanism.

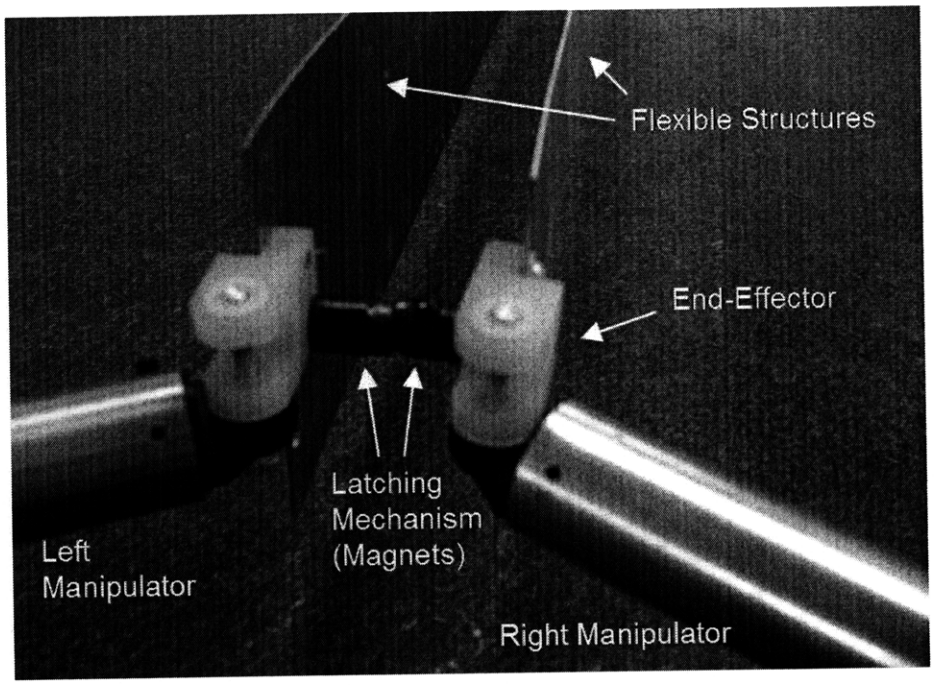

Figure 5.10. Photograph of latching mechanism.

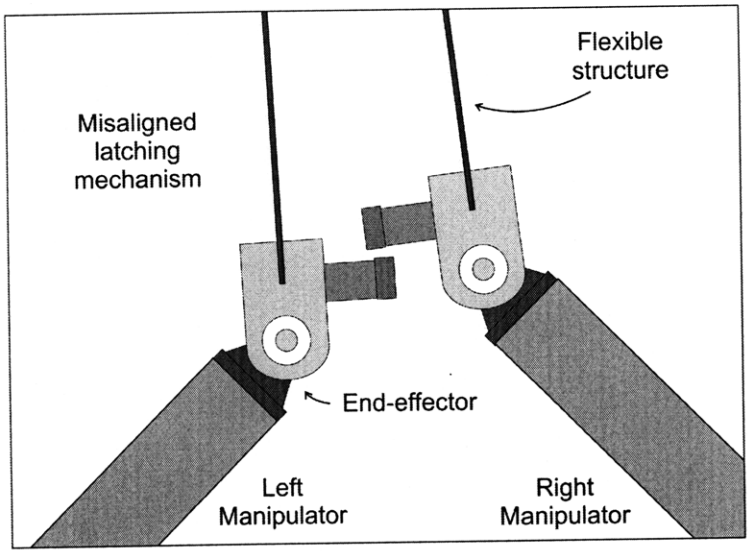

Figure 5.11. Mismatched latching configuration.

5.5 Experimental Results

The difference in latching ability can be seen clearly in Figure 5.12 and Figure 5.13. Figure 5.12 shows the relative x position (defined in Figure 5.9) for a typical assembly experiment for the controller without vibration control, and Figure 5.13 shows the vibration controller result for the same case as Figure 5.18. For assembly cases, the motion of the assembly operation excites enough vibrations to demonstrate the difference in controllers, so the systems start at rest. For the first three seconds, the structures are moved together. Then the structures are at the assembly point and the robots attempt to latch the assembly pieces together. Both controllers bring the endpoints close together, but the orientation is misaligned for the case without vibration control and the assembly latching does not take place. The vibration controller is able to bring the latching magnets within the one centimeter x distance needed to allow the latching to take place at approximately four seconds into the maneuver. Figure 5.14 and Figure 5.16 show the y component for both controllers and Figure 5.15 and Figure 5.17 show the same information magnified. Note that the latching tolerance in the y direction is allowed to be larger than in the x direction.

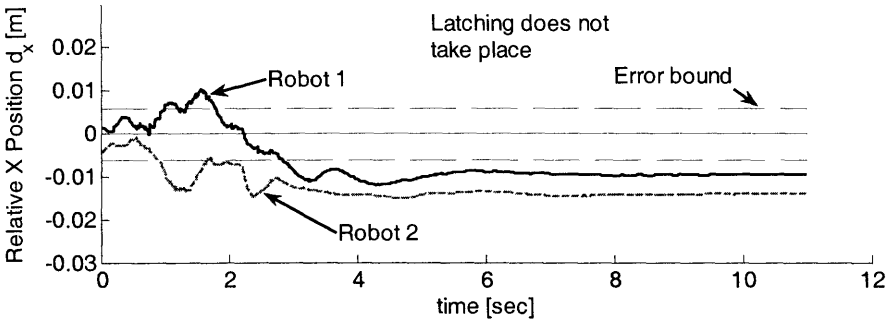

Figure 5.12. Relative x position at the latching point without vibration control for the assembly experiment. Latching does not take place for this case.

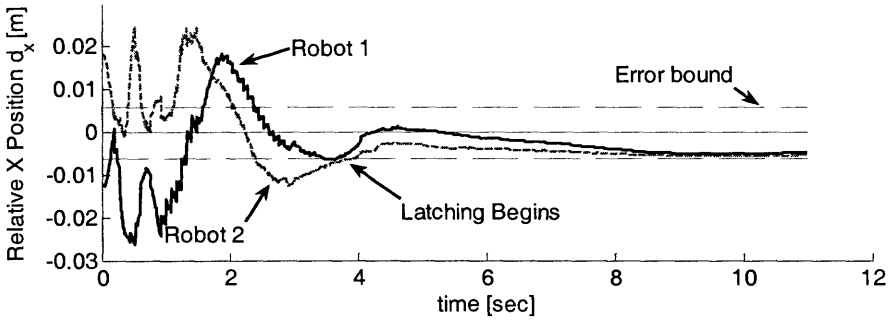

Figure 5.13. Relative x position at the latching point with vibration control for the assembly experiment.

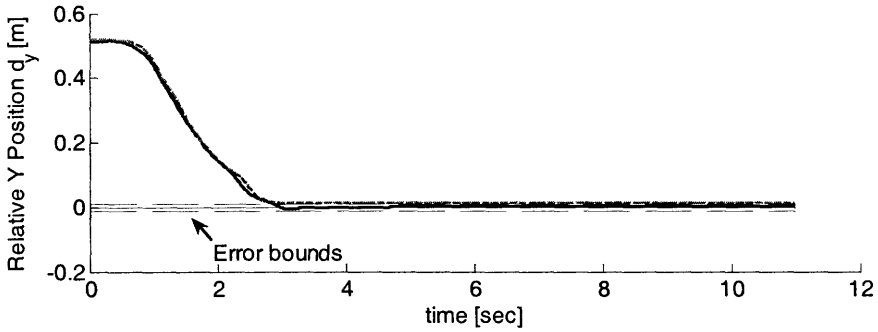

Figure 5.14. Relative y position at the latching point without vibration control for the assembly experiment. Latching does not take place for this case. See Figure 5.15 for details.

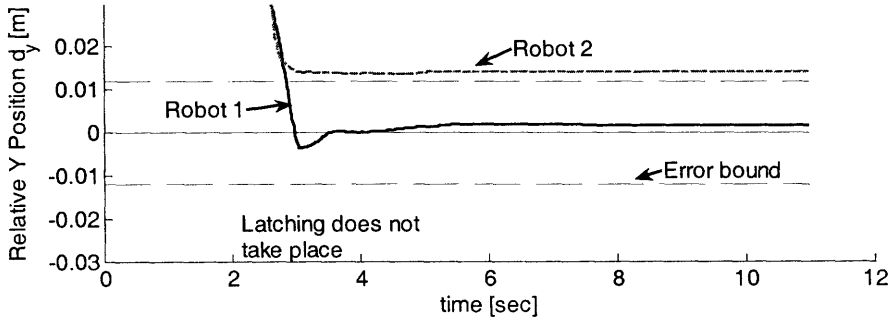

Figure 5.15. Detail of relative y position at the latching point without vibration control for the assembly experiment.

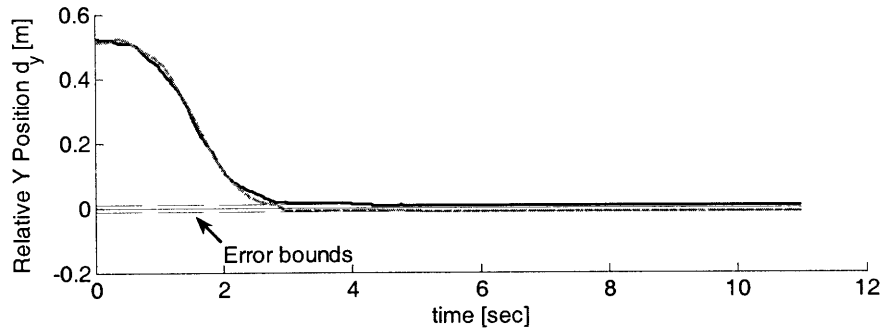

Figure 5.16. Relative y position at the latching point with vibration control for the assembly experiment. Latching begins at about four seconds. See Figure 5.17 for details.

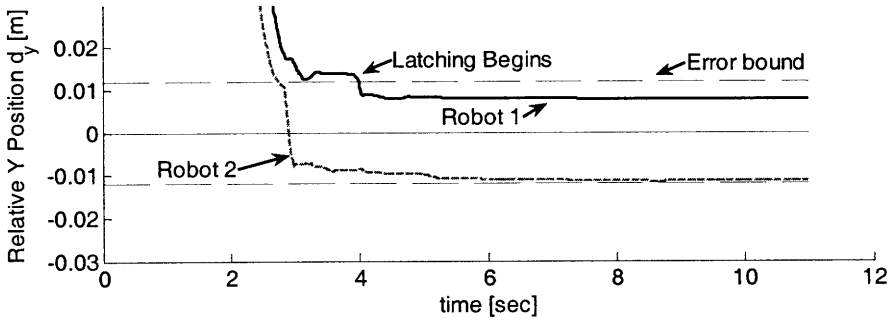

Figure 5.17. Detail of relative y position at the latching point with vibration control for the assembly experiment.

Figure 5.18 shows the first mode of vibration. The first row shows the results without vibration control and the second row shows the vibration controller. The columns show the results for structures 1A and 1B (see Figure 5.7 for the experimental setup). Figure 5.18 shows a typical case where the controller without vibration control is not able to control the vibrations well enough to allow the assemblies to latch while the vibration controller does achieve its objectives.

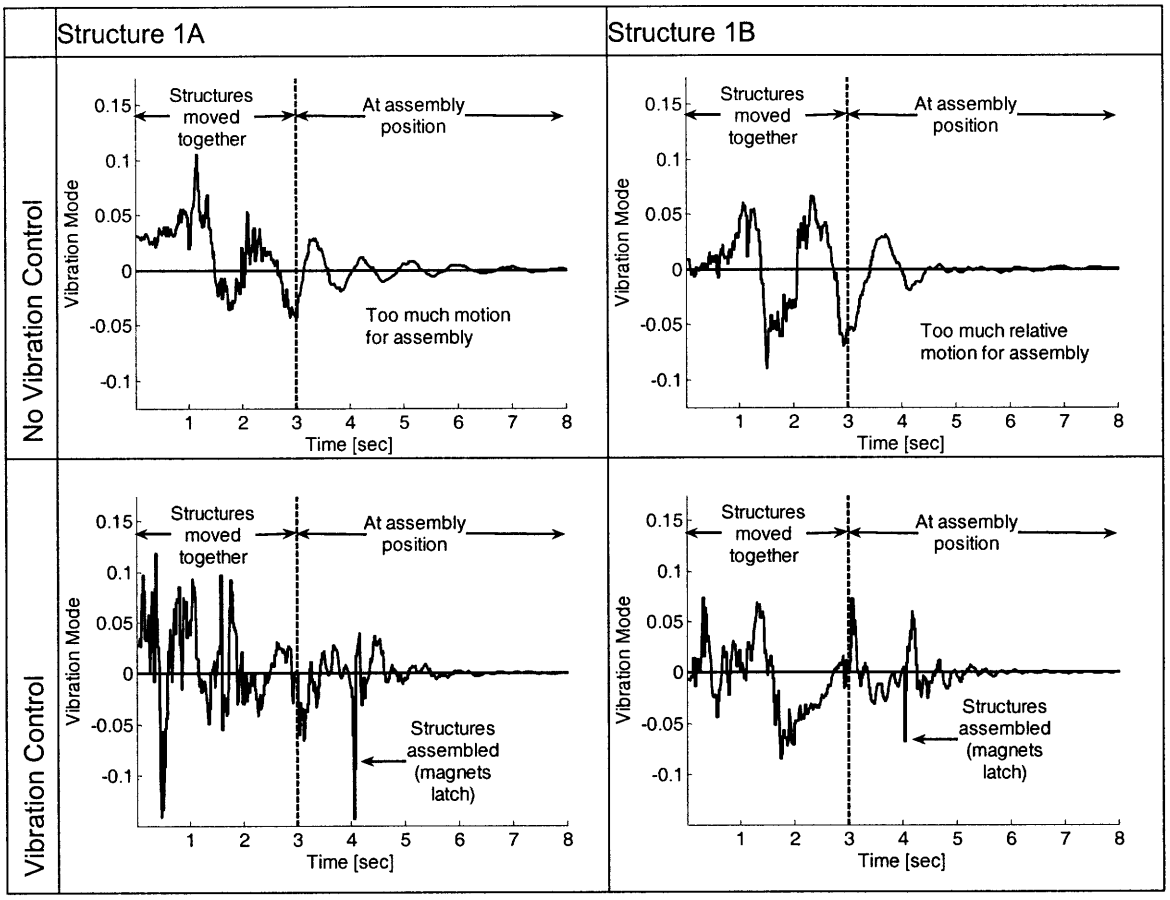

Figure 5.18. First mode of vibration for the assembly experiment.

Figure 5.19 shows the damping ratio for the two controllers for the assembly experiment. The boxes indicate the average while the bars are standard deviation. Structure 1A is gray and structure 1B is white. The vibration controller is able to achieve a higher damping ratio than the controller without vibration suppression. Figure 5.20 shows the settling time for the same case. The vibration controller has a shorter settling time because it removes the vibration more quickly than the other controller. Because the thrusters are turned off, both controllers consume no fuel for this experiment.

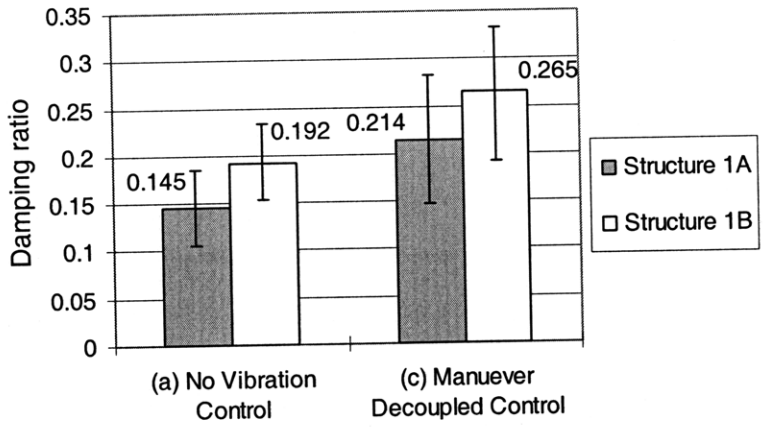

Figure 5.19. Damping ratio for two control methods for both flexible structures for the assembly experiment (averaged over ten runs).

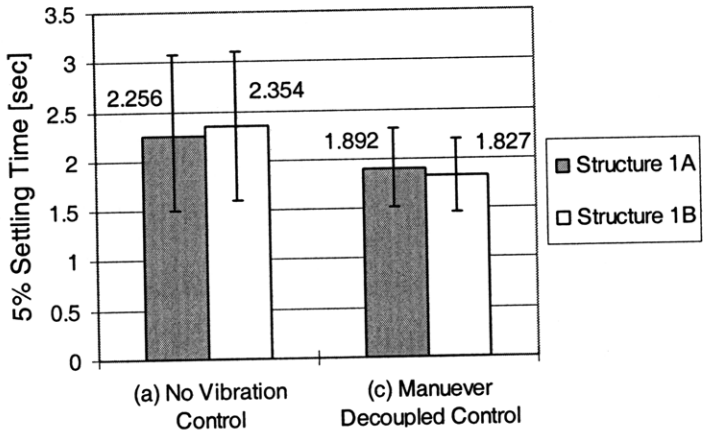

Figure 5.20. Five percent settling time for two control methods for both flexible structures for the assembly experiment (averaged over ten runs).

5.6 Summary

This chapter presented experimental validation of the large space structure vibration controller. Due to limitations on the experimental system sensing and on system bandwidth, the generalized control algorithm as described in Chapter 2 could not be implemented on the experimental hardware. However, the vibration control during assembly is demonstrated.

The robot's controller actively controls the vibration of the structure using the space robots' manipulators while performing the fine assembly maneuver. The results

show that algorithms that consider the effects of structural flexibility have significant performance advantages over ones that do not. Although the algorithms did not include many effects such as computation and sensor delays, the experimental results show no apparent performance degradation from these unmodeled effects. The experimental results suggest that the practical application of this algorithm is feasible.

CHAPTER

6

CONCLUSIONS

This chapter describes the contributions made in this thesis for the on-orbit construction of large flexible structures. It briefly summarizes the contributions chapter by chapter. This chapter concludes with suggestions for future work.

6.1 Contributions of this Thesis

The key contribution of this thesis is to present a general solution for transporting, manipulating and assembling large flexible nonlinear space structures on-orbit using teams of space robots. The approach proposed here transforms the nonlinear system into a set of time-varying linear equations. The structures are able to undergo large displacements and rotations but can be controlled with linear optimal control methods. The method decouples the control of the high-frequency robots from the control of the low-frequency structures and defines the system requirements in terms of bandwidth needed to achieve this. The method allows the robots to act as force sources and effectively maneuver and assemble these large, flexible space structures while minimizing vibration. The thesis also presents methods to mitigate the effects of limited sensing and actuation.

Chapter 1 presented the motivation along with background and literature. Teams of autonomous robots will be needed to construct very large space structures in orbit for use as telescopes and space solar power collectors. These structures will be very

lightweight and flexible. The robots must control vibrations while dealing with the consequences of working in a space environment. However, the coordinated control of teams of robots working in a space environment has not been well studied. The dynamic interactions between the structures and robots make the on-orbit construction of flexible structures a challenging problem.

Chapter 2 introduced a new control algorithm called *Assembly Manipulation Control*. The control approach effectively decouples the control of the high-frequency robots from the control of the low-frequency structures. Decoupling the control allows the robots to serve as interactive force sources that apply forces to the structures and control their dynamic interactions. This approach is possible because of the unique dynamics of the application where the structures are much lower frequency than the robots. The models for these systems are transformed into a set of time-varying linear equations by linearizing about a nominal trajectory. Linear optimal control methods are used to determine the forces needed to position the structures while minimizing their vibration.

Chapter 3 examined limited sensing and actuation in space. Practical issues of weight, complexity and reliability limit available sensing. Precise motion and force control of robots' thrusters and manipulators is needed to effectively maneuver the flexible space structures. These actuation efforts are subject to disturbances and corrupted by nonlinearities such as Coulomb joint friction. For this thesis, a method called Space Base Sensor Control has been developed to compensate for the nonlinear behavior, as shown in Appendix B.

Chapter 4 gives detailed simulation results for a set of problems associated with the construction of a large space telescope. The controller proposed here is compared with other controllers. The simulated results demonstrate the efficacy of the proposed

controller for transportation and assembly tasks. The simulations also show that robots with limited bandwidth are still able to effectively control the flexible structures.

Chapter 5 described the experimental system and presented experimental results. The experimental testbed includes robots that float on a layer of CO_2 emulating two-dimensional weightlessness. These robots maneuver flexible space structures. The chapter presented experimental studies that demonstrate the method can be implemented on a physical system and performs as expected.

6.2 Suggestions for Future Work

This thesis presented studies of large space structure construction with simulation and experimental verification. Before this method could be used for space systems, additional simulation studies of the planned space system and experimental prototyping under the challenging situations expected would be needed.

Practical issues associated with the implementation of this method should be addressed. The sensitivity of the method to noise and sensor error should be studied. Additionally, the sensitivity of the method to errors in the rigid-body and flexible models has not been examined.

Future work could investigate natural extensions to the method presented here that are beyond the scope of this thesis. In particular, the area of optimal trajectory planning for the transportation and maneuvering of large flexible space structures could be expanded. The trajectories used in this thesis for simulation and experimental verification were chosen so that they would be easy to calculate, meet the boundary conditions, and be dynamically achievable. The trajectories are not optimized. With optimal trajectories, improvements in fuel use and vibration reduction are expected. Since the trajectories are directly related to the flexible structure accelerations, the proper

choice of trajectory could also reduce the maximum and average accelerations the structure sees. Lower accelerations are less likely to excite vibrations, and with lower accelerations, the on-off reaction jets for the space robots are less likely to saturate.

Another area that merits further study is very large orbital transportation maneuvers. The first stage of assembly of a large space structure could be done in Low Earth Orbit (LEO) below 2,000 kilometers, and then the partially assembled structures could be boosted to another orbit such as Medium Earth Orbit (MEO), somewhere between LEO and Geostationary Earth Orbit (GEO) at about 36,000 kilometers. The method presented in this thesis for transporting a flexible structure over a long distance is expected to reduce fuel use and vibration when compared to conventional orbital transfer methods. To demonstrate this, effects such as orbital mechanics and gravity gradients that can be neglected for the short time spans studied in this thesis need to be included to accurately model and predict the behavior of such a maneuver.

Assumptions that are made in this thesis could be relaxed and their effects on performance studied. One assumption is that there are no communication delays between the robots or between the robots and the sensors. Communication delays could be modeled as lags in the actuation effort for the robots or as delayed information provided to the Kalman filters for the estimators. Issues of computational burden could also be examined.

Finally, the application for the method proposed in this thesis is the problem of building flexible structures on orbit. However, there is nothing in the algorithm that explicitly limits it to space systems. The method of decoupling the control of high-frequency robots from low frequency flexible elements and manipulating those structures by making the robots behave as force sources is more widely applicable. The method can and should be studied with application to the robotic construction of flexible terrestrial systems.

REFERENCES

1 Anderson, B. D. O. and Moore, J.B., *Optimal Control: Linear Quadratic Methods*, Mineola, N.Y., Dover Publications, 2007.

2 Asada H., and Youcef-Toumi, K., *Direct Drive Robots: Theory and Practice*, Cambridge, MA: MIT Press, 1987.

3 Bilton, A., "Fusion of Remote Vision and On-Board Acceleration Data for the Vibration Estimation of Large Space Structures," M.S. Thesis, Department of Mechanical Engineering, MIT, May 2006.

4 Bilton, A., Ishijima, Y., Lichter, L., and Dubowsky, S. "A Sensor Architecture for the Robotic Control of Large Flexible Space Structures." *The Journal of Field Robotics*, Vol. 24, No. 4, pp. 287-310, April 2007.

5 Blevins, R.D., *Formulas for Natural Frequency and Mode Shape*, Malabar, FL, Krieger Publishing Company, 2001.

6 Bonarini, A., Matteucii, M., and Restelli, M., "Automatic Error Detection and Reduction for an Odometric Sensor based on Two Optical Mice," *Proceedings of the 2005 IEEE International Conference on Robotics and Automation*, Barcelona, Spain, April 2005.

7 Boning, P., Ono, M., Nohara, T., and Dubowsky, S. "An Experimental Study of The Control of Space Robot Teams Assembling Large Flexible Space Structures," *Proceedings of the 9th International Symposium on Artificial Intelligence, Robotics and Automation in Space (i-SAIRAS 2008)*, Pasadena, CA, Feb. 26-29, 2008.

8 Boning, P. and Dubowsky, S. "Identification of Actuation Efforts using Limited Sensory Information for Space Robots," *Proceedings of the 2006 IEEE International Conference on Robotics and Automation*, May 2006.

9 Boning, P. and Dubowsky, S. "A Study of Minimal Sensor Topologies for Space Robots," *10th International Symposium on Advances in Robot Kinematics*, Ljubljana, Slovenia, June 2006.

10 Brogan, W. L., *Modern Control Theory*, Englewood Cliffs, N.J., Prentice Hall, 1991.

11 Brown, R.G., and Hwang, P.Y.C., *Introduction to Random Signals and Applied Kalman Filtering*, 2nd Ed., New York: John Wiley & Sons, 1992.

12 Bryson, A.E., *Control of Spacecraft and Aircraft*, Princeton, New Jersey, Princeton University Press, 1994.

13 Bryson, A.E., and Ho, Y.-C., *Applied Optimal Control: Optimization, Estimation, and Control*, Washington, Hemisphere Publishing (Halstead Press), 1975.

14 CAN in Automation (CiA): Controller Area Network (CAN), http://www.can-cia.com.

15 Chang, K.W., "Shaping Inputs to Reduce Vibration in Flexible Space Structures," M.S. Thesis, Department of Mechanical Engineering, MIT, May 1992.

16 Clark, C., Rock, S., and Latombe, J.C., "Dynamic Networks for Motion Planning in Multi-Robot Space Systems," *Proceedings of the International Symposium of Artificial Intelligence, Robotics and Automation in Space*, Nara, Japan, 2003.

17 Coppa, A., "Robotic Assembly of Truss Beams for Large Space Structures," *AIAA Journal of Spacecraft and Rockets*, Vol. 32, No. 4. pp. 680-685, July-Aug. 1995.

18 Crassidis, J.L., and Markley, F.L., "Unscented Filtering for Spacecraft Attitude Estimation," *AIAA Journal of Guidance, Control, and Dynamics*, Vol. 26, No. 4, pp. 536-542, July-Aug. 2003.

19 Crawley, E.F., Campbell, M.E., and Hall, S.R., *High Performance Structures: Dynamics and Control*, In preparation for publication, Cambridge, MA, 1998.

20 de Wit, C., *Adaptive Control of Partially Known Systems*, Boston, Massachusetts: Elsevier, Vol. 40, No. 3, pp. 419-425, 1988.

21 de Wit, C., Olsson, H., Astrom, K.J., and Lischinsky, P., "A New Model for Control of Systems with Friction," *IEEE Transactions on Automatic Control*, 1996.

22 Dickson, W.C., "Experiments in Cooperative Manipulation of Objects by Free-Flying Robot Teams," Ph.D. Thesis, Department of Aeronautics and Astronautics, Stanford University, 1993.

23 Dickson, W.C., and Cannon, R.H. Jr., "Experimental results of two free-flying robots capturing and manipulating a free-flying object," *IEEE International Conference on Intelligent Robots and Systems*, Aug., 1995.

24 Doggett, W., "Robotic Assembly of Truss Structures for Space Systems and Future Research Plans," *IEEE Aerospace Conference Proceedings*, Big Sky, MT, 2002.

25 Doyle, J., "Guaranteed margins for LQG regulators," *IEEE Transactions on Automatic Control,* Vol. 23, No. 4, pp. 756-757, Aug. 1978.

26 Dubowsky, S. and Boning, P. "The Coordinated Control of Space Robot Teams for the On-Orbit Construction of Large Flexible Space Structures," *Proceedings of the 2007 IEEE International Conference Robotics and Automation, Special Workshop on Space Robotics*, Rome, Italy, April 2007.

27 Dubowsky, S. and Papadopoulos, E. "The Kinematics, Dynamics, and Control of Free-Flying and Free-Floating Space Robotic Systems," *IEEE Transactions on Robotics and Automation, Special Issue on Space Robotics*, Vol. 9, No. 5, pp. 531-543, Oct. 1993.

28 Dunn, H.J., "Experimental Results of Active Control on a Large Structure to Suppress Vibration," *AIAA J. of Guidance, Control and Dynamics*, Vol. 15, No. 6, Nov.-Dec. 1992.

29 Everist, J., Mogharei, K., Suri, H., Ranasinghe, N., Khostnevis, B., Will, P., and Shen, W., "A System for In-Space Assembly," *Proceedings of 2004 IEEE/RSJ International Conference on Intelligent Robots and Systems*, Sendai, Japan, 2004.

30 Gardner, T.N., "Dynamic Analysis of Elastic Mechanical Systems with Clearances," Ph.D. Thesis, University of California, Los Angeles, 1975.

31 Gawronski, W., *Advanced Structural Dynamics and Active Control of Structures*, New York: Springer, 2004.

32 Gralla, E, and de Weck, O., "On-Orbit Assembly Strategies for Space Exploration," *57th International AIAA Astronautical Congress*, Valencia, Spain, Oct. 2-6, 2006.

33 Hara, M., Fukuda, M., Nishibayashi, H., Aiyama, Y., Ota, J., and Arai, T., "Motion Control of Cooperative Transportation System by Quadruped Robots Based on Vibration Model in Walking" *Proceedings of the 1999 IEEE/RSJ International Conference on Intelligent Robots and Systems*, Korea, Oct. 1999.

34 Harlan, A., "Design and Fabrication of a Test Apparatus for Lightweight Flexible Space Modules for Assembly," B.S. Thesis, Department of Mechanical Engineering, MIT, 2007.

35 Huntsberger, T., Stroupe, A., and Kennedy, B., "System of Systems for Space Construction," *IEEE International Conference on Systems, Man, and Cybernetics*, Waikoloa, Hawaii, Oct. 2005.

36 Inalhan, G., Tillerson, M., and How, J.P., "Relative Dynamics and Control of Spacecraft Formations in Eccentric Orbits," AIAA *Journal of Guidance Control and Dynamics*, Jan. 2002.

37 Ipri, S., and Asada, H., "Tuned Dither for Friction Suppression during Force Guided Robotic Assembly," *IEEE International Conference on Intelligent Robots and Systems*, Vol. 1, pp. 310-315, 1995.

38 Ishijima, Y., Tzeranis, D., and Dubowsky, S., "The On-Orbit Maneuvering of Large Space Flexible Structures by Free-Flying Robots," *Proceedings of the 8th International Symposium on Artificial Intelligence, Robotics and Automation in Space, i-SAIRAS*, Munich, Germany, Sept. 2005.

39 Jacobsen, S., "Planning and Control During Robotic Satellite Capture," M.S. Thesis, Department of Mechanical Engineering, MIT, 2003.

40 Kelkar, A., and Joshi, S., *Control of Nonlinear Multibody Flexible Space Structures*, New York: Springer, 1996.

41 Khatib, O., Yokoi, K., Chang, K., Ruspini, D., Holmberg, R., and Casal, A., "Vehicle/Arm Coordination and Multiple Mobile Manipulator Decentralized Cooperation," *Proceedings of the 1996 Conference on Intelligent Robotics and Systems (IROS 1996)*, Osaka, Japan, Nov. 1996.

42 King, D., Reedman, T., and Lymer, J., "Orbital Robotics Evolution for Exploration Enterprise," *Proceedings of the 55th International Astronautical Congress*, Vancouver, Canada, 2004.

43 Kawano, I., Mokuno, M., Kasai, T., and Suzuki, T., "Result of Autonomous Docking Rendezvous Experiment of Engineering Test Satellite ETS-VII," *Journal of Spacecraft and Rockets*, Vol. 38, No. 1, Jan.-Feb. 2001.

44 Lampariello, R., Agrawal, S., and Hirzinger, G., "Optimal Motion Planning for Free-Flying Robots," *Proceedings of the 2003 IEEE International Conference on Robotics and Automation*, Taipei, Taiwan, Sept., 2003.

45 Larson, W.J., and Wertz, J.R., *Space Mission Analysis and Design (3rd Edition)*, Springer-Verlag, 1999.

46 Lichter, M.D., "Shape, Motion, and Inertial Parameter Estimation of Space Objects using Teams of Cooperative Vision Sensors," Ph.D. Thesis, Department of Mechanical Engineering, MIT, 2005.

47 Lichter, M.D., "Electronics Reference Manual for the FSRL Free-Flying Robots," unpublished laboratory documentation, Revision 1, June 23, 2006.

48 Lichter, M.D., and Dubowsky, S., "Shape, Motion, and Parameter Estimation of Large Flexible Space Structures using Range Images," *Proceedings of the 2005 IEEE International Conference on Robotics and Automation (ICRA 2005)*, Barcelona, Spain, pp. 4487-4492, April 2005.

49 Lichter, M.D., Ueno, H., and Dubowsky, S., "Vibration Estimation of Flexible Space Structures using Range Imaging Sensors," *International Journal of Robotics Research*, Vol. 25, No. 10, pp. 1001-1012, Oct. 2006.

50 Lillie, C., "On-Orbit Assembly and Servicing for Future Space Observatories," *Space 2006*, San Jose, California, Sept. 19-21, 2006.

51 Mangalgiri, V., "Analysis for the Robotic Assembly of Large Flexible Space Structures," M.S. Thesis, Department of Mechanical Engineering, MIT, 2004.

52 Mankins, J.C., "A Fresh Look at Space Solar Power: New Architectures, Concepts and Technologies," *Proceedings of the 38th International Astronautical Federation Conference*, 1997.

53 Matsumoto, S., Jacobsen, S., Dubowsky, S., and Ohkami, Y., "Approach Planning and Guidance for Uncontrolled Rotating Satellite Capture Considering Collision Avoidance," *Proceedings of the 7th International Symposium on Artificial Intelligence and Robotics & Automation in Space: i-SAIRAS*, Nara, Japan, 2003.

54 McCamish, S., Romano, M., and Yun, X., "Autonomous Distributed Control Algorithm for Multiple Spacecraft in Close Proximity Operations," *AIAA Guidance, Navigation and Control Conference and Exhibit*, Hilton Head, South Carolina, Aug. 20-23, 2007.

55 Meirovitch, L., *Dynamics and Control of Structures*, New York: John Wiley & Sons, 1990.

56 Miller, D.W., Sedwick, R.J., and Kong, E.M.C., "Electromagnetic Formation Flight for Sparse Aperture Telescopes," *AIAA Journal of Spacecraft and Rockets*, Oct. 2001.

57 *MIT Space Solar Power Workshop*, http://web.mit.edu/space_solar_power/ , May 14-16, 2007.

58 Morel, G. and Dubowsky, S. "The Precise Control of Manipulators with Joint Friction: A Base Force/Torque Sensor Model," *Proceedings of the 1996 IEEE International Conference on Robotics and Automation*, Minneapolis, MN, Vol. 1, pp. 360-365, April 1996.

59 Morel, G., and Dubowsky S., "High Performance Control of Manipulators Using A Base Force/Torque Sensor," Patent Number 5,767,648, May 1998.

60 Morel, G., Iagnemma, K., and Dubowsky, S., "The Precise Control of Manipulators with High Joint-Friction Using Base Force/Torque Sensing," *Automatica: The Journal of the International Federation of Automatic Control*, Vol. 36, No. 7, pp. 931-941, 2000.

61 *NASA James Webb Space Telescope (JWST)* http://www.jwst.nasa.gov/index.html

62 *NASA Space Solar Power (SSP) Exploratory Research and Technology (SERT) Program* (artist Pat Rawlings) Image ID ISC_in_GEO http://www.nasa.gov.

63 *NASA Space Station.* http://www.nasa.gov/mission_pages/station/main/.

64 Newman, W. S., Glosser, G. D., Miller, J.H., and Rohn, D., "The detrimental effect of friction on space microgravity robotics," *Proceedings of the 1992 IEEE International Conference on Robotics and Automation*, Nice, France, Vol. 2, pp. 1436-1441, May 1992.

65 Noran Enginering, NASTRAN Finite Element Software http://www.nenastran.com/newnoran/caseHistory.

66 Oda, M., "ETS-VII: Achievements, Troubles, and Future," *Proceedings of the 6th International Symposium on Artificial Intelligence and Robotics & Automation in Space: i-SAIRAS*, Quebec, Canada, 2001.

67 Oda, M., Ueno, H., and Mori, M., "Study of the Solar Power Satellite in NASDA," *Proceedings of the 7th International Symposium on Artificial Intelligence, Robotics and Automation in Space, i-SAIRAS*, Nara, Japan, 2003.

68 Ono, M., "Experimental Verification of the the Efficient Robotic Transportation Algorithm for Large-scale Flexible Space Structures," M.S. Thesis, Department of Aeronautical and Astronautical Engineering, MIT, Sept. 2007.

69 Ono, M., Boning, P., Nohara, T., and Dubowsky, S., "Experimental Validation of a Fuel-Efficient Robotic Maneuver Control Algorithm for Very Large Flexible Space Structures," *Proceedings of the 2008 IEEE International Conference on Robotics and Automation*, Pasadena, CA, May 2008.

70 Osumi, H., Terasawa, M., and Nojiri, H., "Cooperative Control of Multiple Mobile Manipulators on Uneven Ground," *Proceedings of the 1998 IEEE Conference on Robotics and Automation,* Leuven, Belgium, May 1998.

71 Papadopoulos, E. G., "On the Dynamics and Control of Space Manipulators," Ph.D. Thesis, Department of Mechanical Engineering, MIT, 1990.

72 Pedersen, L., Kortenkamp D., Wettergreen, D., and Nourbakhsh I., "A Survey of Space Robotics," *Proceedings of the 7th International Symposium on Artificial Intelligence, Robotics and Automation in Space, i-SAIRAS*, Nara, Japan, 2003.

73 Pfeffer L.E., Khatib O., and Hake J., "Joint Torque Sensory Feedback of a PUMA Manipulator," *IEEE Transactions on Robotics and Automation*, Vol. 5, No. 4, pp. 418-425, 1989.

74 Preumont, A., *Vibration Control of Active Structures: An Introduction*, Kluwer Academic Publishers, 2002.

75 Romano, M., Friedman, D., and Shay, T., "Laboratory Experimentation of Autonomous Spacecraft Approach and Docking to a Collaborative Target," *Journal of Spacecraft and Rockets*, Vol. 44, No. 1, Jan., 2007.

76 Rus, D., Donald B., and Jennings, J., "Moving furniture with teams of autonomous robots," *Proceedings of the IEEE Conference on Human Robot Interaction and Cooperative Robots*, Pittsburgh, PA, Aug. 1995.

77 Senda, K., Murotsu, Y., Mitsuya, A., Adachi, H., Ito, S., Shitakubo, J., and Matsumoto, T., "Hardware Experiments of Space Truss Assembly by Autonomous Space Robot," *AIAA Guidance, Navigation and Control Conference and Exhibit*, Denver, Colorado, Aug. 2000.

78 Shoemaker, J., and Wright, M., "Orbital Express On-Orbit Satellite Servicing Demonstration," *Proceedings of SPIE Conference on Spacecraft Platforms and Infrastructure, SPIE–International Society for Optical Engineering*, Vol. 5419, pp. 57–65, Bellingham, WA, 2004.

79 SICK Laser Measurement Systems LMS 291 Technical Description, http://www.mysick.com/saqqara/pdf.aspx?id=im0012759.

80 Sidi, M., *Spacecraft Dynamics and Control,* Cambridge, United Kingdom: Cambridge University Press, 1997.

81 Singer, N. C., and Seering, W. P., "Preshaping Command Inputs to Reduce System Vibration," *ASME Journal of Dynamic Systems, Measurement, and Control*, Vol. 112, March 1990.

82 Singh, S. P. N., and Waldron, K. J., "Design and Evaluation of an Integrated Planar Localization Method for Desktop Robotics," *Proceedings of the 2004 IEEE International Conference Robotics and Automation,* New Orleans, LA, April 2004.

83 Singhose, W., Derezinski, S., and Singer, N., "Extra-Insensitive Input Shapers for Controlling Flexible Spacecraft," *AIAA Journal of Guidance, Control, and Dynamics*, 1996.

84 Slotine, J.-J., and Li, W., "On the Adaptive Control of Robot Manipulators," *Int. Journal Robotics Research*, Vol. 6, No. 3, pp. 49-59, Fall 1987.

85 *Space-Based Solar Power as an Opportunity for Strategic Security,* Phase 0 Architecture Feasibility Study, Report to the Director, National Security Space Office, Interim Assessment Release 0.1, Oct. 10, 2007.

86 Staritz, P.J., Skaff, S., Urmson, C., and Whittaker, W., "Skyworker: A Robot for Assembly, Inspection and Maintenance of Large Scale Orbital Facilities," *Proceedings of the 2001 IEEE International Conference on Robotics and Automation (ICRA 2001)*, Seoul, Korea, pp. 4180-4185, May 2001.

87 Stengel, R. F., *Stochastic Optimal Control*, New York, NY, Wiley, 1986.

88 Stroupe, A., Huntsberger, T., Kennedy, B., Aghazarian, H., Baumgartner, E.T., Ganino, A., Garrett, M., Okon, A., Robinson, M., and Townsend, J.A., "Heterogeneous Robotic Systems for Assembly and Servicing," *Proceedings of the 7th International Symposium on Artificial Intelligence, Robotics and Automation in Space, i-SAIRAS*, Munich, Germany, 2005.

89 Sugar, T., and Kumar, V., "Multiple Cooperative Mobile Manipulators," *Proceedings of the 1999 IEEE International Conference on Robotics and Automation*, Detroit, Michigan, May 1999.

90 Tillerson, M., Breger, L., and How, J. P., "Distributed Coordination and Control of Formation Flying Spacecraft," *Proceedings of the IEEE American Control Conference*, June 2003.

91 Tortopidis, I., and Papadopolous, E., "On Point-to-Point Motion Planning for Underactuated Space Manipulator Systems," *Robotics and Autonomous Systems*, July 2006.

92 Tuttle, T. D., "Creating Time-Optimal Commands for Linear Systems," Ph.D. Thesis, Department of Mechanical Engineering, MIT, May, 1997.

93 Tzeranis, D., "Manipulation of Flexible Structural Modules by Space Robots During LSS Construction," M.S. Thesis, Department of Mechanical Engineering, MIT, May 2005.

94 Tzeranis, D., and Dubowsky, S., "Vibration Control in the Assembly of Large Flexible Structures by Teams of Space Robots," *Proceedings of SYROCO 2006: 8th IFAC Int'l Symposium on Robot Control*, Bologna, Italy, 2006.

95 Tzeranis, D., Ishijima, Y., and Dubowsky, S., "Manipulation of Large Flexible Structural Modules by Robots Mounted on Large Flexible Structures," *Proceedings of the 8th International Symposium on Artificial Intelligence, Robotics and Automation in Space, i-SAIRAS*, Munich, Germany, Sept. 2005.

96 Ueno, H., Mangalgiri, V., Dubowsky, S., Sekiguchi, T., Oda, M., and Ohkami, Y., "Simulation Analysis and Experiments of On-orbit Assembly Behavior on Flexible Structure by Cooperative Robots," *Proceedings of the 24th International Symposium on Space Technology and Science (ISTS)*, Miyazaki, Japan, May 2004.

97 Ueno, H., Nishimaki, T., Oda, M., and Inaba, N., "Autonomous Cooperative Robots for Space Structure Assembly and Maintenance," *Proceedings of the 7th International Symposium on Artificial Intelligence, Robotics, and Automation in Space: i-SAIRAS 2003*, NARA, Japan, May 2003.

98 Ueno, H., Oda, M., and Inaba, K., "Robotics Experimental Study for SSPS Walking and Assembly Technology," *Proceedings of the 8th International Symposium on Artificial Intelligence, Robotics and Automation in Space, i-SAIRAS*, Munich, Germany, Sept. 2005.

99 Vischer, D., and Khatib, O., "Design and Development of High-Performance Torque-Controlled Joints," *IEEE Transactions on Robotics and Automation*, Vol. 11, No. 4, pp. 537-544, Aug. 1995.

100 Wan, E.A., and van der Merwe, R. "The Unscented Kalman Filter," *Kalman Filtering and Neural Networks*, pp. 221-280, Edited by Simon Haykin, New York: Wiley Publishing, 2001.

101 Wang, P., "Navigation Strategies for Multiple Autonomous Mobile Robots Moving in Formation," *IEEE/RSJ International Workshop on Intelligent Robots and Systems*, Tsukuba, Japan, Sept. 1989.

102 Whittaker, W., Staritz, P., Ambrose, R., Kennedy, B., Fredrickson, S., Parrish, J., and Urmson, C., "Robotic Assembly of Space Solar-Power Facilities," *Journal of Aerospace Engineering*, Vol. 14, No. 2, April, 2001.

103 Woffinden, D., and Geller, D., "Navigating the Road to Autonomous Orbital Rendezvous," *Journal of Spacecraft and Rockets*, Vol. 44, No. 4, July–August 2007.

APPENDIX

A

CONTROL SYSTEM PROPERTIES

This appendix examines control systems properties for the space systems used in this thesis. In particular, Section A.1 reviews controllability and observability and the looser properties of stabilizability and detectability for linear time-varying systems [1]. In Section A.2, these properties are applied to time-varying flexible space systems and used to examine stability in Section A.3. This appendix focuses on these properties as they relate to systems studied in this thesis. The proof of stability for the general system is usually demonstrated via the Lemma of Lyapunov and is not repeated here [1][10].

A.1 Controllability and Observability

For a time-varying system, the determination of stability requires solution of the system and computation of controllability and observability gramians. The time-varying system is written:

$$\begin{aligned} \dot{\mathbf{x}}(t) &= \mathbf{A}(t)\mathbf{x}(t) + \mathbf{B}(t)\mathbf{u}(t) \\ \mathbf{y}'(t) &= \mathbf{C}(t)\mathbf{x}(t) \end{aligned} \tag{A.1}$$

where the dimension of $\mathbf{A}$ is $n \times n$, the dimension of $\mathbf{B}$ is $n \times r$, and $\mathbf{C}$ has dimensions $n \times m$. The state vector $\mathbf{x}$ has n elements, the control vector $\mathbf{u}$ has r elements, and the output vector $\mathbf{y}'$ has m elements. Although the solution of Equation (A.1) may not be determined analytically for all cases, it can be expressed in terms of the transition matrix

$\Psi(t,t_0)$. (The Ψ matrix notation is used for the transition matrix instead of the more commonly used variable Φ to avoid confusion with the flexible modes shapes.) The transition matrix is defined as the solution to the differential equation:

$$\frac{d\Psi(t,\tau)}{dt} = \mathbf{A}(t)\Psi(t,\tau) \tag{A.2}$$

along with the mapping $\Psi(\tau,\tau) = \mathbf{I}$ for any τ ($\mathbf{I}$ is the $n \times n$ identity matrix). A closed form solution is available when the matrix $\mathbf{A}$ is constant or diagonal and for a few other special cases. Otherwise the transition matrix can be found by numerical solution of Equation (A.2) or by successive approximations.

Using the transition matrix, the solution to Equation (A.1) is found to provide a mapping from the control vector $\mathbf{u}$ to the state vector $\mathbf{x}$. The transformation from the control vector to the state vector leads the to controllability gramian [1]:

$$\mathbf{G}(t_0,t_1) = \int_{t_0}^{t_1} \Psi(t_1,\tau)\mathbf{B}(\tau)\mathbf{B}^{\mathrm{T}}(\tau)\Psi^{\mathrm{T}}(t_1,\tau)d\tau \tag{A.3}$$

The time-varying system is completely controllable if the matrix $\mathbf{G}(t_0,t_1)$ is positive definite. Observability is determined from the observability gramian:

$$\mathbf{H}(t_0,t_1) = \int_{t_0}^{t_1} \Psi^{\mathrm{T}}(t_1,\tau)\mathbf{C}^{\mathrm{T}}(\tau)\mathbf{C}(\tau)\Psi(t_1,\tau)d\tau \tag{A.4}$$

As the dual of controllability, the system is completely observable if the matrix $\mathbf{H}(t_0,t_1)$ is positive definite.

To be stable under linear quadratic optimal control, a time-varying system must be stabilizable. A system is completely stabilizable if all the uncontrollable modes are asymptotically stable, or in other words, the modes that are not controlled stay bounded. To be stable, the system must also be detectable. Detectability is the dual of stabilizability, and requires that the unobservable modes be stable.

A.2 Application to Large Flexible Space Systems

The large time-varying flexible space systems studied in this thesis were examined for stabilizability and detectability. In general, no closed form solution exists. However, for the simulated systems it is possible to evaluate the integrals numerically. For the systems studied in earlier chapters, the controllability and observability gramians are calculated and the systems are determined to be controllable and observable (and hence stabilizable and detectable).

A.3 Stability

In this section, the effect of the optimal LQG control on the stability of the closed-loop system is examined. For the problem of large space structure transportation and assembly in this thesis, the optimal control problem is formulated as a tracking problem, with a non-zero final state $\mathbf{x}_{des}$ and an optional trajectory $\tilde{\mathbf{x}}(t)$. This cost function is repeated from Section 2.6:

$$\begin{aligned} J = &[\mathbf{x}(t_f) - \mathbf{x}_{des}]^{\mathrm{T}} \mathbf{M}_f [\mathbf{x}(t_f) - \mathbf{x}_{des}] \\ &+ \int_{t_0}^{t_f} \left\{ [\mathbf{x}(t) - \tilde{\mathbf{x}}(t)]^{\mathrm{T}} \mathbf{Q} [\mathbf{x}(t) - \tilde{\mathbf{x}}(t)] + \mathbf{u}(t)^{\mathrm{T}} \mathbf{R} \mathbf{u}(t) \right\} dt \end{aligned} \tag{A.5}$$

When there is no trajectory and the final position is the origin, the problem becomes a regulator problem with cost function:

$$J = \int_{t_0}^{t_f} \left\{ \mathbf{x}(t)^{\mathrm{T}} \mathbf{Q} \mathbf{x}(t) + \mathbf{u}(t)^{\mathrm{T}} \mathbf{R} \mathbf{u}(t) \right\} dt \tag{A.6}$$

For the purposes of stability analysis, the regulator problem and the tracking problem are equivalent, so the simpler regulator problem is studied. Provided the conditions on stabilizability and detectability are met, the addition to the system of

closed-loop control found from the solution of the Riccati equation allows the linear quadratic system to have a phase margin $PM \geq 60°$ and a gain margin $GM = \infty$ [10].

In practice, exponential stability of the system is required, because asymptotic stability leads to problems with robustness when there are errors in the system model [25][87]. This is particularly true for systems with lightly damped structural modes such as space structures. Increasing the performance demands on the rigid-body and lower modes of the system can cause the influence to 'spill over' onto the higher modes, and lead to instability.

APPENDIX

B

LIMITED SENSING AND ACTUATION COMPENSATION

This appendix discusses details of compensation for limited sensing and actuation in space robots. Section B.1 gives the system description and assumptions. Space Base Sensor Control (SBSC), described in Chapter 3, is an extension of Base Sensor Control [8][58][60]. The method allows multi-actuator sensing with a reduced number of actuators. Section B.2 describes SBSC in detail. This method is used to determine the minimal number and best placement of sensors for a given robot [9]. Section B.3 presents details of this theoretical development. Simulation results are given in Section B.4. Configurations of one and two-manipulator space robots are examined, and the minimal number of sensors shown. The results are summarized in Section B.5.

B.1 System Description and Assumptions

The systems studied are 3D free-flying space robots with multiple manipulators (see Figure B.1). Each of the p manipulators has n links. It is assumed that there is a six-axis force/torque sensor between each manipulator and its spacecraft. Manipulators are assumed to have rotary joints, but the method developed here can be extended to translational joints. It is assumed that the spacecraft and links are 3D rigid bodies (fuel sloshing and flexible modes of the robot are not considered). The efforts of all the thrusters are represented by a single force and moment applied at the center of mass of

the spacecraft. Actuator forces and moments, friction at each joint, and reaction jet forces are assumed unknown. Further, it is assumed that there are no additional external loads acting on the system. Gravity gradient effects are neglected because they are small compared to the other forces. For this study, quantities measured, including accelerations, are assumed to be known exactly. If the manipulator is holding a payload, a firm grasp by the end-effector is assumed.

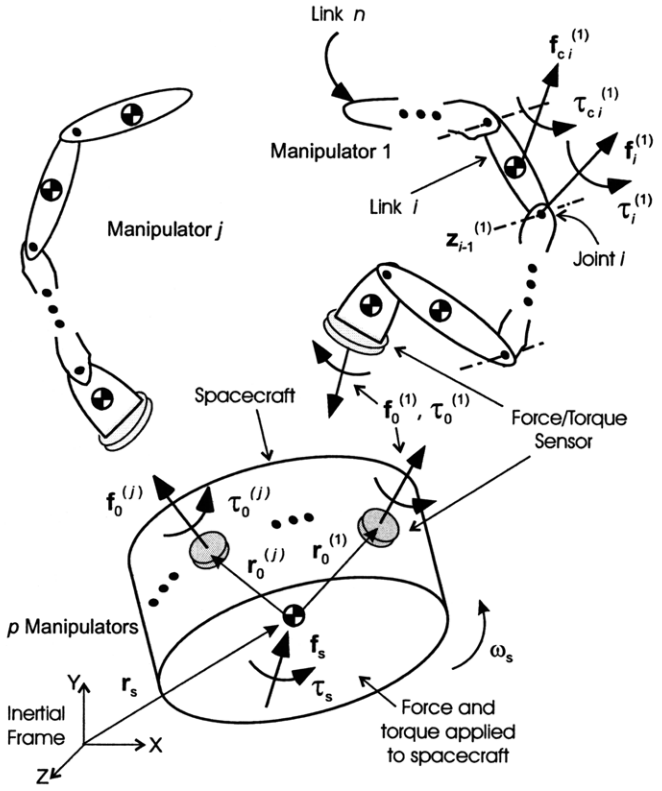

Figure B.1. System model with coordinates.

The sensors force/torque measurements are used to identify the net torque output of the manipulator's actuators. The same measurements are used to identify spacecraft thruster outputs. Other measured quantities are joint angles for each of the j manipulators ($\mathbf{q}^{(j)}$), linear acceleration of the spacecraft ($\dot{\mathbf{v}}_s = \ddot{\mathbf{r}}_s$), spacecraft orientation ($\boldsymbol{\theta}$), angular velocity of the spacecraft ($\boldsymbol{\omega}_s$), and angular acceleration of the spacecraft ($\dot{\boldsymbol{\omega}}_s$), as shown in Figure B.2.

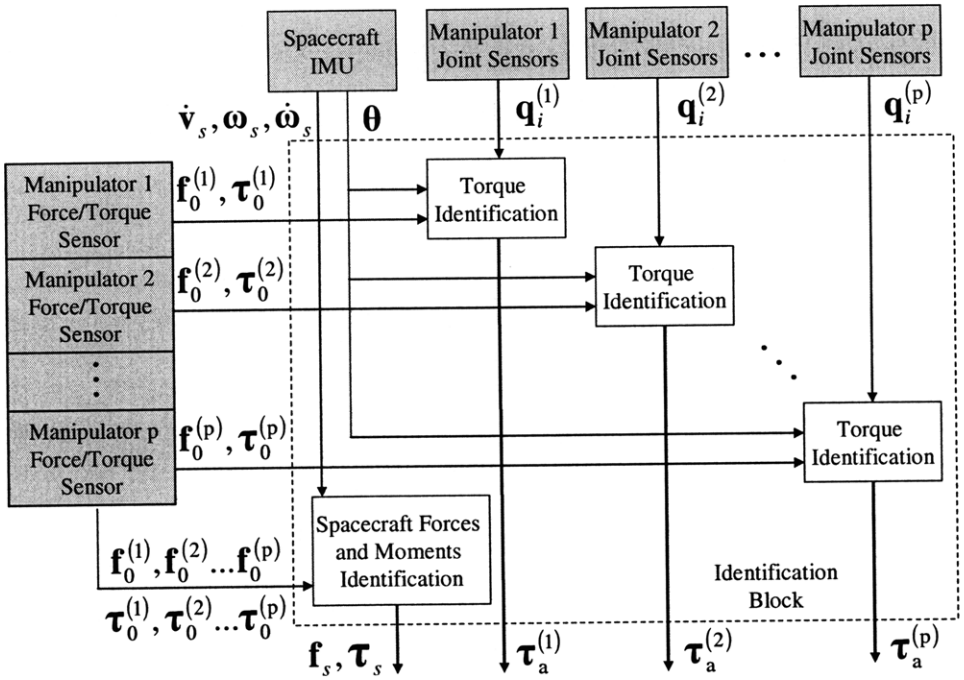

Figure B.2. Actuation effort identification flowchart.

B.2 Space Base Sensor Control Method

The equations for linear momentum $\mathbf{p}_s$ and angular momentum $\mathbf{H}_s$ at the center of mass of the spacecraft are:

$$\begin{aligned} \mathbf{p}_s &= m_s \mathbf{v}_s \\ \mathbf{H}_s &= \mathbf{I}_s \boldsymbol{\omega}_s \end{aligned} \tag{B.1}$$

where $\mathbf{I}_s$ is the spacecraft inertia tensor and m_s is the spacecraft mass. From conservation of momentum, the time derivative of the momentum is equal to the forces and torques applied to the spacecraft:

$$\begin{aligned} \dot{\mathbf{p}}_s &= \sum \mathbf{f}^{ext} \\ \dot{\mathbf{H}}_s &= \sum \boldsymbol{\tau}^{ext} \end{aligned} \tag{B.2}$$

Referring to Figure B.1, where $\mathbf{f}_0^{(j)}$ are the forces and $\boldsymbol{\tau}_0^{(j)}$ are the torques measured by the sensors for the *j*th manipulator, the dynamics of the spacecraft can be

written as a function of the forces and torques and the measured forces and torques applied by the manipulators:

$$\begin{aligned} m_s \dot{\mathbf{v}}_s &= \mathbf{f}_s - \sum_{j=1}^{p} \mathbf{f}_0^{(j)} \\ \mathbf{I}_s \dot{\boldsymbol{\omega}}_s + \boldsymbol{\omega}_s \times (\mathbf{I}_s \boldsymbol{\omega}_s) &= \boldsymbol{\tau}_s - \sum_{j=1}^{p} \left(\boldsymbol{\tau}_0^{(j)} + \mathbf{r}_{s,0}^{(j)} \times \mathbf{f}_0^{(j)} \right) \end{aligned} \tag{B.3}$$

where $\mathbf{r}_{s,0}^{(j)}$ is a vector from the center of mass of the spacecraft to the *j*th sensor. To find the forces and torques applied to the spacecraft, the terms are rearranged to yield:

$$\begin{aligned} \mathbf{f}_s &= \sum_{j=1}^{p} \mathbf{f}_0^{(j)} + m_s \dot{\mathbf{v}}_s \\ \boldsymbol{\tau}_s &= \sum_{j=1}^{p} \left(\boldsymbol{\tau}_0^{(j)} + \mathbf{r}_{s,0}^{(j)} \times \mathbf{f}_0^{(j)} \right) + \mathbf{I}_s \dot{\boldsymbol{\omega}}_s + \boldsymbol{\omega}_s \times (\mathbf{I}_s \boldsymbol{\omega}_s) \end{aligned} \tag{B.4}$$

This can be rewritten to yield vectors of spacecraft forces and torques:

$$\begin{aligned} \mathbf{f}_s &= \sum_{j=1}^{p} \mathbf{A}_{fs}^{(j)}(\boldsymbol{\theta}) \begin{bmatrix} \mathbf{f}_0^{(j)} \\ \boldsymbol{\tau}_0^{(j)} \end{bmatrix} - f(\boldsymbol{\theta}, \boldsymbol{\omega}_s, \dot{\boldsymbol{\omega}}_s, \dot{\mathbf{v}}_s) \\ \boldsymbol{\tau}_s &= \sum_{j=1}^{p} \mathbf{A}_{\tau s}^{(j)}(\boldsymbol{\theta}) \begin{bmatrix} \mathbf{f}_0^{(j)} \\ \boldsymbol{\tau}_0^{(j)} \end{bmatrix} - f(\boldsymbol{\theta}, \boldsymbol{\omega}_s, \dot{\boldsymbol{\omega}}_s, \dot{\mathbf{v}}_s) \end{aligned} \tag{B.5}$$

with the $\mathbf{A}$ matrices given by:

$$\begin{aligned} \mathbf{A}_{fs}^{(j)}(\boldsymbol{\theta}) &= \begin{bmatrix} \mathbf{1} & \mathbf{0} \end{bmatrix} \\ \mathbf{A}_{\tau s}^{(j)}(\boldsymbol{\theta}) &= \begin{bmatrix} \mathbf{S}_{s,0}^{(j)} & \mathbf{1} \end{bmatrix} \end{aligned} \tag{B.6}$$

where $\mathbf{1}$ is the identity matrix and $\mathbf{0}$ is the zero matrix. The skew symmetric matrix $\mathbf{S}_{a,b}$ denotes cross product, $\mathbf{S}_{a,b}\mathbf{f} \equiv \mathbf{r}_{a,b} \times \mathbf{f}$ where $\mathbf{r}_{a,b}$ is a vector from point *a* to point *b*, and $\mathbf{S}_{s,0}^{(j)}$ is therefore the cross product matrix from the origin of the spacecraft to the origin of the force/torque sensor for the *j*th manipulator.

In addition to the estimation of the forces and torques applied to the spacecraft, the joint torques can be estimated. To calculate the applied joint torques, the dynamics of the links in the manipulator are included in the formulation. Since the links all belong to the same manipulator, the superscript *j* has been dropped to simplify the notation. Writing

the relationship to find the forces $\mathbf{f}_{ci}$ and torques $\boldsymbol{\tau}_{ci}$ at the center of mass of *i*th link in the system yields:

$$\begin{aligned}\mathbf{f}_{ci} &= m_i \dot{\mathbf{v}}_{ci} = \sum \mathbf{f}_{ci}^{ext} \\ \boldsymbol{\tau}_{ci} &= \mathbf{I}_i \dot{\boldsymbol{\omega}}_i + \boldsymbol{\omega}_i \times (\mathbf{I}_i \boldsymbol{\omega}_i) = \sum \boldsymbol{\tau}_{ci}^{ext}\end{aligned} \tag{B.7}$$

The forces at the *i*th joint $\mathbf{f}_i$ can be calculated (with $\mathbf{f}_0$ measured by the manipulator force/torque sensor):

$$\mathbf{f}_i = \mathbf{f}_0 - \sum_{k=0}^{i-1} \mathbf{f}_{ck} \tag{B.8}$$

Similarly, the torques at the *i*th joint $\boldsymbol{\tau}_i$ can be calculated:

$$\boldsymbol{\tau}_i = \boldsymbol{\tau}_0 - \mathbf{r}_{0,i} \times \mathbf{f}_0 - \sum_{k=0}^{i-1} \left(\boldsymbol{\tau}_{ck} + \mathbf{r}_{ck,i} \times \mathbf{f}_{ck} \right) \tag{B.9}$$

where $\mathbf{r}_{0,i}$ is a vector from the origin of the force/torque sensor (the 0^{th} joint) to the origin of the *i*th joint, and $\mathbf{r}_{ck,i}$ is a vector from the center of mass of the *k*th link to the origin of the *i*th joint. This torque is projected onto the axis of the joint to calculate the applied joint torque:

$$\tau_{ai} = \mathbf{z}_{i-1}^{\mathrm{T}} \boldsymbol{\tau}_i \tag{B.10}$$

where $\mathbf{z}_{i-1}$ is a unit vector aligned with the axis of the joint's rotation. Equations (B.7)-(B.10) are combined and the superscript notation indicating manipulator number is again shown to yield a vector of joint torques of the form:

$$\boldsymbol{\tau}_a^{(j)} = \mathbf{A}_{\tau a}^{(j)}(\mathbf{q}^{(j)}, \boldsymbol{\theta}) \begin{bmatrix} \mathbf{f}_0^{(j)} \\ \boldsymbol{\tau}_0^{(j)} \end{bmatrix} - f(\boldsymbol{\theta}, \mathbf{q}^{(j)}, \dot{\mathbf{q}}^{(j)}, \ddot{\mathbf{q}}^{(j)}, \boldsymbol{\omega}_s, \dot{\boldsymbol{\omega}}_s, \dot{\mathbf{v}}_s) \tag{B.11}$$

where each row *i* of $\mathbf{A}_{\tau a}^{(j)}$ is given by:

$$\mathbf{A}_{\tau a\ i}^{(j)} = \left(\mathbf{z}_{i-1}^{(j)}\right)^{\mathrm{T}} \mathbf{S}_{i-1,0}^{(j)} + \left(\mathbf{z}_{i-1}^{(j)}\right)^{\mathrm{T}} \tag{B.12}$$

and $\mathbf{S}_{i-1,0}^{(j)}$ is the cross product matrix from the origin of the *i*-1th joint to the origin of the force/torque sensor for the *j*th manipulator. The $\mathbf{A}$ matrices are relatively simple to derive and require minimal computation for generating the actuator estimates. When large external forces are absent and joint accelerations and velocities are relatively low,

such as for a free-flying robot performing precision motions, the forces and torques can be estimated by neglecting the higher order terms. Calculations have shown that these terms are small compared to the magnitude of the applied actuation effort, in which case Equation (B.11) reduces to:

$$\hat{\boldsymbol{\tau}}_a^{(j)} = \mathbf{A}_{\tau a}^{(j)}(\mathbf{q}^{(j)}, \boldsymbol{\theta}) \begin{bmatrix} \mathbf{f}_0^{(j)} \\ \boldsymbol{\tau}_0^{(j)} \end{bmatrix} \tag{B.13}$$

Similarly the estimates for the net thruster forces and torques become:

$$\begin{aligned} \hat{\mathbf{f}}_s &= \sum_{j=1}^{p} \mathbf{A}_{fs}^{(j)}(\boldsymbol{\theta}) \begin{bmatrix} \mathbf{f}_0^{(j)} \\ \boldsymbol{\tau}_0^{(j)} \end{bmatrix} \\ \hat{\boldsymbol{\tau}}_s &= \sum_{j=1}^{p} \mathbf{A}_{\tau s}^{(j)}(\boldsymbol{\theta}) \begin{bmatrix} \mathbf{f}_0^{(j)} \\ \boldsymbol{\tau}_0^{(j)} \end{bmatrix} \end{aligned} \tag{B.14}$$

With the applied joint torques and the net thruster forces estimated, compensation for these errors in the actuation in a closed-loop controller for free-flying and free-floating space robots becomes possible [27].

B.3 Determining Minimal Sensors

The approach taken to determine minimal sensors is to divide the system at each six-axis force/torque sensor into subsystems [9]. The subsystems are categorized by a small set of canonical elements. The dynamics of the canonical elements are analyzed using Newton's method to find intermediate forces and torques. Finally, the results are applied to the original system to find the minimum number of sensors required to calculate the actual net joint efforts (eliminating the effects of friction), thruster forces, and reaction wheel moments. This section gives details of this approach.

B.3.1 Categorizing by Canonical Element

All of the subsystems created by isolating sections for the space robots at the force/torque sensors can be reduced to the canonical elements in Figure B.3. The

force/torque sensors provide the known interface forces and moments. The canonical element for a given subsystem is determined by reducing the subsystem, following the rules shown in Figure B.4. First, the system is divided at the force/torque sensors, and the sensors are replaced with equal and opposite known force/torques. Next, zero end loads at the end-effectors are replaced with known force/torques, because zero loads are also known loads. Adding these zero loads allows more cases to be considered as one type. Then, reaction jets are replaced with unknown force/torques. Finally, branches are replaced with chains. A known load applied at the end of a chain is equivalent to a known load applied at the branching point. The same is true for an unknown load.

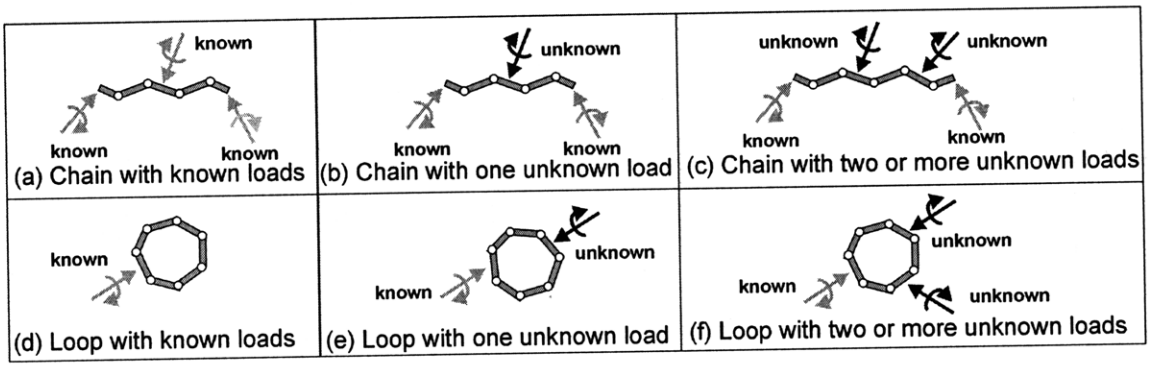

Figure B.3. Canonical system elements.

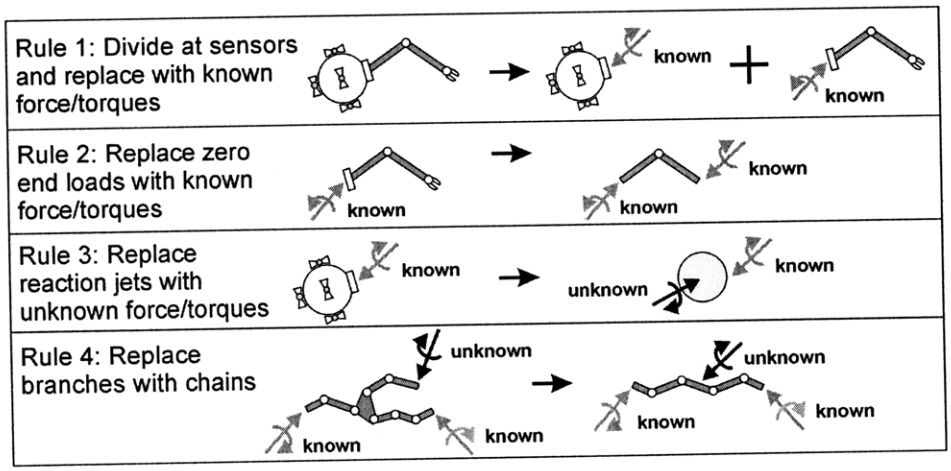

Figure B.4. Reduction to canonical elements.

An example of the application of these rules is given in Figure B.5, showing how the unknown reaction jets on a spacecraft become the canonical element chain with one unknown. Figure B.6 shows more examples. Figure B.6 (a) (Case 1) is a free-floating (no thrusters) space robot with two manipulators and a single force/torque sensor. The sensor separates the system into two canonical elements, both chains with known loads. Figure B.6 (b) (Case 2) shows a free-floating robot with a single sensor at the wrist, equivalent to a chain with known loads. The sensor measures very little, because there is no payload in this case. Figure B.6 (c) (Case 2) shows a free-flying space robot with a single sensor between the spacecraft and both manipulators. Figure B.6 (d) (Case 4) shows a free-flying space robot that contains a closed kinematic chain or loop.

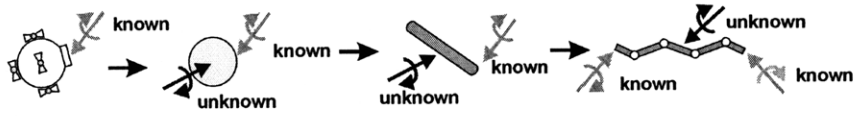

Figure B.5. Reduction of unknown reaction jets to chain with one unknown.

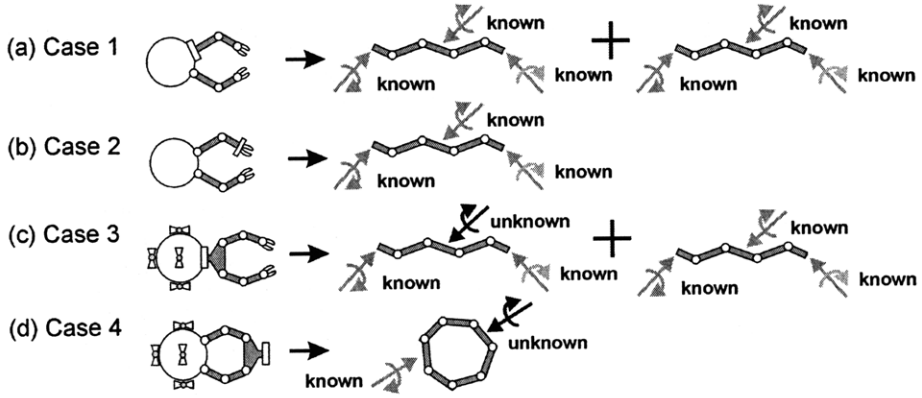

Figure B.6. More reduction examples.

B.3.2 Dynamic Analysis

The objective of this section is to determine if enough sensory information exists for a given subsystem topology to find the net actuator forces and moments on all joints and links in the subsystem. The friction at unactuated joints can also be measured. The

analysis is for a full 3D system (see Figure B.1). Figure B.7 shows a typical link, and Figure B.8 shows a link at a branch point.

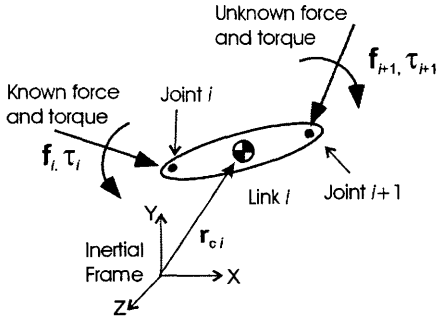

Figure B.7. Link with one unknown load.

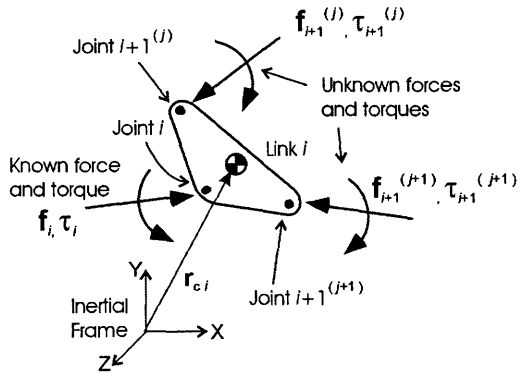

Figure B.8. Link with two unknown loads.

When there are two unknown forces (such as in Figure B.8), the forces and torques cannot be calculated directly. This situation can often be solved by starting at several points in the chain and propagating the known forces and moments to a common point. In other cases, additional information, such as provided by an additional force/torque sensor, is needed to permit a solution. When all of the links in the system have been visited, determining if the given set of sensors is sufficient or if additional sensors are required is possible.

B.3.3 Analysis of Canonical Elements

The above analysis can be applied case by case to the canonical elements in Figure B.3. First, consider the chain with known loads, as in Figure B.3 (a). By starting

with the link on the far left, finding the actuator torques on the first joint is possible. Continuing with the links from left to right, calculation can yield the forces and torques on all joints in this system. Hence, enough sensors exist to completely identify all actuation efforts for this case.

The canonical element chain with one unknown load also has enough sensors, but working inward from both ends of the chain simultaneously is necessary so that the single unknown load at the middle link can be determined. However, for any chain that has more than one unknown load, as in Figure B.3 (c), all actuator efforts cannot be determined without adding more sensors.

Loops can be resolved into two chains joined by two branching links. Loops are analyzed by starting with a link that has only known applied loads and propagating the loads in both directions around the loop until the chain rejoins. Enough sensors do not exist to determine all actuation efforts for any of the three canonical elements with loops. However, inserting a sensor in a loop converts this problem into the case of the chain with known loads (Figure B.3 (a)). To summarize, for all the canonical elements, only a chain with known loads, as in Figure B.3 (a), and a chain with one unknown load, as in Figure B.3 (b), have enough sensory information to determine all actuation efforts.

By using the analysis of the canonical elements, applying the results to the original system to determine sensor placement is straightforward. For any given robot configuration with multiple manipulators, links, branches, etc., it is possible to enumerate potential sensor placements, divide the system into subsystems at the sensors, classify each subsystem by its canonical element, eliminate the layouts where not enough sensory information exists, and find the minimal number and placement of sensors for the system.

B.3.4 System Topologies

Systems such as that depicted in Figure 2.1 are studied to determine the torques at each joint and the reaction jet forces. The parameters varied are number of manipulators (p = 1, 2), number of links per manipulator (n = 1, 2, many), reaction jets or not (free-flying or free-floating), and payload or not. The primary locations for sensor placement are the manipulator wrist and the manipulator base where the manipulator joins the spacecraft. For most cases, enumerating all the cases where the sensor is placed at any joint in between is unnecessary, because the cases are often equivalent to the cases where sensors are placed at the ends of the manipulators.

B.3.5 Minimum Sensor Configurations

The sensor placement method presented above is applied to space robots with one and two manipulators. A collection of single manipulator cases with and without thrusters is summarized in Figure B.9. In all cases with a single manipulator, adequate sensing existed. Figure B.10 through Figure B.13 summarize the results for space robots with two manipulators. The cases in Figure B.10 do not have (or are not firing their) thrusters. The first row shows possible sensor placements when one sensor is available. The sensor can be placed between the manipulator and the spacecraft, at the end effector, between both manipulators and the spacecraft, or at both end-effectors. The second row shows placement of two sensors, the third row shows placement of three sensors, and the last row shows the only configuration with four sensors. All cases reduce to the canonical chain elements with at most one unknown load, except for the two loop cases that are crossed out. The crossed out cases do not have enough sensing to determine all actuation efforts. From the remaining cases that do have enough information, determining the minimal sensors (one) and its potential locations is straightforward. These cases are outlined in bold. Figure B.11 shows the same cases as Figure B.10, except that the space

robots now have thrusters. The addition of the unknown thruster loads does not change the results; there are still only two cases that do not have enough sensing, and a single force torque sensor is enough to determine actuation.

Figure B.12 shows robots that have no thrusters but carry a payload grasped by both manipulators, creating a closed loop. Most of the loops are broken by a sensor so actuation can be determined, but two places exist to put a single sensor to determine actuation. Figure B.13 shows the robots from Figure B.12 with thrusters. Once again, addition of unknown thruster forces does not significantly change the results.

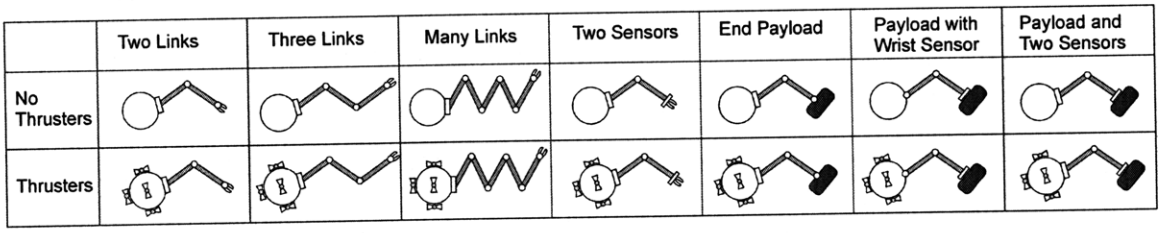

Figure B.9. Space robot configurations for a single manipulator.

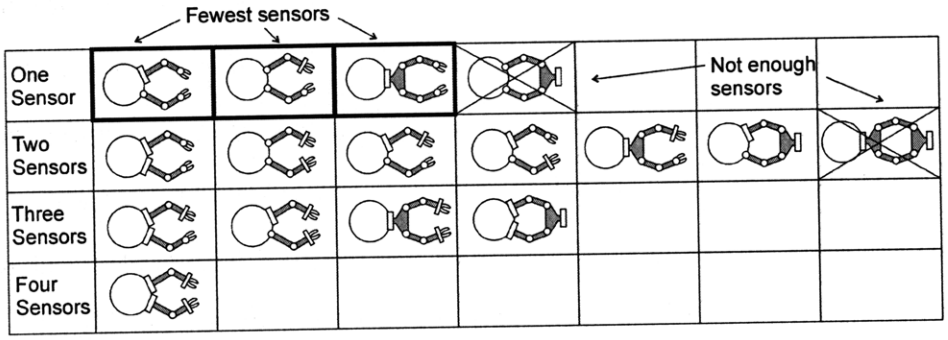

Figure B.10. Space robot configurations for two manipulators and no thrusters.

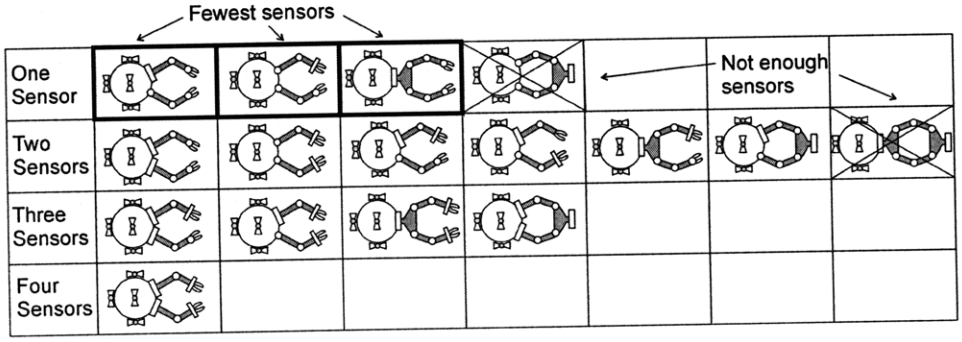

Figure B.11. Space robot configurations for two manipulators and thrusters.

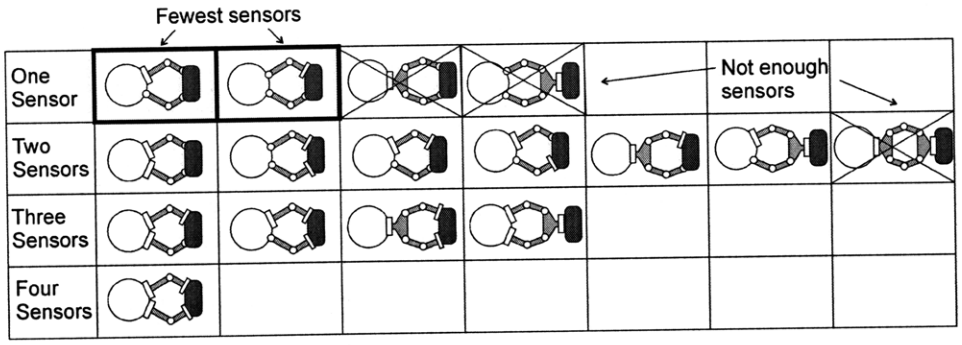

Figure B.12. Space robot configurations for two manipulators and payload.

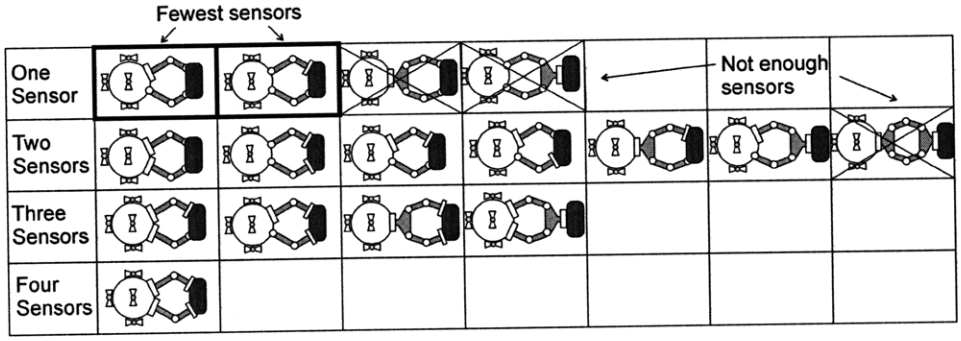

Figure B.13. Space robot configurations for two manipulators, payload, and thrusters.

B.4 Simulation Results

The large space structure construction discussed in this thesis is one mission where precise control is important for space robots. Precise sensing and actuation is also needed by space robots for satellite capture missions (see Figure B.14). The results presented here show the application of the Space Base Sensor Control method to the satellite capture task.

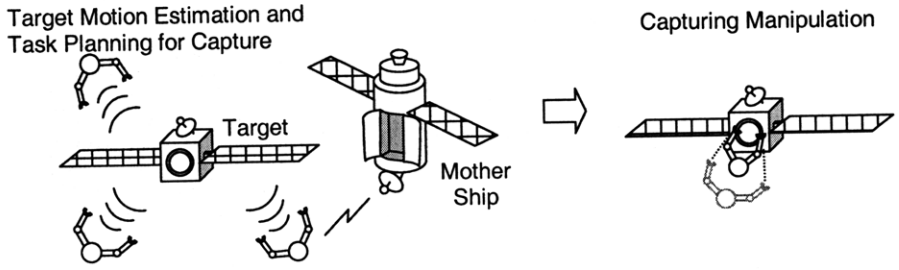

Figure B.14. Mission scenario for robotic satellite capture.

B.4.1 System Description

To demonstrate its validity, the basic method is applied to the robot shown in Figure B.15. One sensor could be used; however, two sensors are included here to provide sensor redundancy. With failure of one sensor, this system could still maintain precise control. While the above results are valid for 3D systems, for clarity, 2D cases of a satellite capture task are simulated. The system studied here in simulation is shown in Figure B.15, and is a space robot with two manipulators performing the pre-grasp portion of a satellite capture task [39]. The loss of attitude control has been lost on the satellite due to improper orbital insertion, failure of components, or lack of fuel is assumed. When the robot gets close enough to the satellite, the robot's manipulator tracks and reaches for a hardened grasping point on the satellite, such as the payload attachment ring. The objective of this part of the task is to track the grasp point (within a specified position and orientation error) on an uncontrolled spinning satellite long enough to allow a firm grasp to be made. The robot's end-point sensor is assumed to be able to measure the relative position and orientation of the grasp point. The inertial parameters of the robot are assumed to be well known, but the characteristics of the joint friction are assumed to be unknown except that the friction is Coulomb in nature with magnitudes approaching twenty to fifty percent of the maximum torque. These values are typical for space robotic systems [64]. The thruster sizes needed for the satellite capture task are substantial compared to those used for satellite attitude control. The characteristics of the thruster errors are assumed to be unknown.

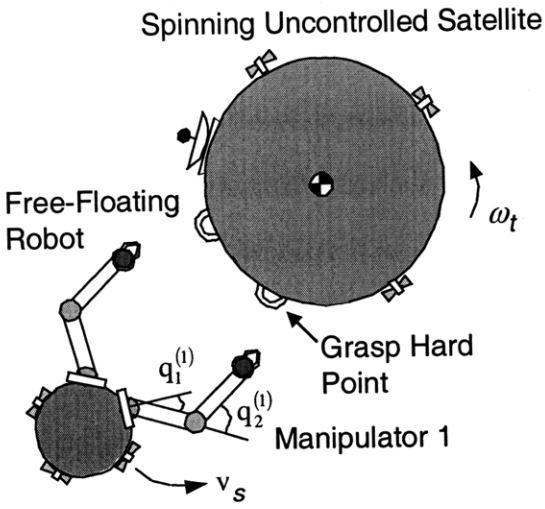

Figure B.15. Flat spin satellite capture example.

Table B.1 gives the parameters of the simulation. The manipulators are symmetric, separated by a 90 degree angle and each has two links. The target satellite has a radius of 3 meters and is assumed to be spinning with an angular velocity $\boldsymbol{\omega}_t$ of 3 revolutions per minute.

Table B.1. Space robot parameters.

	Length [m]	Mass [kg]	Inertia [kg m^2]
Spacecraft	4.2 (diameter)	2400	5808
Link 1	4	200	345
Link 2	3	100	106

B.4.2 Tracking Performance

The task is simulated in Matlab for a free-flying space robot, firing thrusters at the same time as the manipulator end-effectors are tracking the grasp points. The robot needs to avoid firing its thrusters in the direction of the satellite [53]. The position of the end-effectors is controlled by a Jacobian transpose controller. The forces and torques are estimated but the actuation compensation loop is not closed in the simulation runs in order to permit the identification of the torques to be seen. In use, this loop would be closed. Figure B.16 shows the desired spacecraft trajectory and the desired end-effector

trajectories for a representative case. Note that the two manipulator trajectories are different because they are reaching for different points on the rotating satellite. Figure B.17 and Figure B.18 show the end-effector position errors in the x and y directions for manipulators 1 and 2. The solid line shows the position error when there is no friction, and the dashed line shows the position error when there is Coulomb joint friction. Clearly, the error is larger is the presence of uncompensated joint friction.

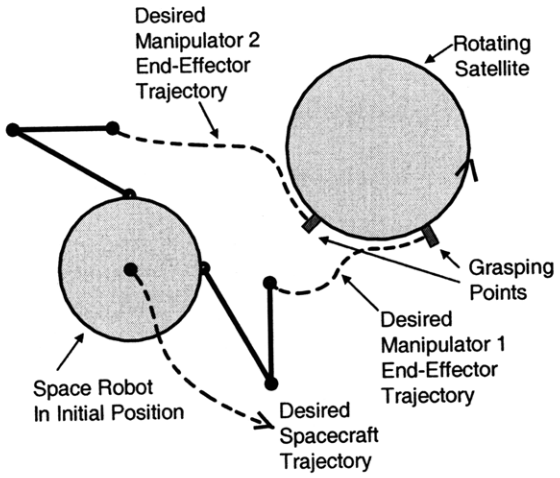

Figure B.16. Desired spacecraft and manipulator end-effector trajectories.

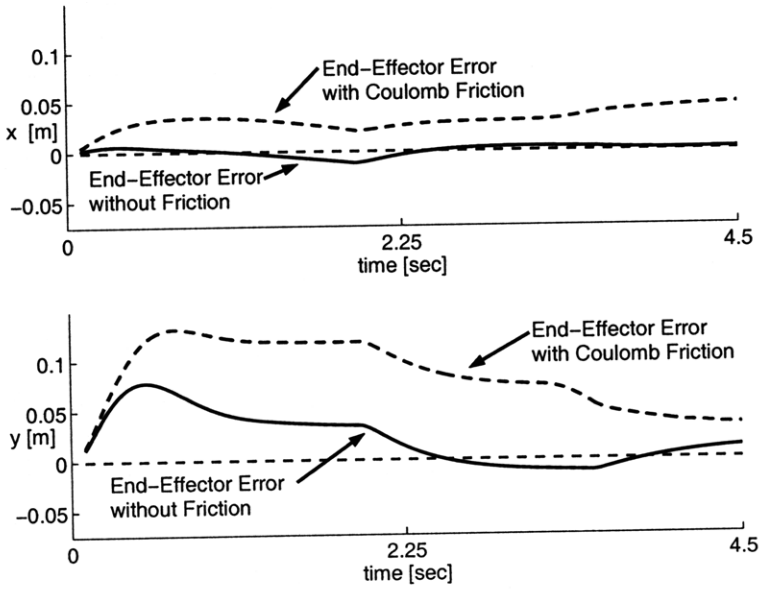

Figure B.17. Manipulator 1 end-effector position error.

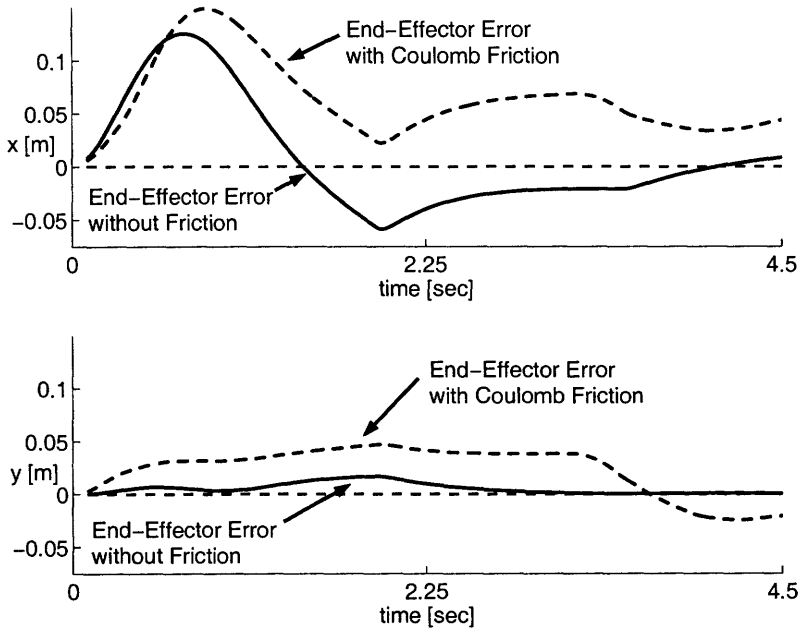

Figure B.18. Manipulator 2 end-effector position error.

The effects of joint friction can also be seen in Figure B.19 and Figure B.20, which show the torques in both joints for manipulators 1 and 2. The thin solid line is the commanded torque, the solid line is the actual torque, and the dashed line is the estimate of the torque. The commanded torque is generally larger than the actual torque due to the errors in the actuation. The method provides good agreement between the estimated value and the actual value especially for the first joint. Since the acceleration terms are neglected in the estimation algorithm for the results presented here, the method provides the best estimates for actuation closest to the sensor. In Figure B.20, the method works well for the first joint, but the torques for the second joint show a limitation of the method. Since the joint virtually remains stationary, the friction overwhelms the dynamic terms.

The spacecraft forces and moments are also estimated at the same time by the same sensor. Figure B.21 shows the spacecraft forces in the x and y direction. The thin line shows the commanded forces, the solid line shows the actual forces, and the dashed

line is the estimate value. The actual force values experienced by the spacecraft are substantially different than the commanded values. However, the method provides good agreement between the estimated actuation value and the actual value. The error between the estimate and the actual is less than five percent.

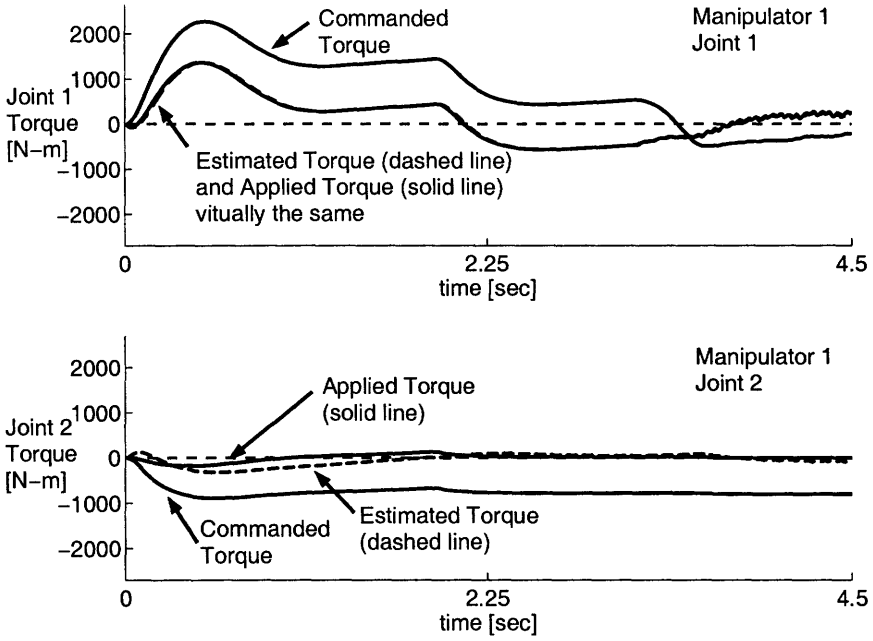

Figure B.19. Manipulator 1 torques for the large satellite capture task.

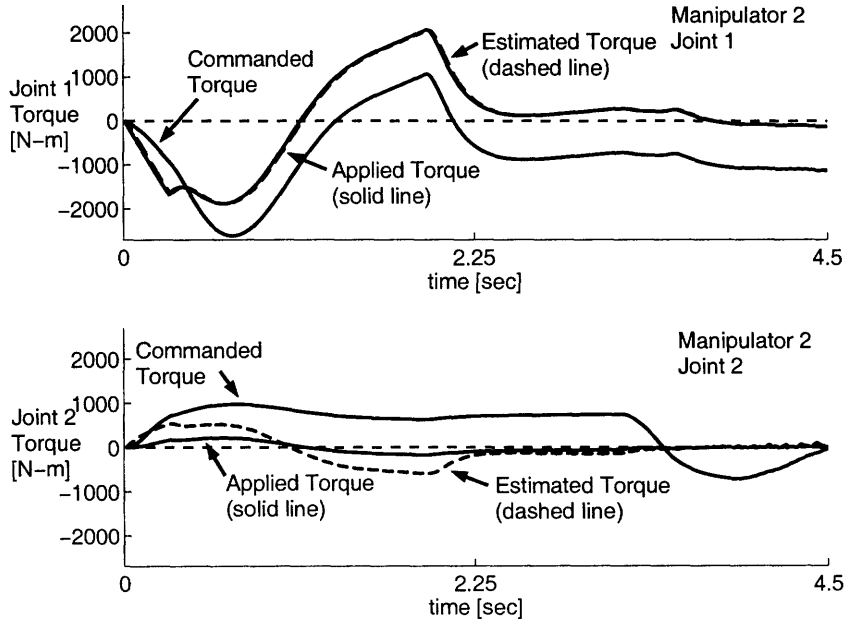

Figure B.20. Manipulator 2 torques for the large satellite capture task.

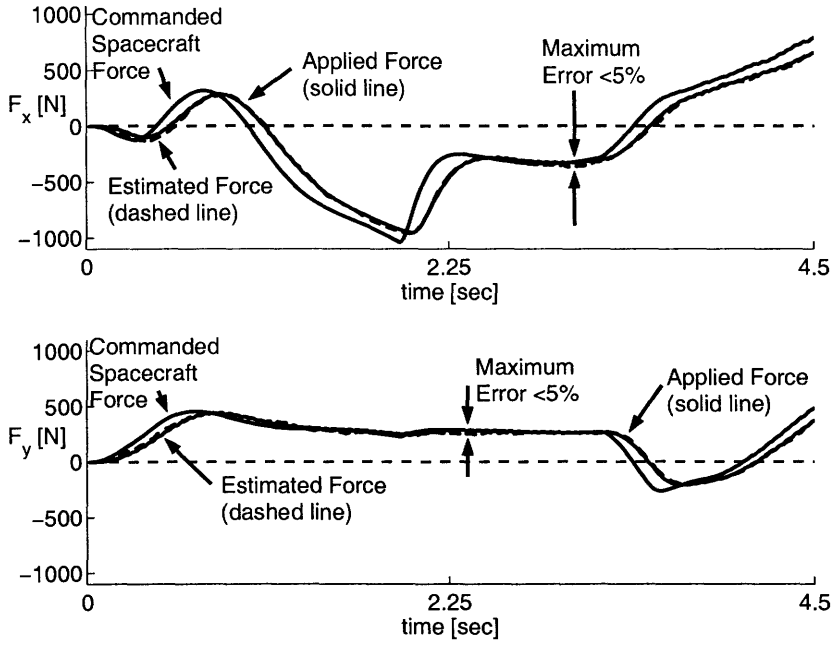

Figure B.21. Continuous x and y commanded net thruster forces for the large satellite capture task.

B.5 Summary

In space robots, actuator efforts can be degraded by such factors as friction, thermal, and other disturbances. Sensing is required for precise control. However, such sensing adds complexity, weight and cost. Hence, minimizing the number of sensors is important. Simulations demonstrate that dynamic models can be combined with limited sensing to identify actuation forces and torques in robotic manipulators, and minimum sensor configurations exist that are able to determine system actuation precisely. A base force torque sensor for each manipulator can provide an estimate for friction in the joints and applied reaction jets. These estimates can be used in an inner actuator control feedback loop. This controller can compensate for joint friction and spacecraft thruster inaccuracies and would take the form of a classical torque controller that requires individual joint torque sensors. A wrist force torque sensor for each manipulator can also be used to estimate joint friction and applied reaction jet forces. However, additional sensors are needed for cases when there are closed kinematic loop configurations.

The methods shown here can be applied to other situations such as unknown contact forces at the end-effector, unknown payload mass, or payload gripped with pin joints (rather than rigidly grasped). Systems with reaction wheels can be considered with this methodology. The approach is useful to study redundant sensor configurations and accommodate sensor failure.

APPENDIX

C

EXPERIMENTAL SYSTEM

This appendix provides details about the MIT Field and Space Robotics Laboratory (FSRL) Free-Flying Robotics Testbed (FFRT). The testbed is designed to enable the experimental verification of planning, sensing, and control algorithms for teams of space robots [3][4][7][68][69]. Section C.1 describes the experimental robots and associated hardware and sensors. Section C.2 describes the flexible structures. This appendix also includes suggestions for improvements based on lessons learned.

The Field and Space Robotics Laboratory is under the direction of Prof. Steven Dubowsky. Members of the FSRL who have participated in the design and construction of the testbed include Visiting Professor Yoji Kuroda, Dr. Matthew Lichter and Dr. Jamie Nichol, Visiting Engineers Yoshiyuki Ishijima and Tatsuro Nohara, graduate students Amy Bilton, Masahiro Ono, and Dimitrios Tzeranis, and undergraduates Patrick Barragán, Marcos Berrios, Andrew Harlan, Dan Lopuch, and Ta Kim from UCLA. Prof. Rich Wiesman consulted on the project. More recently graduate student Dan Kettler and visiting graduate student Chiara Toglia have run experiments using the testbed.

C.1 Experimental Robots

Chapter 5 presented the experimental space robots. This section describes additional details of the robots, including the mechanical systems, the coordinate systems, the gas systems, the electronics and software.

C.1.1 Mechanical Systems

This section describes the mechanical systems. The robot structures are made of a composite material, with a hexagonal base approximately 23 centimeters at its largest diagonal (see Figure 5.3 and Figure 5.4). The two manipulators each have a force/torque sensor at their base, a hexagonal structure supports the CO_2 gas tank, and the electronic boards are mounted vertically on one side. Four 7.2-V NiMH batteries sit in the middle and additional batteries can be attached. The gas system, including thrusters and air bearings, is mounted underneath, along with the position sensors (Logitech PS/2 Optical Mice [6][82]).

Figure C.1 shows the scale of the manipulators. The manipulator's motors and encoders are mounted inside of its structure. The manipulator's end-effectors are designed to be interchangeable depending on tests to be run. Figure C.2 shows an end-effector designed to carry a laser for trajectory following experiments. For the flexible module transportation and assembly experiments, a pin joint end-effector that transmits forces but not moments is used (see Figure 5.3) [34].

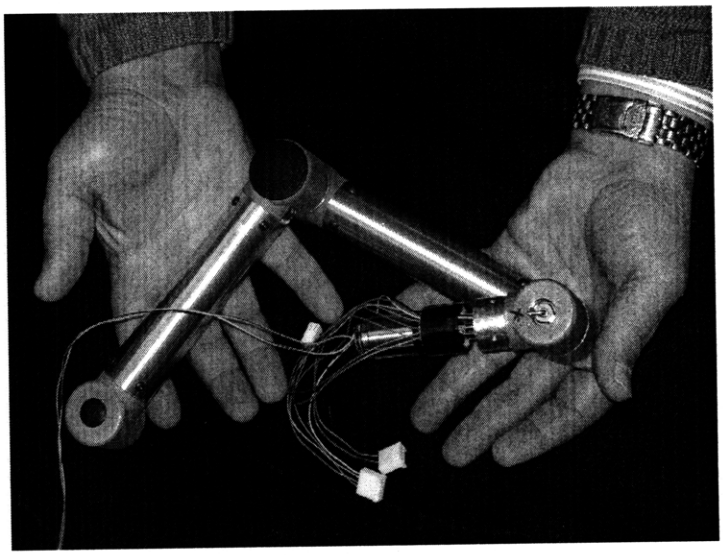

Figure C.1. Manipulator arm.

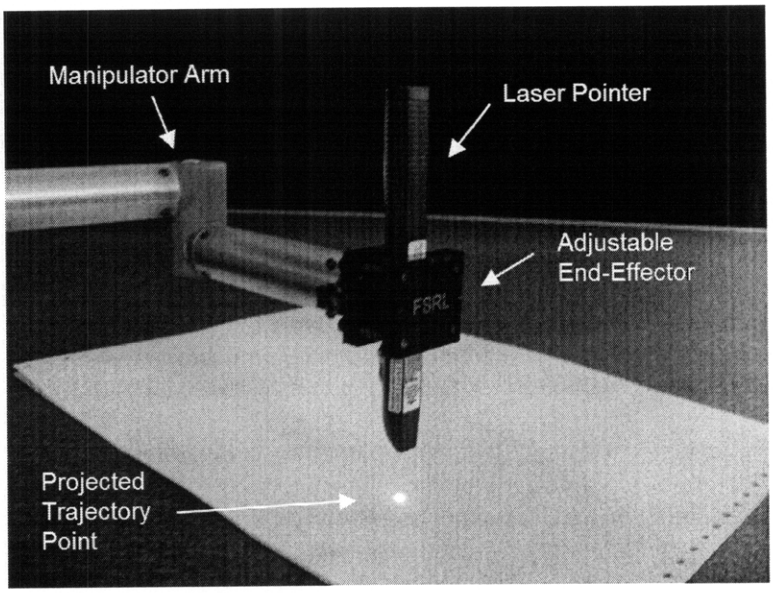

Figure C.2. End-effector holding laser pointer.

Custom force/torque sensors are placed at the base of each manipulator (see Figure C.3 and Figure C.4). They measure the two planar forces and one torque (F_x, F_y, and T_{xy}) by using four strain gauges. The sensors' four flexures are designed to deform linearly with the forces and torque. From their strains the forces and torque applied by the manipulator are estimated. The force/torque sensors are calibrated before use [68].

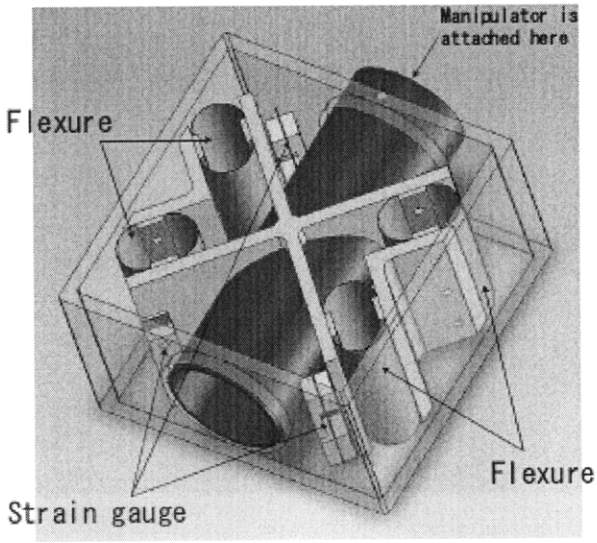

Figure C.3. Force/torque sensor design [Dr. Jamie Nichol].

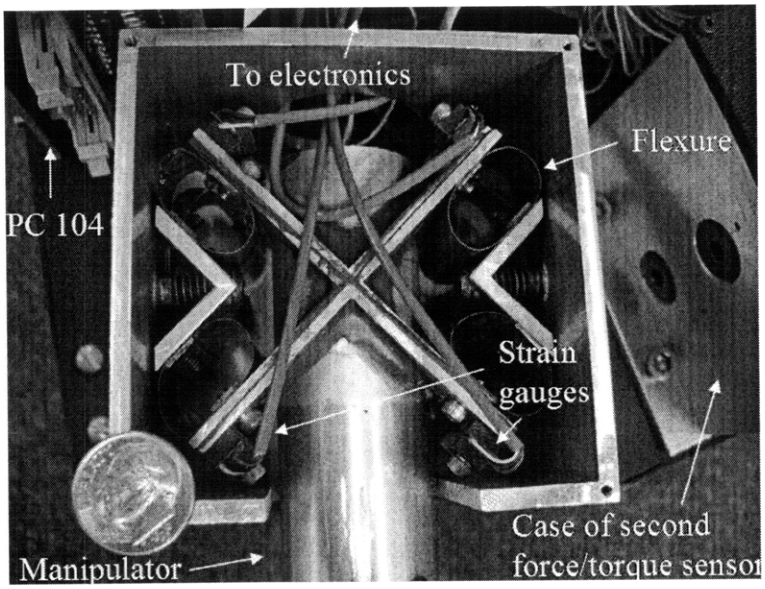

Figure C.4. Photograph of force/torque sensor.

C.1.2 Gas Systems

Figure C.5 shows a diagram of the gas system for the robot. The robots have a single tank of compressed CO_2 that is used for both levitation and driving the thrusters. The mass of the system changes slightly (approximately 220 grams) over the course of the experiments as the gas in the tank is used up, but this difference had negligible effects on the results. The robots are supported by three porous low-friction flat-floation bearings made by New Way Precision.

Each robot has eight reaction jet thrusters that drive the robot in the plane. Figure C.6 shows the locations and orientations of the thrusters on the robot. Each thruster can apply a force of approximately 0.1 Newton. The thrusters are driven by on-off solenoid valves, and are controlled with pulse width modulation (PWM).

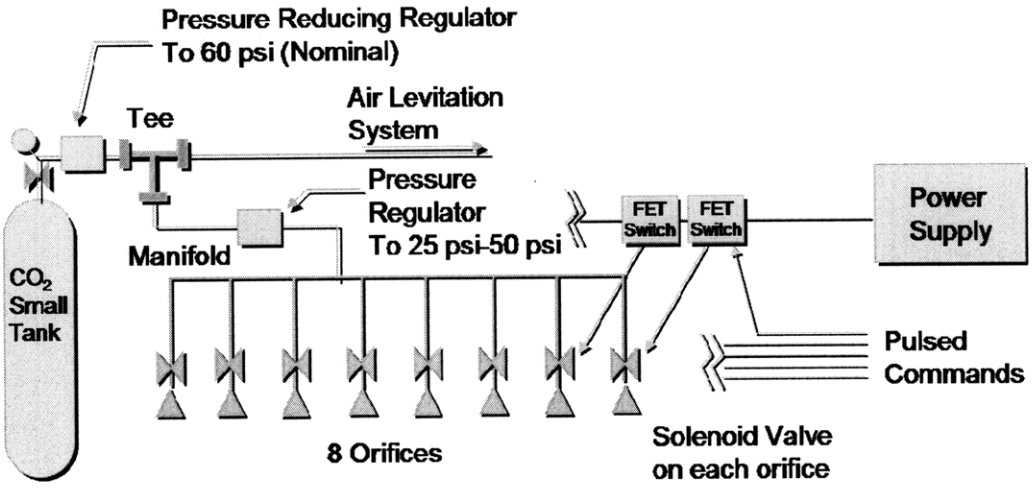

Figure C.5. Gas system [drawing by Prof. Yoji Kuroda].

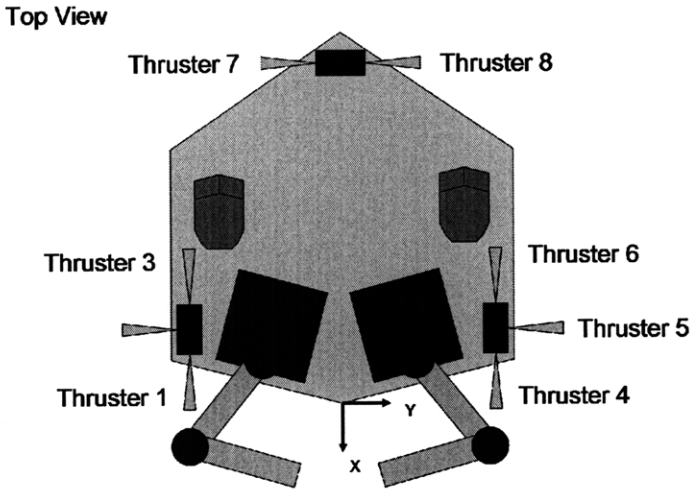

Figure C.6. Thruster locations [drawing by Dr. Matthew Lichter].

C.1.3 Electronics

The robotics electronics consist of an on-board PC104 computer with host CPU and motherboard, a custom power board, wireless LAN, a Softing CAN-AC2-104 peripheral board, the CANBus (twisted pair wires), and the interface electronic circuit boards with microcontroller firmware [47]. Figure C.7 shows a diagram of the electronics.

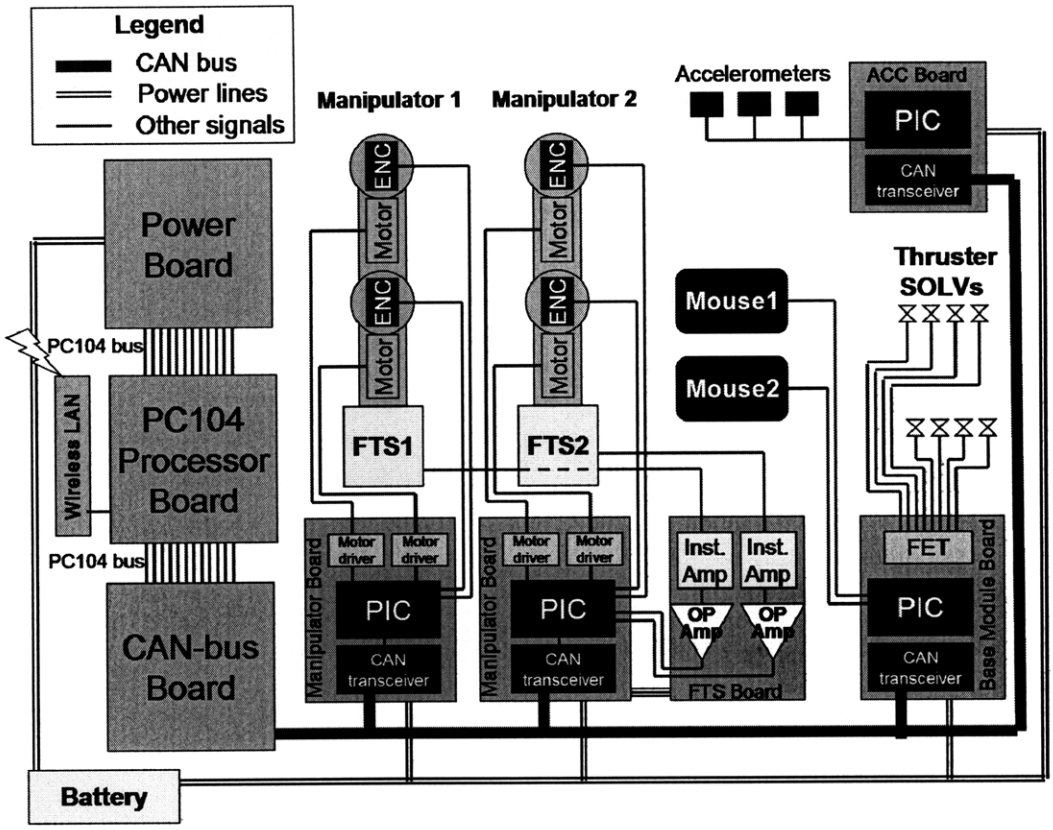

Figure C.7. Electronics diagram [Dr. Matthew Lichter and Masahiro Ono].

Communication between the PC104 and the actuators and sensors uses multiple layers of software, firmware, and hardware, as seen in Figure C.8. The top layer is the high-level robot controller software, written in Matlab and Simulink. This top layer is responsible for coordinating sensor and actuator activities, computing control laws, filtering and processing data, and managing the other aspects of an experiment. The robot's on-board computer is the Diamond Systems Morpheus PC/104 System. The robot is also equipped with a Belkin wireless router to allow wireless access between the on-board computers from the operator's control station.

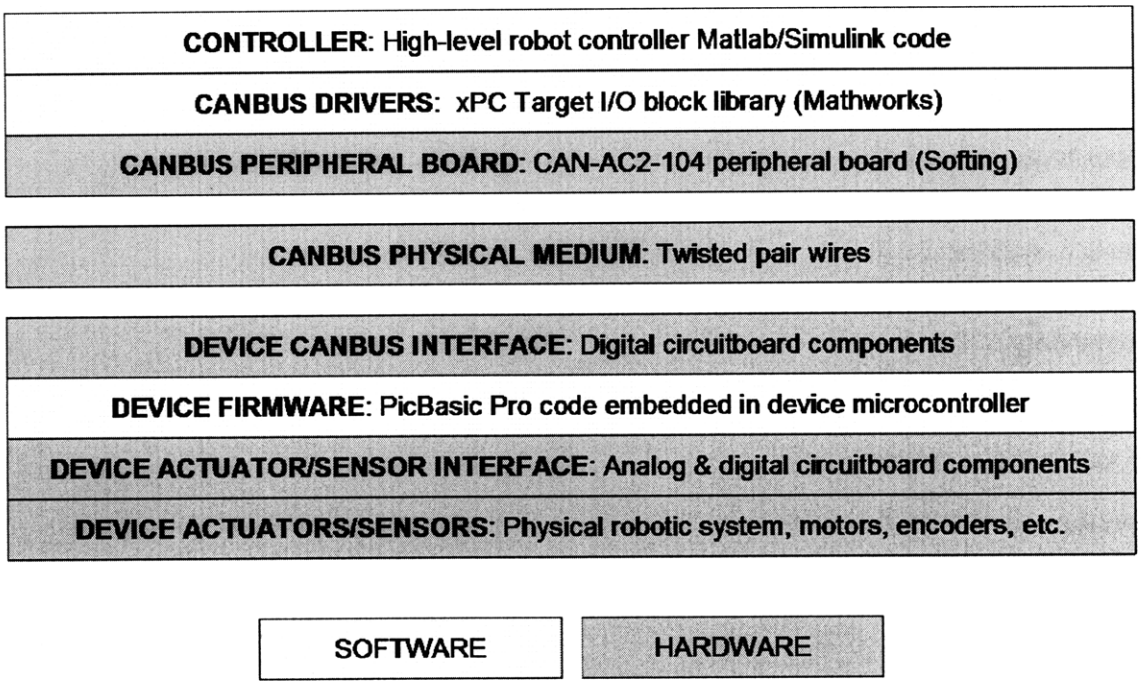

Figure C.8. Communication layers between PC104 and actuators and sensors [adapted from original by Dr. Matthew Lichter].

The controllers communicate with the CANbus peripheral board using an I/O block library provided by Mathworks that translates high-level commands and requests into small packets of data to be transmitted and received over the CANbus. The CANbus peripheral board is the hardware that physically puts data packets (CANbus *frames*) onto the CANbus physical medium [14]. Custom electronic boards are attached to the other end of the CANbus physical medium.

Four kinds of custom electronics boards are used to drive on-board sensors and actuators: manipulator boards, force/torque sensor boards, base module boards, and accelerometer boards (see Figure C.9). All boards except the force/torque sensor board have Microchip PICs for the operation of the sensors and actuators. The manipulator board controls DC motors and reads the digital angle encoders. Motor speed is controlled by PWM (pulse width modulation). The base module board controls thrusters and reads mice. The force/torque sensor board has instrument amps and operational amps to

amplify the signal of the force/torque sensors; these amplified signals are A/D converted on manipulator boards. The accelerometer board interprets the digital PWM signal from accelerometers on the flexible element.

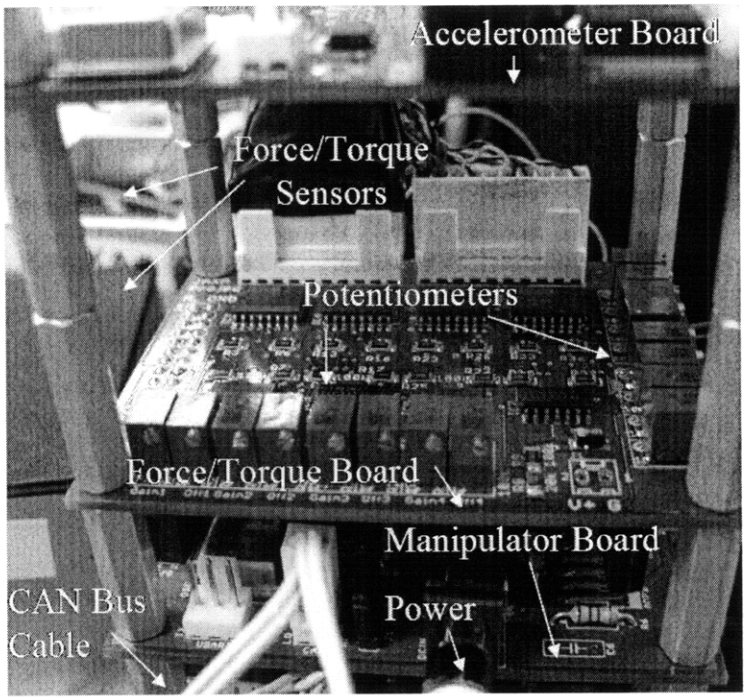

Figure C.9. Electronics stack.

C.1.4 Software and Controllers

The software for the simulations and the experimental system is written with Matlab and Simulink. The real-time software is implemented with the Matlab xPC Target. The code is written in Matlab .m files and C/C++ code accessed from Simulink through S-Functions. The controllers are implemented in Simulink and simulations are written using SimMechanics plants. When the simulations are debugged and working, the SimMechanics plant blocks are removed from the Simulink model and replaced with xPC plant blocks that communicate directly with the experimental hardware via a layer of CAN software provided by Matlab. The real-time software is compiled on a laptop,

downloaded onto the PC104 computers on the robots, and triggered via wireless link. During the experiments, the controllers execute on the target without communicating with outside systems. After completion of an experiment the PC104 transfers data back to the host laptop. Running simulations and hardware verification in parallel allowed for rapid prototyping and easy comparison of controller methods.

C.1.5 Robot Coordinate Systems

This section describes the coordinate systems (or frames) used for the experiments. The global inertial reference system is fixed in the experimental platform, either the granite table or the epoxy floor. The location of the origin and the orientation of the reference inertial system are set independently for each experimental case. Each robot has two coordinate systems: a local coordinate system attached to the robot that moves with the robot, and a global inertial coordinate system fixed in the experimental platform (see Figure C.10). The robot's local coordinate system has its origin at the front corner of the hexagonal base and its x axis is aligned with the robot's axis of symmetry. The y axis is orthogonal to the x axis and the z axis is out of the plane. The robot's global coordinate system is typically chosen so that it aligns with the local coordinate system at the initial time. The inertial coordinate systems for the robot and reference are always fixed relative to one another and are related by a translation and a rotation.

The inertial position of the center of mass of the robot system is denoted by the vector $\mathbf{R}_{CM}$. The center of mass of the base section alone (without the manipulators) is denoted by the vector $\mathbf{R}_{CS}$. The local origin for the robot is specified in inertial space by the vector $\mathbf{R}_0$.

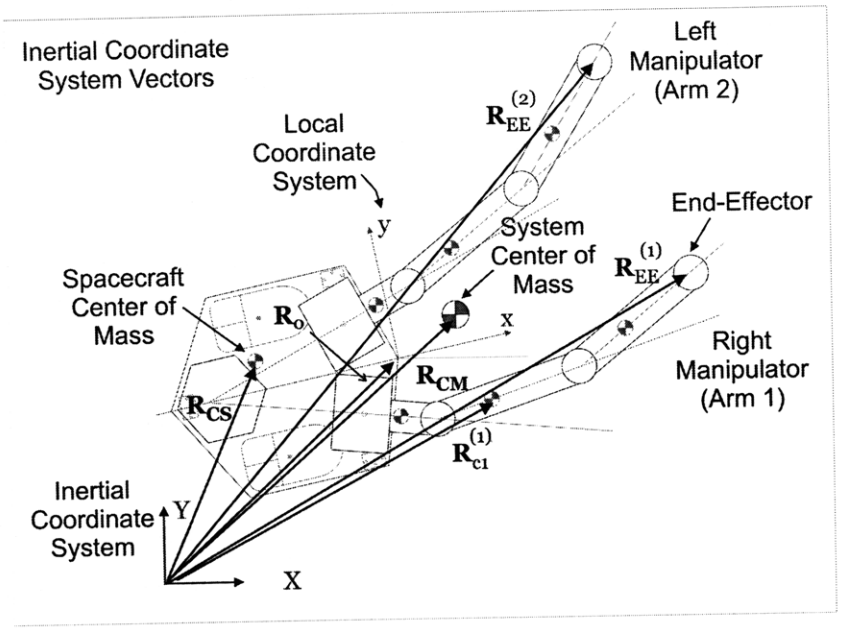

Figure C.10. Experimental robot coordinate frames and inertial vectors.

C.1.6 Robot Sensor Performance and Bandwidth

With any systems as complex as these seven DOF robots, lessons are learned in the design and implementation process. The most challenging areas are the sensors and the communications system. The force/torque sensors are the most problematic, and the issues with communication system delays lead to restrictions on the controller bandwidth. This section discusses the robots' limitations and makes suggestions for improvement.

The force/torque sensors were custom built because of cost and the limited availability of sensors capable of measuring the small forces with adequate resolution. The force/torque sensors proved to be sensitive to out of plane forces and consequently joint position. The force/torque sensor calibration is able to compensate for some of this sensitivity [68]. The force/torque sensors are also sensitive to room disturbances, such as air conditioning and the fans on nearby desktop computers. Figure C.11 shows the x and y components of the force/torque measurements on the right manipulator of robot 1 when the system is at rest, and Figure C.12 shows the same measurements when the room air conditioner is on. Redesigning the supporting structure of the force/torque sensor (see

Figure C.4) could make the design stiffer and less sensitive. Furthermore, signal processing for the force/torque sensors could be improved by additional shielding on the load cell wiring, by physically moving the electronics closer to the load cells to reduce noise and interference, and by revising the custom electronic board design to eliminate coupling between the gain and offset potentiometers.

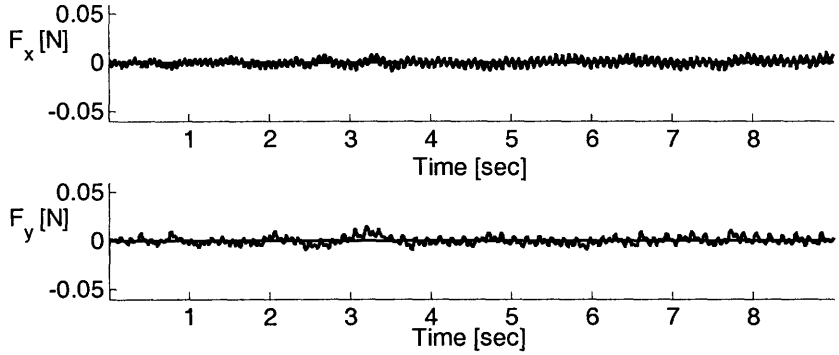

Figure C.11. Force/torque sensor measurement for right manipulator of robot 1, at rest with gas system off (not floating).

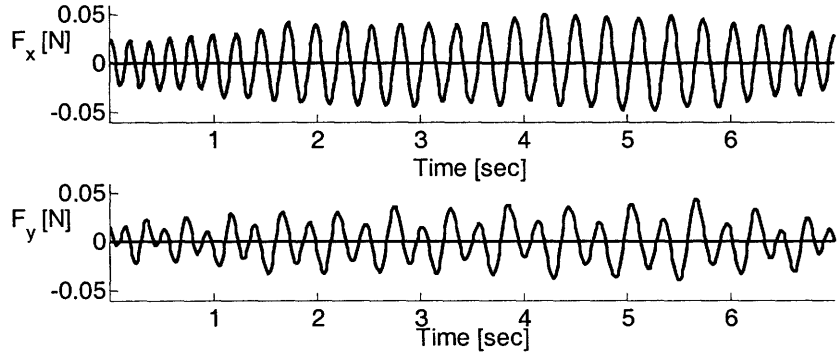

Figure C.12. Force/torque sensor measurement for right manipulator of robot 1, at rest with gas system off, room air conditioner on.

The other manipulator sensors, the joint encoders, performed well. Once calibrated, the mice also performed well. For this application, the nonlinearities and on-off nature of the thrusters dominated the control loop containing the mice. However, replacing the simple desktop mice with faster ones designed for computer games could improve performance.

Limitations in the communications systems impose unexpected and undesirable restrictions on the robot's controller bandwidth. As the system is currently constructed, there is a propagation delay between the time the high level controller requests a read or a write function until the time the custom electronic boards perform the operation. Although the bit stream is transmitted over the CANbus at approximately 1 Mbit per second, the effective rate of the larger system is much slower. The time delay is highly variable and is in the range of tens of microseconds to tens of milliseconds (depending on the sensor). A buffer somewhere in the CANbus or communications software or on the hardware boards is believed to act as a delay between when the functions are called and when the bits are placed on the CANbus. Partially to address this problem, the original Linux operating system was replaced by Matlab xPC, but the change did not improve the time delays substantially. Although CANbus systems operate at high speeds elsewhere, the CANbus implementation is problematic here [14]. Future users of the testbed should consider replacing the CANbus system with more commonly used I/O boards, although this is not a simple change due to the number of actuators and sensors involved. Additionally, the current configuration allows a single PC104 to control both robots, simplifying issues of robot to robot communication.

The bandwidth and control of the experimental robots is limited by these time delays. For example, Figure C.13 and Figure C.14 show representative Bode plots for Joint 1 (closest to the base) and Joint 2 for the right manipulator arm on the second robot. The gas system was disabled so the robot is effectively a fixed-base manipulator. The manipulator joints were driven at varying frequencies and the output frequencies recorded. The sampling time for these cases is 0.01 seconds. The figures show that the manipulators do not track the inputs well at frequencies above $2-2.5\pi$ radians per second (1-1.25 Hertz).

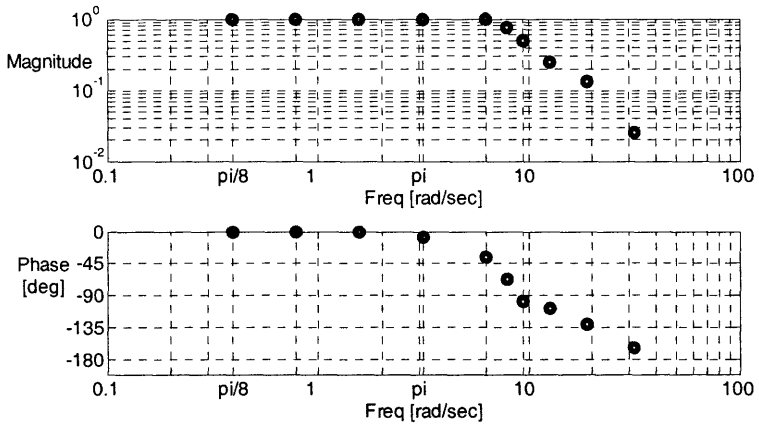

Figure C.13. Bode plot of Joint 1 on the right manipulator for robot 2 (fixed-base). Sampling time is 0.01 seconds.

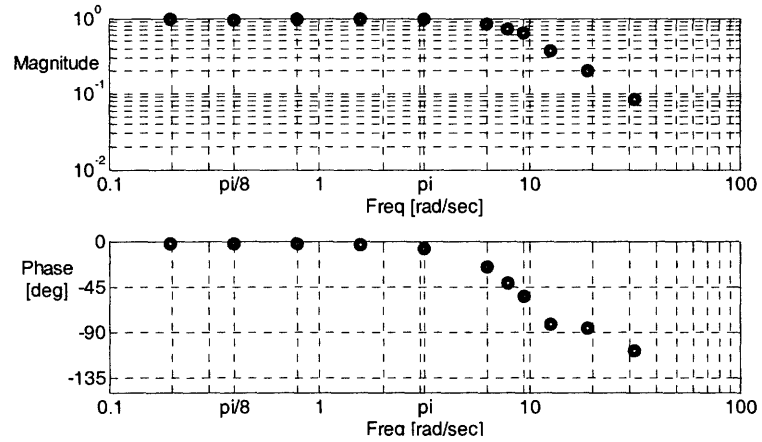

Figure C.14. Bode plot of Joint 2 on the right manipulator for robot 2 (fixed-base). Sample time is 0.01 seconds.

C.2 Experimental Flexible Elements

This section discusses the design of the experimental flexible modules [34][68]. The purpose of these flexible elements is to emulate the behavior of representative flexible modules that would be found on orbit during the construction of large space telescopes or large space solar power stations. The ideal experimental structure has a low damping ratio (under one percent), and is extremely flexible in the transverse direction with dominant frequencies at least twenty times smaller than the bandwidth of the robot controller. The experimental structure must be lightweight since the force/torque sensors support the load. If the experimental structure has transverse deflections on the order of five to ten percent it is easy to make visual comparisons of various controllers.

However, constructing an experimental structure that meets these criteria is challenging. Even if an experimental facility large enough to manipulate the proposed 200 meter space structure could be found, the structure would not support its own weight on earth. Scaled to the testbed robot dimensions, the structure would be more than 6 meters long. The largest beam that fits on the granite table is 1.5 meters. The size of an experimental structure is also limited by the amount of weight that the robot force/torque structures can support. No simple beams of metal or composite material with length near to the testbed size were found to meet the design requirements.

Other designs for the flexible structures were considered. Large masses were added to the structure to lower frequencies, but made the structure too heavy for the force/torque sensors. The height of the structure was reduced to limit weight. From Euler beam theory, the height of the beam does not contribute to the frequency [55]. However, the shorter prototypes (approximately 3 centimeters) plastically deformed. Other experimental prototype designs sagged under their own weight, twisted out of the plane, and did not meet the frequency and damping requirements.

Alternative designs for the flexible element such as a zig-zag beam (see Figure C.15) or a lumped-mass beam built with metal shims and rigid composite elements (see Figure C.16 and Figure C.17) were also considered. (These alternative beams were designed after conversations with Prof. David Miller. The beams were built by Patrick Barragan.) The zig-zag design allows substantial axial as well as transverse vibrations, complicating the control of the structure. The zig-zag beam has large amplitude of vibrations and a low damping ratio, but suffered from significantly sag under its own weight. The lumped-mass structure consists of lumped masses (polymer tubes) separated by springs (thin metal shims). The natural frequencies of this beam could be tuned by varying the lumped masses and the lengths of exposed shim, although this beam is more complicated to fabricate.

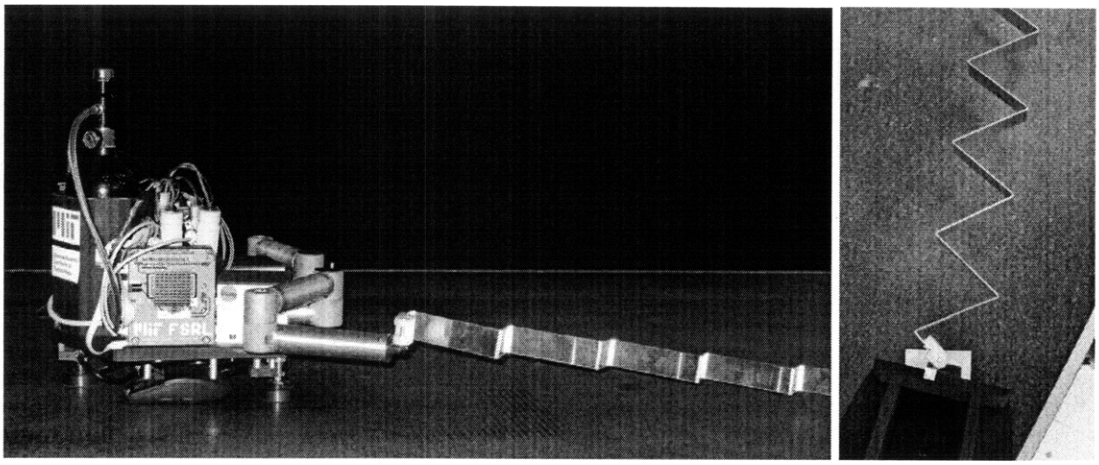

(a) Side view *(b) Top view*

Figure C.15. Zig-zag beam prototype.

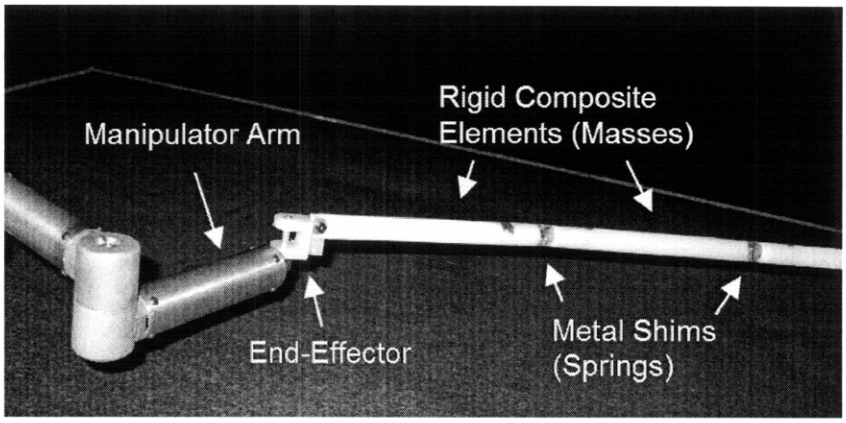

Figure C.16. Lumped mass beam prototype.

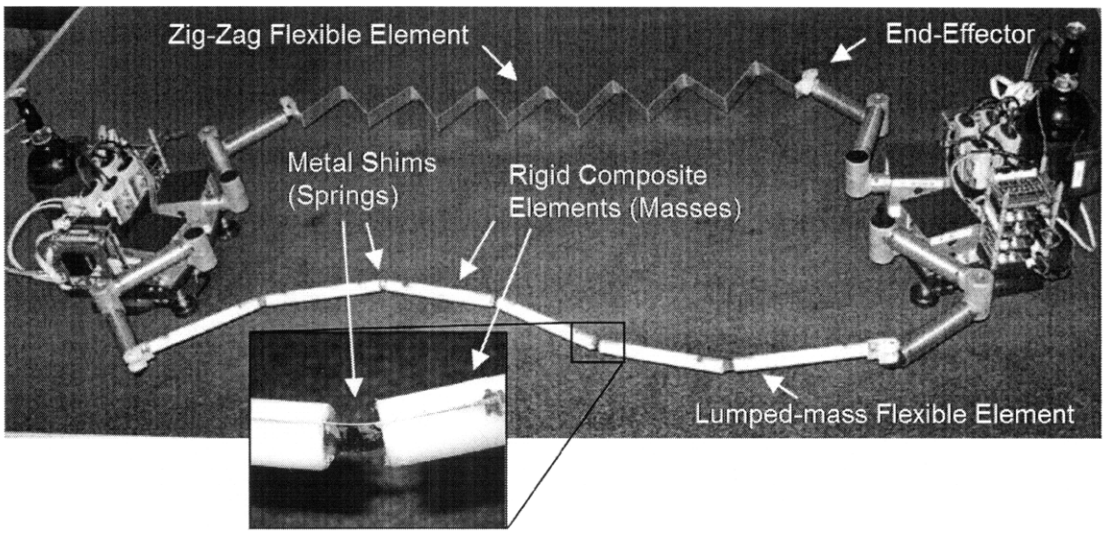

Figure C.17. Overhead view of two robots manipulating lumped-mass and zig-zag beams.

For the experiments presented in this thesis, the flexible element chosen is a simple aluminum beam supported by the robot end-effectors, as seen in Figure 5.1. The beam is 1.22 meters long, 0.80 mm thick, and 12.8 centimeters tall. The beam's lowest natural frequency is 2.8 Hertz and it has a damping ratio of 15 percent. Figure C.18 shows an alternative configuration for the experimental system. In this figure, the flexible element is a flat piece of aluminum supported by two passive floating modules.

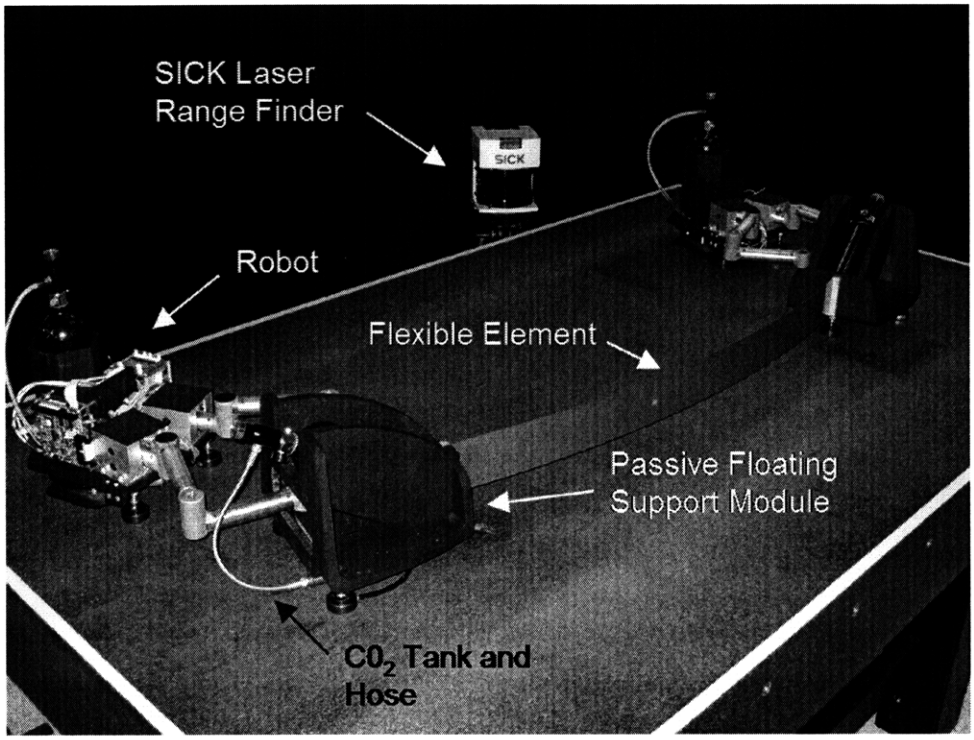

Figure C.18. Alternative configuration for experiments with flexible elements supported by passive floating modules [with Amy Bilton].

The flexible elements would have their vibrations excited by thrusters in an on-orbit system. It is difficult to have the low amplitude forces of the CO_2 thrusters excite large amplitude easily visible vibrations. However, the motions of the manipulators are able to produce easily visible amplitudes.

Distributed accelerometers manufactured by Analog Devices measure the motions of the flexible elements (see Figure 5.1 and Figure C.19). These accelerometers have a

measurement range of +/- 1.2g and a measurement variance (σ_a^2) of 0.013g^2. Although not used for the experiments in this thesis, additional testbed sensors include a laser range finder and overhead cameras. The SICK LMS 291 laser scanner provides vision deflection measurements of the flexible structure (see Figure C.18) [79]. The measurement variance in the range direction (σ_v^2) for this system is calculated to be 1.7 mm^2 [3]. Overhead cameras made by Videre Design are available to provide additional position measurements. The overhead camera collects images at a rate of 15 Hertz and the camera measurements have a resolution of 6 mm.

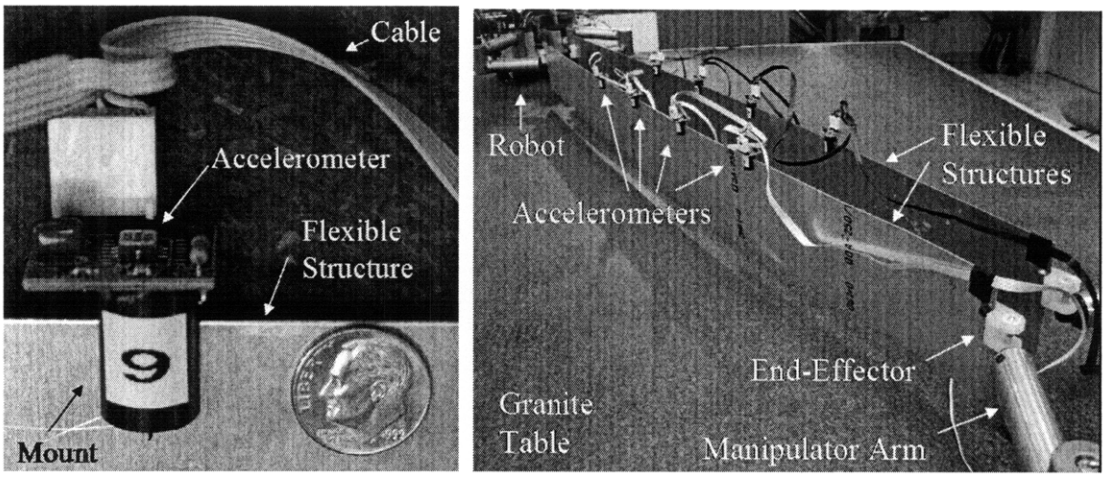

Figure C.19. Accelerometers.